Deformation and Shape Transition Studies of Single Mammalian Red Blood Cells in View of the Effects of Diseases or Chemical Modifications by Means of Microfluidic Devices

Dissertation im Fach Physik
vorgelegt der
Mathematisch-Naturwissenschaftlichen Fakultät
der Universität Augsburg

Juni 2014

angefertigt am
Lehrstuhl für Experimentalphysik I
- Softmatter and Biophysical Physics -
Institut für Physik der Universität Augsburg
bei Prof. Dr. Thomas Franke
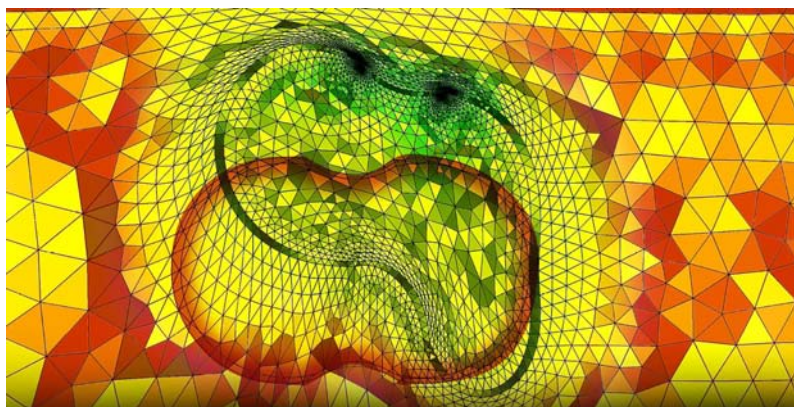
von
Benjamin Eggart M.Sc.

Nanosystems Initiative Munich Calendar 2013 - August
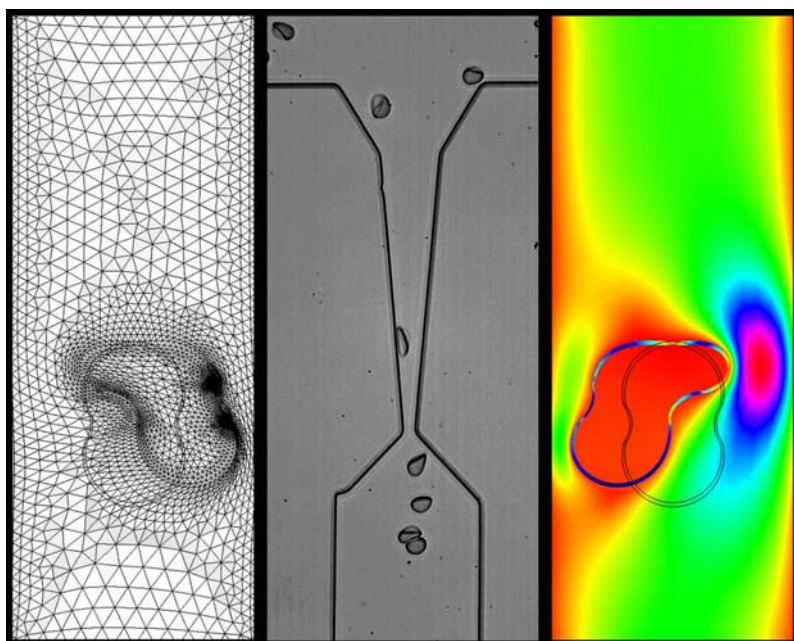
Center for NanoScience Calendar 2014 - September

Abstract

The main focus of the thesis was to study and understand why human RBC change their shape upon increasing shear stress in the microvasuclatur. Therefore, human RBCs were observed while flowing in PDMS micro-channels of different structures (even structure, corner structure, spiral structure and zig-zag structure) and tapered glass capillaries. This allowed for the study of RBC morphology upon various levels of flow conditions or shear stress, respectively.

Besides the study of the flow behaviour under various flow conditions various types of RBCs were investigated. The following mammalian red blood cells (RBCs) were investigated: healthy human RBCs, chemically modified RBCs as a model system for blood diseases, RBCs suffering from β-Thalassemia and Spherocytosis as well as RBCs from Alpaca (vicugna pacos). The chemical modification was performed by incubating healthy RBCs in suspensions of phosphate buffered saline (PBS) with a small concentration of either formaline, diamide or cholesterol. The chemicals formaline and diamide hardened the cell membrane and cholesterol changed the strain inside the RBC membrane. To characterize the RBC mechanics quantitatively the following physical parameters were used: bending modulus, shearing modulus, area expansion modulus and the transition velocity.

First, cell morphology in flow was investigated regarding length and curvature measurements of the two-dimensional cell projection (for example length to width ratio or front and rear curvature). For each cell type the discocyte, slipper and parachute shape was measured regarding width to length ratios and protuberances-length ratios as well as front and rear curvatures. A detailed study of the healthy, chemically modified and diseased shape morphology showed that chemically modified and diseased cells had a different shape and size compared to healthy RBCs. The variations of the measured two-dimensional projection ratios and curvatures showed a correlation to alterations in the cell membrane.

Second, in flow systems the mechanical properties were investigated dynamically. While the cells were exposed to a constant hydrodynamic flow field their deformation was measured. The Taylor deformation parameter varied proportionally to changes in mechanical properties of the RBCs. Chemically modified

RBCs showed a smoother increase of the Taylor deformation with increasing cell velocity and saturated at lower Taylor deformation levels. Modifications of the RBCs with diamide and formaline incubations decreased the Taylor deformation parameter for the measured flow regimes dramatically. This supported the results from the static measurements. However, the Taylor deformation parameter did not indicate shape changes of RBCs (such as discocyte to slipper or parachute) which were observed upon increasing shear stress.

Third, using PDMS micro channels the shape transition from the discocytic rest shape to a slipper or parachute shape of RBCs was characterized further. In a 10 x 10 µm (width and height) channel the transition velocities v_c of hundreds of RBCs for different volume flows were measured. It was found that the transition velocity solely depends on mechanical properties of the RBC membrane. Formaline and diamide modifications increased the transition velocity by a factor of about two to three. Low cholesterol content in the membrane as well as high tonicity of the suspension medium increased the transition velocity weakly. In contrast, high cholesterol content and low medium tonicity decreased the transition velocity. Cells from donors with the blood disease β-Thalassemia showed an increase of the transition velocity of around 25 %. In the case of Spherocytosis disease a dramatic increase of around 470 % was observed.

Fourth, using tapered glass capillaries, the shape transition was further investigated to see the effect of different channel heights as well. In contrast to PDMS microchannels glass capillaries had different round shaped cross-sections if they were fabricated with a small taper angle. This experiment enabled for each RBC alteration the drawing of a phase diagram showing the shape morphology in dependency of the cell velocity and squared capillary radius. Alterations in the membrane by chemical modification or blood diseases were visible by different phase boundaries. As a proof of principle transition velocities of the 10 x 10 µm PDMS channel experiments were validated for the same flow environments. In addition, phases with very high slipper probabilities were identified at small capillary radii. This was mainly due to the wall interactions of the cells for small capillary radii.

The fifth research focus investigated the transition into a slipper and parachute shape in more detail. Therefore, the slipper was observed in a weakly tapered

glass capillary and a slip velocity was introduced. The slip velocity is the difference of the experimentally measured cell velocity and the theoretical extrapolated velocity in undisturbed flow at the corresponding capillary radius. In the experiments, the slip velocity increased during the shape transition. As a conclusion the main effect of the shape transition was to lower the flow resistance.

These experiments brought new insight to the shape change of human RBCs. However, RBC from alpaca showed a different shape behaviour. In both microfluidic flow systems (glass capillary and PDMS microchannel), the flow motion of Alpaca RBC was investigated as well. At rest these cells were characterized by an elliptical extended shape. Exposed to shear stress, these cells behaved differently from discocytic mammalian RBCs because they deformed much less. However, as a new characteristic, they showed a combination of flow motions of healthy human RBCs: tumbling and swinging. The tumbling motion of RBCs was characterized by an incidental inclination angle with respect to the flow direction whereas the swinging motion showed a periodical change of the inclination angle with respect to the flow direction. Furthermore, the relaxation time after an induced bending of Alpaca RBC was measured by squeezing them through extremely narrow capillaries ($2R_{cap} < 2\,\mu m$). This enabled the determination of a bending modulus ($\kappa = 62.1 \cdot 10^{-19}\,\mathrm{J}$).

Zig-zag structured channels allowed the deformation of single RBCs periodically. With increasing deformation amplitude, the cells changed their deformation response times. At a certain deformation amplitude their deformation time at the entrance of the period was longer than their relaxation time at the wide part of the period. This is due to the viscoelasticity of the cells.

With the micropipette aspiration (MPA) technique, the shear modulus μ and a parameter B, which was correlated to the area expansion modulus, have been measured. Furthermore, indentation type atomic force microscopy (IT-AFM) [140] was performed to measure the bending modulus κ of the RBCs. These static measurements showed that formaline and diamide modified RBCs were accompanied by an increase in bending and shearing moduli compared to healthy RBCs. Diamide modification disabled the shearing and bending ability in a much stronger way than formaline treatment. In contrast, the diseased RBCs showed only a weak increase in the bending modulus and area

expansion modulus.

The viscoelastic behavior was also investigated by coupling surface acoustic waves (SAW) into PDMS microchannels. It connected rheology and microfluidics. Frequency sweep measurements allowed the investigation of the viscoelastic response by different deformation frequencies. In the measurement, healthy RBCs deformed until deformation frequencies of f=50 Hz to f=150 Hz. The diamide and formaline modified RBCs showed a deformation response even for high frequencies (up to $f \approx$ 1 MHz). This means another strong evidence for increased mechanical properties.

Red Blood Cell, Single Cell Analysis, Microfluidics, Anemia, Spherocytosis, β-thalassemia, Chemical Modification, Alpaca (vicugna pacos), Indentation Type Atomic Force Microscopy, Micro Pipette Aspiration, PDMS Microchannels, Glass Capillaries, Structured Microchannels, Surface Acoustic Wave Microfluidic, Environmental Scanning Electron Microscopy

Contents

Abbreviations

AFM Atomic Force Microscopy

ESEM Environmental Scanning Electron Microscope

FEM Finite Element Method

IDT Interdigital Transducer

IT-AFM Indentation Type Atomic Force Microscopy

MPA Micropipette Aspiration

PDMS Polydimethylsiloxane

RBC Red Blood Cell

SAW Surface Accoustic Wave

Chapter 1

Introduction

The first description of human RBCs and their particular shape changes upon shear stress was published in the Philosophical Transactions of the Royal Society by the Dutch microscope manufacturer Antonie van Leeuwenhoek in 1675. He observed human erythrocytes under his self-made light microscope and reported that these cells have a soft and flexible character capable of passing through the microvasculature in the human body. While flowing in small capillaries they deformed into ovals (two-dimensional projection), whereas in larger capillaries they adopted their rest shape reversibly [157].

The non-nucleated erythrocyte of mammals is unique among vertebrates. The main component which determines the mechanical properties is the membrane of the cell. Additionally, the membrane dictates the shape of the cell. RBCs of mammals, except Camelidae, show a typical biconcave discoid shape. The cells can undergo high degrees of passive deformation during constantly changing shear stress in capillaries having cross-sections one-third of their own diameter. This is mainly possible because of the specific mechanical parameters of the membrane which allow the cell to change its shape. At rest the membrane designates the typical discocytic shape. Subjected to extreme shear stresses in the circulatory system, a discoid red cell shows two changes in shape: an asymmetric slipper shape and an axisymmetric parachute shape. This change of shape is supposed to be correlated with the lowering of flow resistance and may play an important role in tempering hemoglobin [146]. In contrast, the RBCs of the camel family shows different unique physiology in the class of mammals. Exposed to chronic hypoxia or dehydration (high altitudes or deserts), Camelidae need less cardiorespiratory adjustments compared

to any other mammal [132, 169, 93]. To summarize, they have a very high resistivity against dehydration [13, 169, 93], low oxygen levels [119, 170, 111] or a high resistance to osmotic lysis [91]. These adaptations are supposed to be related to the mechanical properties of the camel RBC because their cells store water by binding amino acids and have a higher hemoglobin content [170, 111]. Regarding the cell shape there is another uniqueness in the class of mammals. Unlike most mammals, which have biconcave discoid shaped erythrocytes at rest, those of camel, such as alpacas, camels, guanacos and vicunas have a flattened ellipsoid [87, 92, 108]. This typical shape is also supposed to be correlated with the mentioned physiologically important features [170].

Measuring and investigating the physiological flow behavior of mammalian RBCs will improve the understanding of blood flow, the characterization of blood diseases and will provide further insight relevant to the design of medical therapeutics. Moreover, the identification of RBC deformability is indispensable for medical diagnostics as well as for understanding physico-chemical relation on the cellular and molecular levels [101, 75, 50].

As mentioned, the macroscopic cell deformation is strongly correlated with RBC architecture at the molecular level. The membrane of a RBC has a composite architecture made up of a lipid-protein bilayer and an underlying cytoskeleton anchored to the lipid membrane [101]. In contrast to a regular cell structure the cytoskeleton is not cross-linked through the cytosol but is a second layer. The interplay between lipid membrane and the underneath cytoskeleton layer provides the viscoelastic properties of the cell envelope and ensures a reversible response to external stress. The resistance to shear deformation is mainly given by the cytoskeleton because of the fluid character of the lipid membrane. In contrast, the lipid membrane dictates bending response [122].

Modifying human RBCs with chemicals which are known to alter the mechanical properties of the membrane, the interplay of the molecular level of the membrane and the macroscopic cell deformation can be investigated. For example, chemicals like diamide and formaline are known to increase the number of cross-links inside the cytoskeleton. Changing the cholesterol content of the suspension allows the variation of the lipid bilayer area that alters the initial tension of the cytoskeleton. Exposing the cells to solutions of varied tonicity the cytosol pressure can be controlled [96]. The chemical modification thus enables the alteration of the cell elasticity or the three main mechanical

parameters (shear modulus, bending modulus and area expansion modulus). Additionally, chemically modified RBCs can be a model system for blood diseases which induce an altered cell deformability as well.

Mechanical characterization has become possible mainly by two techniques that are now widely used. In the 1970s, Evans [39], Chien [25] and Hochmuth [59] developed a method to investigate mechanical cell properties by Micropipette Aspiration (MPA). The technique has been successfully used to measure the shear elasticity μ and area expansion modulus K_A of RBCs [99, 22, 154, 60]. A single cell is aspirated into a glass capillary and the position of the membrane tongue in the pipette is observed. The dependency of aspiration pressure and aspiration length yields a stress-strain relation. However, available literature values of the moduli for healthy RBCs scatter significantly in the range of $\mu = 1\,\mu\mathrm{N/m}$ to $13\,\mu\mathrm{N/m}$ [39, 135, 43, 58, 82, 85], whereas very precise measurements of tip radii, using secondary electron microscopy, leads values between $6\,\mu\mathrm{N/m}$ to $9\,\mu\mathrm{N/m}$ [61, 44]. The main reason for higher degree of divergence between different authors are different cell preparations and different blood donors. The same situation is true for Indentation Type Atomic Force Microscopy (IT-AFM) [140]. The measured bending stiffness varied between $\kappa=0.13\cdot10^{-19}\,\mathrm{J}$ to $3\cdot10^{-19}\,\mathrm{J}$ [40, 68, 124, 173, 65, 141, 159, 175, 110, 54]. IT-AFM technique uses a nanometer-sized tip to scan the surface of a cell and measures the mechanical properties by measuring the indentation force of the AFM-tip into the cell.

In the last two decades, microfluidic has become a multi-disciplinary research field because it combines physics, biology, chemistry or medicine. The so-called "lab-on-a-chip" devices provide possibilities similar to those of large-scale labs and allow the combination of several disciplines in one very small system. These miniaturized chips come along with benefits such as automation, low cost, reduced reagent and sample consumption and precise control [31]. Yet, straightforward data acquisition and analysis of the experimental data still remains elusive. Recently, capillary micromechanics have been used to probe soft gel particles [167] as well as biological cell aggregates (glomeruli) [168]. In this way, the shear modulus and the compressive Young's modulus can be determined. However, this method allows only a throughput in the order of around $1\,\mathrm{cell/min}$. Deformation of lipid vesicles [74, 30, 28, 75, 79, 104, 158] and RBCs in hydrodynamic flow fields under shear is another technique that allows a contact-free and non-invasive investigation. RBCs and vesicles have

been studied experimentally [16, 50, 153, 150, 149, 152, 151] and theoretically [75, 146, 104, 129, 128, 127]. However, the comparison of literature values remains challenging because of different preparation techniques. Additionally, different blood donors increase the variance of the measurement.

In this study preparation techniques are the same for all experiments to increase the accuracy of the mechanical property evaluation. In the experiments the mechanical properties of healthy human RBCs and chemically modified RBCs are measured statically by MPA and IT-AFM. The results are used to identify the influence of the mechanical moduli on flow deformations in hydrodynamic flow fields. RBCs are observed while flowing through capillaries having diameters of 2 μm to 20 μm and quadratic microchannels of 10 x 10 μm. There RBCs reach velocities up to 3500 μm/s. These flow conditions have been chosen because they are in a physiologically regime. The microvasculature consists of venules, arterioles and capillaries with average diameters of 20.6 μm, 13.2 μm and 8.72 μm, respectively [113, 116] and average blood velocities of 107 μm/s, 2030 μm/s and 850 μm/s [8, 116] have been measured. It is therefore essential to investigate the shape probability of RBCs under physiological flow conditions. The slipper shape transition is of a high relevance because the asymmetry in the shape is an important question in circulatory research. Additionally, cells suffering from β-Thalassemia and hereditary Spherocytosis show altered transitions and can be compared to healthy and chemically modified RBCs.

As mentioned in the beginning, RBCs of Camel and Lama are less deformable and do not change their shape although the flow conditions in their cardiovascular system are identical to any other mammal [137]. The stiffness of RBCs of Alpaca were found to have a four times higher bending modulus than human RBCs when performing flickering spectroscopy [173]. So far, only an orientation of the cells of camels and lamas were observed in linear shear stress by taking diffraction patterns on a microscope [137]. However, no data for alpaca RBCs are reported so far. As they belong to the camel family, it indicates that they also do not deform. It is thus important to understand how RBCs of Alpaca behave while traveling through the small capillaries and how they compensate their lowered deformability, although the mechanical stress for the cells is the same as in other mammals. Observing cells while flowing and deforming in microchannels using high speed imaging is a new

method for studying flow dynamics and mechanical properties in detail. For example, in these systems, relaxation experiments were performed for healthy human RBCs. The relaxation time was found to be $\approx 300\,\mathrm{ms}$ [41]. Measuring the relaxation time is a precise method to identify the viscoelastic mechanical properties of red cells. So far there is no measurement of the relaxation time of alpaca or camel RBCs.

Chapter 2

Physiology and Theoretical Background

The main focus of this chapter is the basic explanation of important red cell aspects concerning the structure, the flow motion or the flow environment in order to obtain a better understanding of the experimental findings and discussions.

2.1   Morphology of Red Blood Cells

This section discusses the morphology of human red blood cells that are healthy, chemically modified or diseased. Furthermore, a unique red blood cell structure in the class of mammals is introduced, the RBC of alpaca.

In order to understand the presented results in this thesis, it is important to get in-depth information of structural properties of red blood cell membranes.

2.1.1   Healthy Human RBC

In the case of humans, the diameter of a RBC is around $2R_{cap} = 8\,\mu$m and the height of the rim is $\sim 2\,\mu$m. The concavity, which is located in the center of the cell, has a height of only $1\,\mu$m. Figure 2.1 shows four Environmental Scanning Electron Microscope (ESEM) images of a healthy human RBC. The left image shows human RBCs with their typical discoid biconcave shape having a diameter of $2R_{cap} = 8\,\mu$m. In the right picture RBCs are magnified. One is seen from the top showing the round shape, while the other one is rotated by 90° highlighting the biconcave discoid shape. The thicker rim and thinner

concavity area can be seen. The rim has a thickness of around $2\,\mu m$ and the concavity of around $1\,\mu m$ [126].
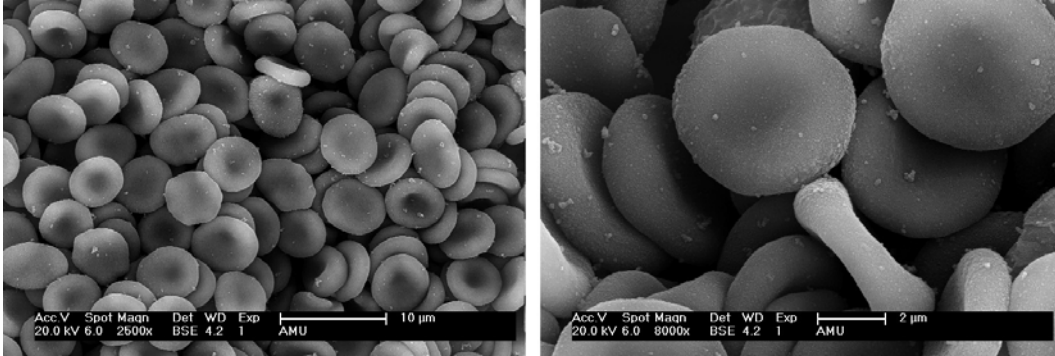

Figure 2.1: Environmental Scanning Electron Microscopy (ESEM) image of healthy human RBCs. The images were taken in the backscattering electron mode. The left image shows several RBCs with their discoid rest shape having a diameter of around $2R_0 = 6\,\mu m$. In the right image, the concavity in the middle of a RBC can be seen. The side view of a RBC shows that the rim has a thickness of around $2\,\mu m$ and the concavity of around $1\,\mu m$.

The RBC architecture of human, and more generally, of the abundant mammals is highly specialized for their main function: delivering sufficient oxygen to all the tissues in the whole body. During erythropoiesis they therefore remove their cell nucleus and cell organelles to increase the space available for hemoglobin, the oxygen binding molecule. In contrast most RBC of vertebrates keep their nucleus and cell organelles. Hemoglobin is the carrier protein responsible for binding oxygen and is the major component of the cytosol. An increased hemoglobin concentration is thus favorable from a physiological point of view. However, not only the inside but also the membrane, is highly optimized for maximum hemoglobin contents. It is manufactured of a lipid bilayer with an underlying cytoskeleton that is anchored by transmembrane proteins. Other cells, such as skin cells, have the cytoskeleton linked across the entire cell.

Figure 2.2 shows a cross-section through the human RBC membrane (from Perrota et al. [109]). The lipid bilayer, which has a thickness of 4 nm [86, 56, 122] is an embedding matrix for proteins. The proteins of the glycocalyx, which project 10 nm [86, 56, 122] from the cell, and the anchoring proteins of the cytoskeleton are dissolved there. Under physiological conditions (the lipid bilayer is in the fluid phase) the proteins as well as the lipids themselves can move freely in the two-dimensional membrane area. The glycocalyx proteins

hardly influence the morphology of RBCs. The composition of glycoproteins only determines the blood group [118]. The anchoring proteins are embedded in the cytoskeleton that plays an important role for the mechanical properties and thus the deformability of the RBC (also see chapter 2.2). The cytoskeleton is kept 10 nm [12, 56, 122] away from the lipid bilayer. The network has a thickness of 20 to 30 nm [12, 56, 122].
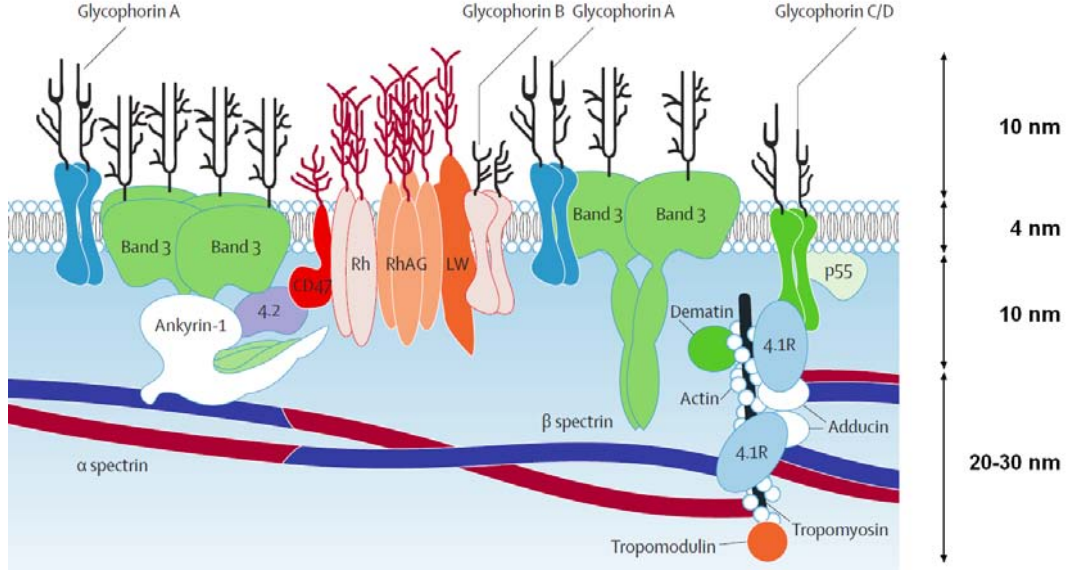
Figure 2.2: Schematic cross-section through the RBC membrane [109]. The glycocalyx projects $\sim 10\,\text{nm}$ beyond the $\sim 4\,\text{nm}$ thin lipid bilayer [86, 56, 89]. Anchoring proteins keep the 20 nm to 30 nm thick skeletal network $\sim 10\,\text{nm}$ away [12, 56].

From a physical point of view, the shape of human RBCs can be explained by the competition between the curvature energy of the membrane (mostly determined by the bending elasticity), the geometrical aspects of the cell (such as fixed surface area and enclosed volume) and the lipid composition of the membrane. The abortion of the cell nucleus during erythropoiesis influences the cell's reduced volume at a fixed surface area effectively [92]. The mean volume of the cytosol is $\approx 90\,\text{fl}$ enclosed by a surface area of $\approx 140\,\mu m^2$ depending on the age of the cell. Younger and denser cells have a slightly higher surface area or volume respectively. Consequently, a characterizing parameter is the reduced volume ν that is given by

$$\nu = \frac{V}{(4\pi/3)R_0^3} \quad R_0 = (A/4\pi)^{1/2} \tag{2.1}$$

, where R_0 is the radius of a sphere with the same area A. Human RBCs are found to have a ratio of 0.6 [130].

Lipid vesicles are simple models for red blood cells. They consist of a lipid bilayer enclosing fluid volume. In the following, two simple models for vesicles that have similar shapes with respect to a given excess area and volume are described. First, the Spontaneous-Curvature Model by Helfrich [57]. The membrane is seen as a two dimensional surface in a three dimensional space. Every surface point has two curvatures C_1 and C_2 respectively. Based on these estimations different shapes can be calculated by minimizing the energy for this system. The corresponding shapes can be seen in figure 2.3.
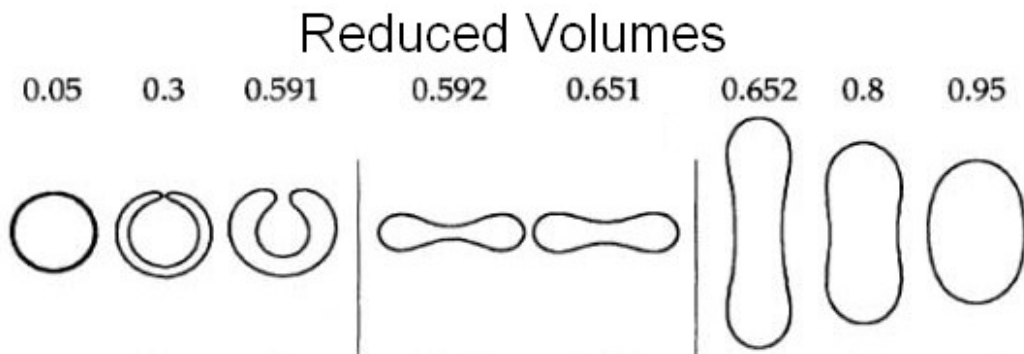
Figure 2.3: Vesicle shapes calculated by Lipowsky (reprint from [90]). The numbers correspond to the reduced volume ν and the two dimensional lines represent the cross-section through the three dimensional vesicle.

Second, the Bilayer-Coupling Model by Svetina and Zeks [144] is equivalent to the Spontaneous-Curvature model. This model treats the bilayer membrane as two mono-layers without any interaction. Furthermore, molecule exchange between the mono-layers is forbidden and the membrane can be stretched laterally. Characterizing shapes of vesicles, having analogous RBC shapes, are shown in figure 2.3. Some symmetric oblate discoid shapes (S) and asymmetric stomatocyte shapes (A) with $V = 0.6$ are shown. Vesicles with an excess area of $\delta A = 1.038$ and a relative bending energy of $\omega = 1.956$ are comparable to the situation of human RBCs.

From both models the discoid rest shape of RBCs can be theoretically characterized.

In the case of hereditary or metabolic diseases, a different rest shape can be observed. For example RBCs enlarge if the organism suffers from a Vitamin B_{12} absence (Addison's anemia), whereas small RBCs often indicate an iron

Surface Area 0.997   1.038   1.060   1.065   1.073

Surface Area 0.43   0.51   0.88   0.95   1.02
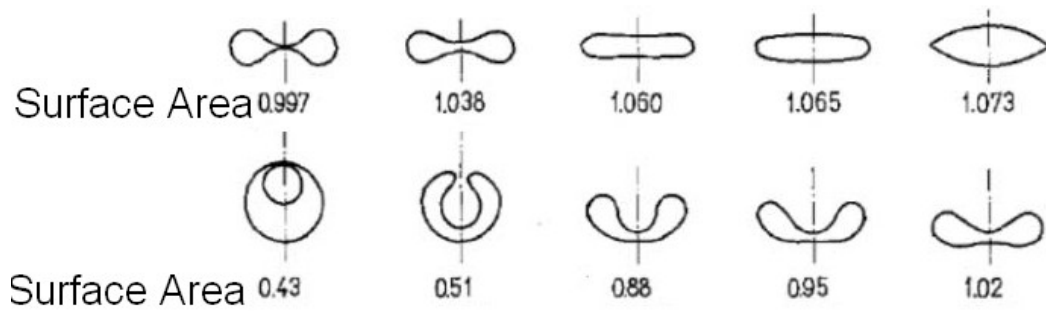
Figure 2.4: Theoretically calculated vesicle shapes by Svetina and Zeks (reprint from [144]). The numbers represent the surface area of the vesicle. The line is the symmetry line of the vesicles. The vesicle shapes are cross-sections through the three dimensional vesicle.

deficiency. Sickle cell or spherocytosis anemia show a deformed structure. Such anemia reduce the cell mean life span and by that a lowered ability to transport oxygen (O_2) to the tissue despite higher production rate [126].

2.1.2 Blood Diseases

In general, there are two types of blood diseases: hereditary and acquired diseases. In the following, two hereditary blood diseases will be discussed thesis: β-Thalassemia and Hereditary Spherocytosis. Both are accompanied by defects in the red cell membrane. The defects have different influences on the morphology or mechanical properties of the RBCs.

β-Thalassemia

Especially in Africa, Burma, Mediterranean regions, the Middle East, India, Indonesia, Malayan Peninsula and Southeast Asia, Thalassemia is high frequent among the total population up to 10 %. Over the last 30 years, both α- and β-Thalassemia have turned out to be the most common monogenic disease in humans [162].

Figure 2.5 shows a micrograph of human RBCs suffering from β-Thalassemia. The cells were photographed subsequently in different osmotic PBS buffer solution (see section 3.1). Compared to healthy human RBCs, they tend to bulge out or even have oval to prolate shapes but always retaining a discoid character. In addition, the mean cell diameter shows a slight increase. However, in the non-severe form, not all of the cells are affected.
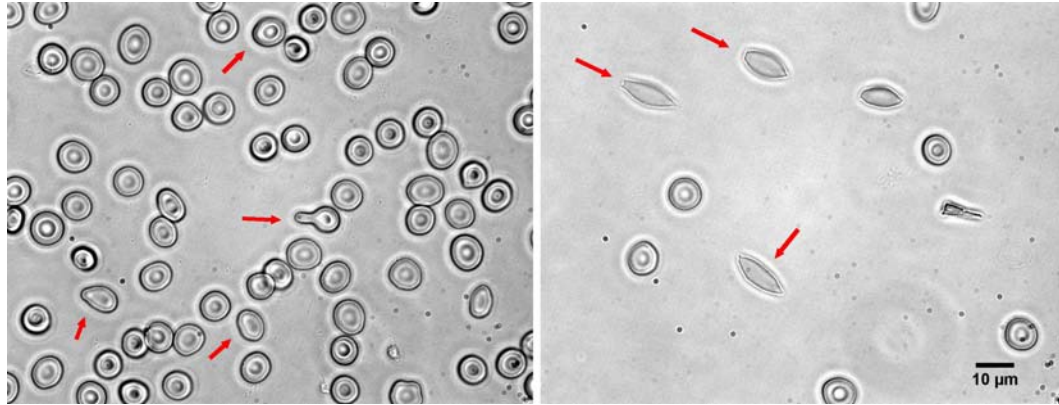
Figure 2.5: RBCs suffering from β-Thalassemia. In comparison to healthy human RBCs, the cells extrude parts of their cell volume. Further on, their rest shape tends to have a stomatocytic structure because the rim seems to be enlarged. In the right image some cells can be seen that form a cigar like shape with two peaked ends. Obviously not all cells are affected, since some of the cells show a typically healthy character. The red arrows mark strongly deformed cells.

In the following, the pathophysiology of the blood diseases is described with respect to shape and modified membrane.

A major characteristic of β-Thalassemia is an ineffective erythropoiesis (production cycle of RBCs). The inefficiency is distinguished by an relative excess of α-globin chains. α-globin is one of the O_2-binding hemoglobin proteins. The increased content of α-globin is accompanied by self-regulatory processes in the cell. They try to lower the α-globin content also resulting in a higher production of degradation products. The degradation products mainly consist of iron. Both degradation products and excess α-globin chains lead to a varied ratio of spectrin to band3 and also affect the function of band4.1 inside the membrane.[131, 125, 107] These membrane proteins are essential for anchoring the cytoskeleton to the plasma membrane and thus affect the deformability (as highlighted in section 2.1.1 and the following section 2.1.3).

Spherocytosis

The most common corpuscular hemolytic anemia in Northern Europe, North America and Japan is the heterogeneous inherited Spherocytosis. It has a prevalence of 1 to 1000-2500 [109]. The anemia has very mild up to subclinical dimensions and patients suffer from chronic haemolysis. The morphology of diseased RBCs is visible by their swollen, spherical shape and change of shape

is accompanied by a membrane surface loss. This increases the volume to surface ratio and lowers cell deformability. The membrane loss originates in defects in the membrane proteins ankyrin, band3, β-spectrin, α-spectrin and protein 4.2.
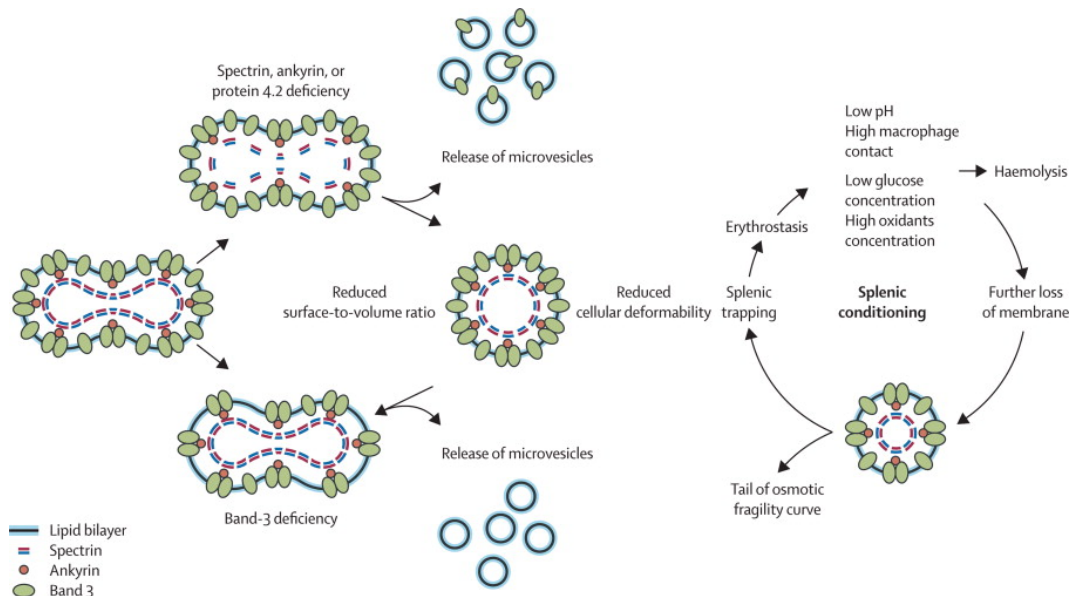
Figure 2.6: Schematic pathophysiology of hereditary Spherocytosis. Depending on the protein deficiency, RBCs can lose their membrane surface area in two ways. A failure of band3 results in the release of microvesicles. In the case of spectrin, ankyrin or protein 4.2 defects, RBCs release microvesicles containing band3 [109, 101].

Depending on the type of heredity, different types of mutations have typical pathophysiological consequences. The mutations lead to a pure deficiency of spectrin, an absence of spectrin and ankyrin, a deficiency of band3, a deficiency of protein 4.2 or a deficiency of the Rh-complex [109]. Mutations of the protein furthermore affect the α-spectrin as well as β-spectrin. A defect of the β-spectrin occurs in around 15 % to 30 % of all patients and is inherited autosomal dominantly. The etiopathology is mild to severe. However, a defect of the α-spectrin occurs in only 5 % of all patients, but shows an even severe course of disease. This deficiency is inherited autosomal recessively [37, 7, 109, 69].

More often defects in the proteins ankyrin and spectrin can be observed. Around 40 % to 65 % of patients in Northern Europe suffer from this type of mutation. It is a mild to severe characteristic and is inherited autosomal, both recessively and dominantly. The ankyrin protein plays an important role in the stabilization of the plasma membrane because it is bound to the β-spectrin

and band3. Ankyrin is a binding site with high affinity to the heterodimer spectrin and is only stable as it is bound to the membrane. Consequently, a defect of the protein ankyrin also includes a defect of spectrin [37, 7, 109, 69].

In contrast, mutations of band3 affect 20 % to 35% of the patients and are inherited autosomal dominantly. This type is categorized as mild to severe. There is a local variety of this type of mutation. In Japan, the occurrence is 45 % to 50 %, whereas in Northern Europe the probability is much lower than 5 % [37, 7, 109, 69].

The pathophysiological effects are independent of the type of mutation and have an altered cell deformability due to a reduced surface to volume ratio. The reduction of cell deformability is shown in figure 2.6 schematically. The cytoskeleton of the diseased RBC is only attached weakly. If the cell is then exposed to shear forces in the cardiovascular system of the human body microvesicles are strangulated. Depending on the type of genetic defect the microvesicles either contain band3 or they do not (see figure 2.6) [109, 101].

2.1.3 Chemically Modified RBCs

Altered deformability of RBCs is known to change the viscosity of whole blood and is correlated with several widespread diseases like diabetes mellitus, hypertension or cardiac infarction indirectly [50, 100, 24]. Diseases like hereditary Spherocytosis, sickle cell anemia or malaria change the viscoelasticity of RBCs directly, due to membrane disorders or dysfunctions [101, 100]. To change mechanical properties of RBCs, chemicals like diamide or aldehydes are often used [50]. For example, aldehydes are known to cross-link hemoglobin and are used as blood substitutes in medical therapeutics [50]. Accordingly, chemical modification of RBCs improves the understanding of single cell dynamics and its relevance to blood flow. The modifications help to adjust and even study the cell mechanics.

As explained in section 2.1, the cytoskeleton can be described as a hexagonal network of spectrin filaments with a mesh size of 100 nm to 200 nm. In the cytoskeleton, spectrin is arranged in tetramers, each tetramer is composed of a head-to-head connected heterodimer. Each heterodimer consists of one α- and a β-chain twisted around each other.

Both, α- and β-spectrin are composed of around 20 subunits that have a length of approximately 106 amino acids. The α-spectrin monomer consists of
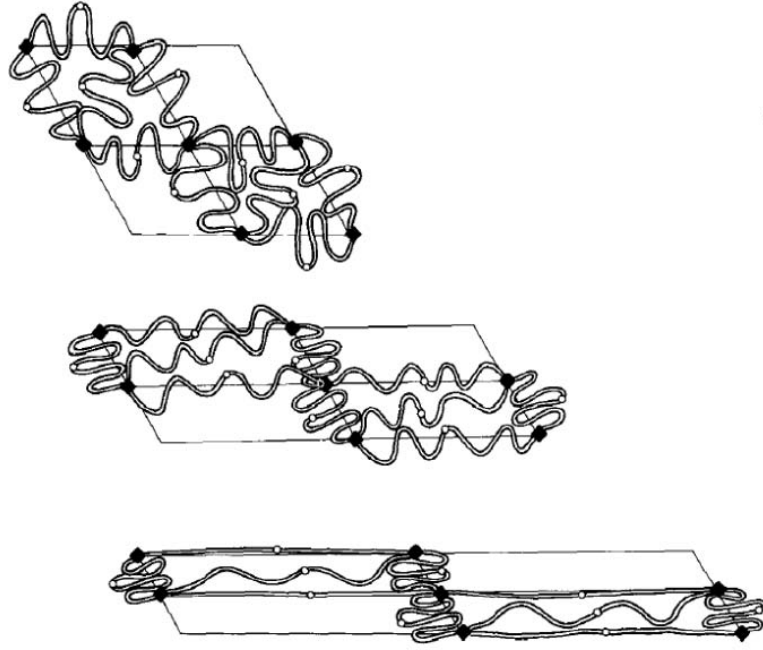
Figure 2.7: Reversible deformation of the cytoskeleton. The above picture shows the α- and β-spectrin fibres without an applied external force, while the lower picture shows the maximum sheared behaviour [23].

20 single subunits and has an ankyrin connection point. It is located at its last third and connects the heterodimer to the membrane. The β-spectrin monomer consists only of 17 subunits without any disruption. The secondary structure of the α- and β-spectrin subunits (compare figure 2.7) is an α-helix. Each subunit is able to unfold separately upon load. This provides an important source of nonlinear elasticity [120, 81, 117, 6].

From a thermodynamical point of view, unstressed α- and β-chains are disordered orientated, so that the entropy is very high. The unfolding of spectrin increases order and lowers the entropy. From an energetic point of view it is unfavorable. Consequently, the unfolding process is reversible (compare Figure 2.7). In simulations and micropipette experiments it was shown that under high shear stress the network softens due to the unfolding ruptures in the spectrin network [6].

To reduce elasticity and alter physical properties of erythrocytes, it is possible to cross-link the membrane proteins of the spectrin network chemically. In the following, the chemical modifications used in this thesis are discussed.

Formaldehyde is a widespread protein cross-linking agent that for example, biologists use to fuse tissue to observe it under the light microscope. The used

formaldehyde suspension is stabilized with methanol. In the measurements, the cross-linking aspect will be shown to be dominant [121].

Figure 2.8: Reaction scheme of aqueous solution of formaldehyde (formaline) with a cytoskeleton protein. Also known as Mannich Reaction [121].

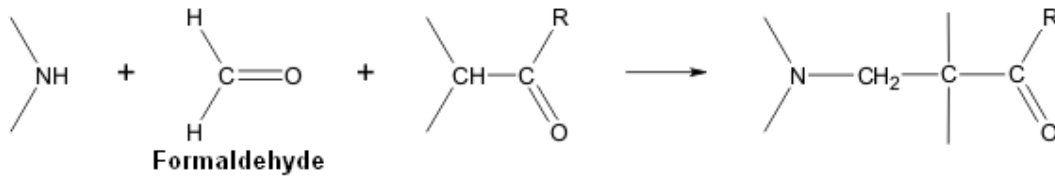Formaldehyde is known to be a highly reactive aldehyde. It stiffens red blood cells or cells due to introduction of new $-CH2-$ groups between amino acid chains. This reaction is known as Mannich Reaction. Since formaldehyde also links haemoglobin inside the cell, this may also have an effect on the inner cell viscosity [121].

Additionally, diamide is used to influence the cytoskeleton because it is known not to influence red cell's inner viscosity [24]. The diamide is able to react with spectrin's cysteine SH (thiol groups) [9]. Therefore diamide modifies the skeleton rather specifically compared to formaline, as the possible reaction centers are limited. Furthermore, in oxidating the spectrin network, protein 4.1 shows a lower ability to amplify spectrin-actin bindings [70]. Experiments on isolated spectrin showed ring structures that may also alter the cytoskeleton [9].

Formaline and diamide modifications are direct modifications of the RBC membrane as they chemically alter the cytoskeleton and increase cell viscoelasticity. In contrast, there are two methods that influence the deformability of the cytoskeleton indirectly: cholesterol modification and variations in the osmotic pressure.

The steroid cholesterol (see figure 2.9 (left)) is one of the main components of the plasma membrane of cells. It consists of four hydrocarbon rings and one connected hydrocarbon chain at the end. The OH-group at the other end is the polar head. The hydrocarbon rings are known to decrease the fluidity of the plasma membrane [83]. As Christian and Haynes [26] reported, it was possible to modify the cholesterol content in the plasma membrane with the help of methyl-(beta)-cyclodextrin (MβCD). The molecule acted as carrier, as the steroid is not solvable in water.
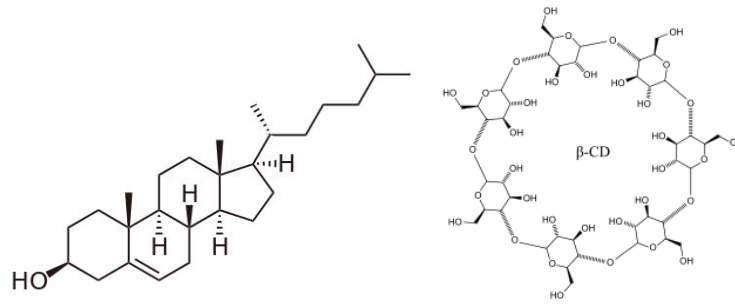
Figure 2.9: (left) The steroid cholesterol. It dissolves in the lipid bilayer of the RBC. This increases the surface area of the lipid bilayer but not of the underlying cytoskeleton. (right) Since cholesterol is hardly solvable in water a carrier molecule is needed. The carrier molecule methyl-(beta)-cyclodextrin is shown in the right. Cholesterol is carried in the middle of the ring and is transported to the cell or the membrane, respectively. [83, 121].

By increasing the cholesterol content the excess area of the lipid bilayer is increased. This increases the initial tension in the cytoskeleton because the two membranes are connected by transmembrane proteins. In contrast, cholesterol depletion lowers the excess area of the lipid bilayer so that the cytoskeleton is compressed (see section 2.2 for the model).

Another possibility to alter cell membrane is discussed in the following. It is an indirect chemical modification. By changing the osmolarity of the surrounding buffer, osmotic pressure is changed. Normally the osmolarity of the blood serum is $c_{osm} \approx 290 \, \mathrm{mOsm}$. A decrease of the value in the buffer solution (hypotonic) increases the inner pressure of the cell because water diffuses into the cell. The situation is vice versa for an increased buffer solution of higher osmolarity (hypertonic).

2.1.4 RBCs from Alpacas

High deformability of erythrocytes is essential for the normal life of mammalians. This outstanding property not only allows RBCs to pass capillaries that are even smaller than their own cell radius, but also reduces the bulk viscosity in large vessels. Furthermore, altered cell rigidity is used by reticuloendothelial system to recycle old cells. The physiological importance of deformability becomes questionable regarding the dynamic behavior of cameloid RBCs. The rest shape of cameloid RBCs is, unlike RBCs of mammalians, an elliptical prolate shape (compare figure 2.10). In this work, Alpaca RBCs

are investigated. The donor animals are property of Chromotek (Planegg-Martinsried, Germany), are healthy and live 484 m above sea level.
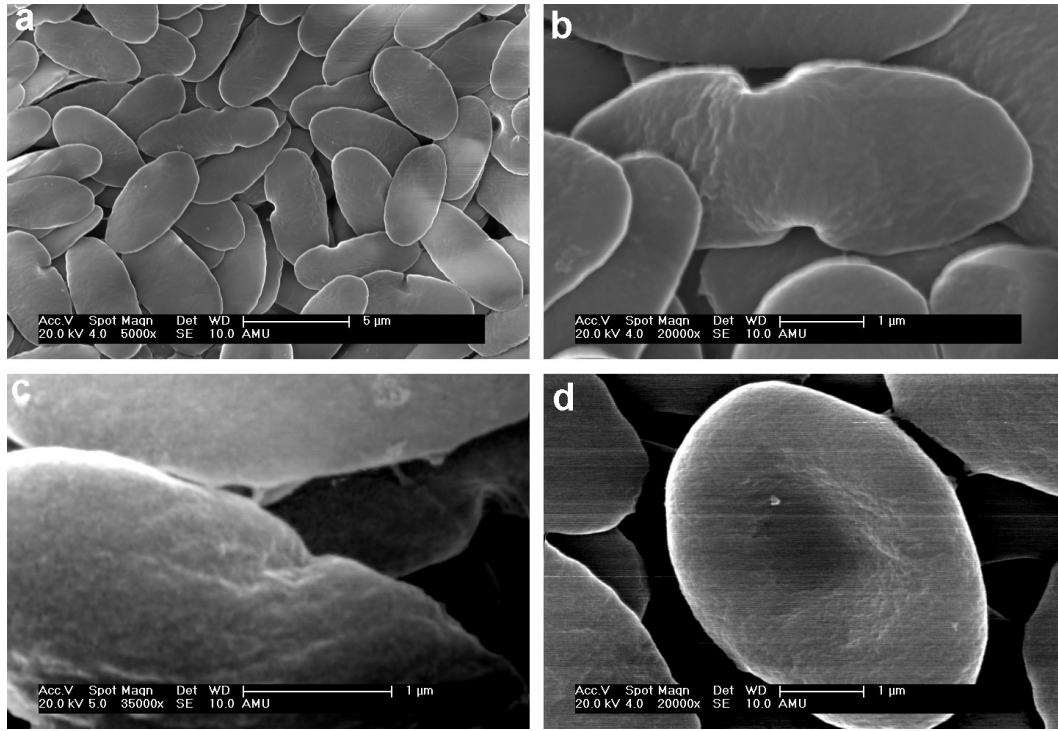
Figure 2.10: ESEM Pictures of Alpaca RBC. (a) A bunch of some cells is seen. The cells show a cigar like shape (flattened ellipsoid). (b) Nearly all cells have typical indentations at the long side of the cells. (c and d) The indentation is magnified and found to be as deep as 342 nm.

To determine the morphology, the RBCs are placed in the ESEM and the pressure is set to around 30 mTorr. The microscope is used in the secondary electron mode and the acceleration voltage is 20 kV. Figure 2.10 shows four typical ESEM micrographs of Alpaca RBCS which are magnified by a factor of 5000 to 35000. Their RBCs have a length of 5.6 µm, a width of 2.7 µm and a height of 1.1 µm. The cells show a semicircular indentation on the side having a depth of around 342 nm. In several studies, similar dimensions have been reported and a flattened ellipsoid was described using SEM-imaging [92, 108]. For the first time, this thesis reports two indentations that are positioned at the long side of the cell opposite one another. These indentations can be as deep as 342 ± 20 nm. So far the indentations have not been discussed, although they are visible on a SEM micrograph of Omorphos et al. [108].

To identify the mean density, RBCs from alpaca were deposited in solutions of five different densities ($1.064\,\text{kg/m}^3$, $1.087\,\text{kg/m}^3$, $1.107\,\text{kg/m}^3$, $1.132\,\text{kg/m}^3$

and $1.160\,\text{kg/m}^3$). For detailed information see appendix A.11. After 18 hours only in the density solution of $1.132\,\text{kg/m}^3$ RBCs were suspended homogeneously, while for the other solutions cells either sank to the bottom or rose to the surface. Consequently, the measured density of Alpaca RBCs is $1.132 \pm 0.027\,\text{kg/m}^3$. In contrast, for healthy human RBCs a value of $1.097\,\text{kg/m}^3$ was measured. The higher density is explained by the higher amount of hemoglobin that RBCs of Alpaca typically contain.

In addition to the unique architecture, alpaca RBCs have also special physiological abilities that are strongly correlated to the RBC shape. Their RBCs withstand a wide range of osmolarity changes as it is the case for dehydration. Another remarkable feature is the fact that Alpacas can live at very high altitudes or change altitude levels quickly without having the need to adjust their hematocrit to that altitude.

Alpaca RBCs are not known to deform in narrow capillaries or at high shear stress. In literature there is no dynamic cell observations of Alpca RBCs. Therefore, this thesis observes dynamic behavior of alpaca RBCs to compare them to human RBCs in contrast to diseased RBCs that show altered mechanical properties and surface to volume ratios as well (see section 4.8.2).

2.2   Mechanical Properties of RBC

As already outlined, the high deformability of RBCs is mainly due to the membrane architecture. Compared to a latex membrane of the same thickness, the RBC is 100 times softer. The membrane would allow the cell to deform by about $250\,\%$ assuming a linear increase. However an increase in surface area of 3 to $4\,\%$ would cause cell lysis [101].

From a physical point of view, there are three mechanical moduli describing the deformability of a RBC: bending modulus κ, shear modulus μ and area expansion modulus K_A. There are different methods for identifying the mechanical moduli of RBCs. In the literature, a suitable technique to measure stress-strain relations to identify the bending rigidity κ is AFM, whereas the shear modulus μ and area expansion modulus K_A are measured by MPA technique [100, 61].

A shear deformation is an elongation of the two-dimensional membrane without either increasing the surface area or bending it. Since the membrane of the RBC is a two-dimensional shell, a constant area extension occurs along

a line at 45° to the extension direction. This deformation behavior is charac-
terized by the shear modulus μ [39, 42, 61]. The relation between the shear
resultant T_S and the ratio λ of the extended and original length is given by

$$T_S = \frac{\mu}{2}(\lambda^2 - \lambda^{-2}) \tag{2.2}$$

Deformation of a RBC when the isotropic expansion of the membrane sur-
face does not either shear or bend, is described by the area expansion modulus
K_A [39, 42, 61]. The simple linear connection between the isotropic tension T
of the membrane and the relative area expansion K_A was evaluated by Evans
et al. [45] to be

$$T = K_A \cdot \frac{A}{A_0} \tag{2.3}$$

Here A/A_0 is the relative change of surface area compared to an initial area
A_0. The modulus K_A is the constant of proportionality between membrane
tension and the fractional increase in surface area (Hooke's law) [100].

To characterize whether bending or stretching forces play the major role
in RBC elasticity the dimensionless Föppl-von-Kármán number can be used.
This number shows the relative importance of shear or bending elasticity and
is given by [88]

$$\gamma = \frac{K_0 R_0^2}{\kappa} \quad \text{with} \quad K_0 = \frac{4\mu K_A}{\mu + K_A} \tag{2.4}$$

R_0 is the mean red blood cell radius, K_0 is the 2D Young modulus of the red
cell membrane and K_A is the area compression modulus. A Föppl-von-Kármán
number γ=150 is the transition at which stretching and bending forces mainly
control the shape of crystalline vesicles [88]. Regarding the incompressibility
of the fluid membrane ($K_A \gg \mu$), K_0 can be assumed to be 4μ and $\gamma \approx 400$
[104] for RBCs. Although these values are close to the validation limit of the
model, it can be deduced that shear elasticity is the dominant parameter of
the RBC shape compared to the bending elasticity.

In the following, a theoretical model that describes the viscoelastic prop-
erties of RBCs by means of springs developed by Boal [12] is used. Figure
2.11 shows a schematic illustration of the RBC architecture to demonstrate

the similarity to the model and the real cytoskeleton system. The view is from inside out of a RBC so that the blue plane in the background illustrates the plasma membrane. The main anchoring proteins ankyrin and band4.1 are depicted as circles and pentagons, respectively. They interconnect the plasma membrane and the hexagonal network consisting of α- and β-spectrin dimers. The network has a six-fold symmetry and can be viewed as a plane of triangular plaquettes. One side-length of a triangle consists of an α- and β-spectrin tetramer.
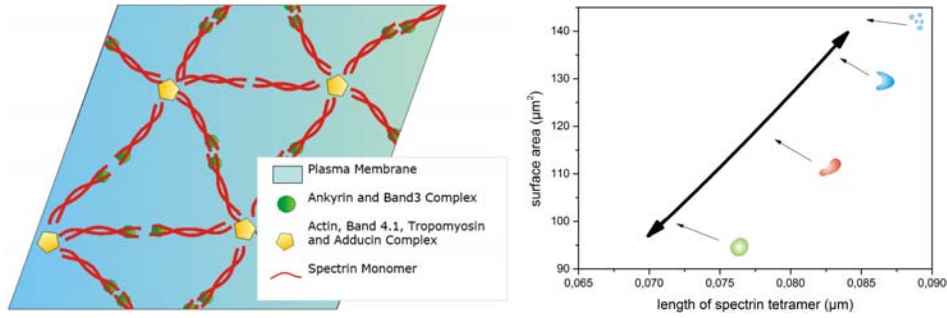
Figure 2.11: (left) Schematic drawing of the RBC membrane. The blue background corresponds to the plasma membrane. The anchoring proteins are drawn as symbols and the spectrin tetramers correspond to springs. (right) Theoretical dependency of spectrin length and surface area is shown. The data line shows the regime where the spectrin can be elongated or compressed. Since there is no defined start or end it is represented by an arrow. The schemes inside the graph represent the shape of the whole cell observed during flow measurements. At very high spectrin lengths the cell lyses.

In the theoretical model, connection points are represented by anchoring proteins. Starting from these points, four springs that model the tetramers spread out in a two-dimensional plane [12]. By applying a two-dimensional tension τ to the spring network the deformation, in form of side-length s expansion, can be simulated. The deformation can be calculated by minimizing the enthalpy $H = k_{\mathrm{spr}} - \tau A$. k_{spr} is the spring constant and A is the area of the network. The complete area of the network is given by the number of triangles times $\sqrt{3}s^2/3$. For zero temperature, Boal finds the shear modulus and the area expansion modulus to be

$$K_A = \sqrt{3}k_{\mathrm{spr}}/2 \qquad (2.5)$$

and the shearing modulus μ is half the area expansion modulus ($\mu = 1/2K_A$).

The model is dominated by the geometry and the single spring constants of the network. In section 2.1.3, the chemical modifications are introduced as cross-links in the network. Diamide introduces cross-links along the spectrin proteins so that the spring constant is modified as follows

$$K_A = \sqrt{3}(k_{\text{spr}} + k_{\text{dia}})/2 \tag{2.6}$$

In the case of aldehyde modification, the spring constants are not affected directly. The introduced cross-links connect neighboring spectrin polymers. Thus, the single triangle size is decreased and the maximum extension length of the triangle is decreased.

$$K_A = \sqrt{3}(k_{\text{spr}}/k_{\text{forma}})/2 \tag{2.7}$$

Figure 2.11 (right) shows the dependency of the surface area and the spectrin unfolding length.

In terms of diamide modification, the time scales of the unfolding process are modified, as the spring constant is influenced directly. Formaline modification decreases the maximum unfolding length. In case of osmotic modifications and cholesterol alterations, the model generates an initial load for the spectrin unfolding.

2.3   RBCs in Flow

2.3.1   Poiseuille Flow

Nearly all measurements presented in this thesis are performed in environments having a Reynolds Number lower than 1.

$$Re = \frac{L\rho v}{\eta} = \frac{\text{Inertial Forces}}{\text{Viscous Forces}}(< 1) \tag{2.8}$$

The so called Reynolds Number as shown in equation 2.8 describes the relation between inertial and viscous forces. In systems having a Reynolds Number lower than one, the viscous forces dominate the inertial forces.

Water is a typical example for a Newtonian fluid. It has a linear viscous flow behavior. The basic equation to describe the flow of a Newtonian fluid is

the so called Navier-Stokes equation (see equation 2.9) [145].

$$\rho\frac{\partial v}{\partial t} + \rho(v \cdot \nabla)v = -\nabla p + \eta\Delta v + (\lambda + \eta)\nabla(\nabla \cdot v) + f \qquad (2.9)$$

This equation uses the principle of linear momentum with respect to Newton's three laws of motion in a given continuum. The vector f includes external forces on a volume element such as gravity force, electrostatic forces. Since only incompressible fluids are used, equation 2.9 can be reduced to equation 2.10 [145].

$$\rho\left(\frac{\partial v}{\partial t} + (v \cdot \nabla)v\right) = -\nabla p + \eta\nabla^2 v + f \qquad (2.10)$$

In general, the Navier-Stokes equation is challenging or impossible to solve analytically, due to the following non-linear term:

$$\rho(v \cdot \nabla)v \qquad (2.11)$$

Two important conditions have to be considered. The first condition is expressed by the Reynolds Number as discussed before. For small Reynolds-Numbers, as in the experiments, the inertial term can be neglected and the viscous term is dominating. In that case, the Navier-Stokes equation can be reduced to the linear Stokes equation 2.12 [145].

$$0 = -\nabla p + \eta \cdot \Delta v + f \qquad (2.12)$$

The second important condition represents the situation in a one-dimensional direct flow in x direction with $v_y = v_z = 0$ and incompressible fluid ($\nabla v = 0$). In this case, the inertia term can be neglected because of the geometry [145].

$$v_x(r) = -\frac{1}{4\eta}(R^2 - r^2)\frac{dp}{dx} \qquad (2.13)$$

Equation 2.13 represents the Hagen-Poiseuille flow profile with its characteristic parabolic shape valid for capillaries with a circular shaped cross section. R denotes the radius of the capillary and r the variable position. A particle placed inside the channel experiences a shear force F due to the parabolic

24

shaped velocity profile [145].

$$F = \tau \cdot A \tag{2.14}$$

In this equation, τ is the shear stress and A is the sheared area.

2.3.2 Particle in Flow

In the following a rigid sphere with radius r_0 is given to explain the slip-velocity for this sphere. Figure 2.12 shows a schematic drawing.
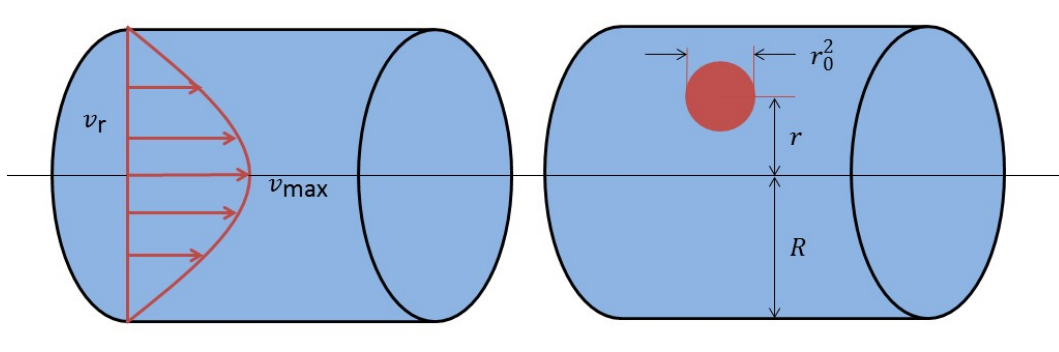
Figure 2.12: Schematic plot. Rigid particle in capillary flow.

The slip velocity is given by,

$$v_s = v_{\max} - v_{\mathrm{RBC}} \tag{2.15}$$

where $v_{\max}$ is the maximum flow velocity in the middle of the capillary and v_{RBC} the velocity of the sphere or red blood cell. Consequently, the slip velocity v_s is defined as the difference of the fluid velocity $v_{\max}$ without particle and the velocity v_{RBC} with particle.

$$v_{\mathrm{RBC}} = v_{\max}(1 - \frac{2}{3}\frac{r_0^2}{R^2}) \tag{2.16}$$

Equation 2.16 calculates the velocity of the RBC in dependency of the maximum flow profile velocity. Finally, the slip velocity v_s is identified by:

$$v_s = \frac{-1}{3}\alpha r_0^2 \quad \text{with} \quad \alpha = \frac{\partial v}{\partial r^2} = \frac{-\nabla p}{2\eta} \tag{2.17}$$

Combined with equation 2.16 the slip velocity v_s can be expressed in dependency of the maximum flow velocity $v_{\max}$, the cell radios r_0 and the capillary

radius R. These parameters can be measured in the experiments easily.

$$v_{\mathrm{s}} = \frac{1}{6}\frac{-\nabla p}{\eta}r_0^2 = v_{\mathrm{max}}(\frac{2r_0^2}{3R^2}) \tag{2.18}$$

2.3.3 Simulating Flow Fields Using FEM

Figure 2.13 shows the design of two different channels. The height (z direction) of both channels is $8\,\mu$m and the length (x direction) is $108\,\mu$m. The smaller part is the inlet, which is $49\,\mu$m long and has a width of $2\,\mu$m. The difference of the two channels is the final width at the end of the channel. The final width of the first channel is $50\,\mu$m and the other one is $100\,\mu$m. Simulations with the software COMSOL Multiphysics were performed to confine the velocity profile decay at the widening. The fluid flows from the constriction to the widening.
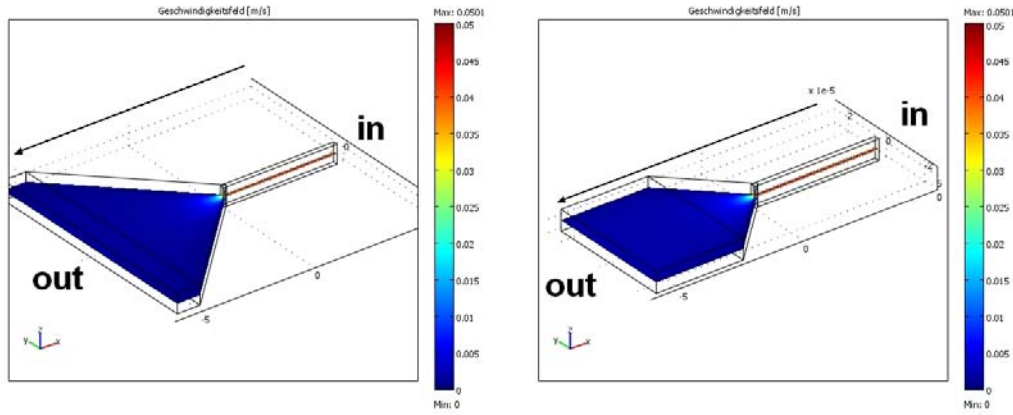
Figure 2.13: Velocity cross section plot and channel dimensions are shown. A pressure difference Δp of $5000\,$Pa is applied. The inlet maximum velocity of $5\,\mu$m/s is thereby in the same range as in the experiments. (Contains data from [38])
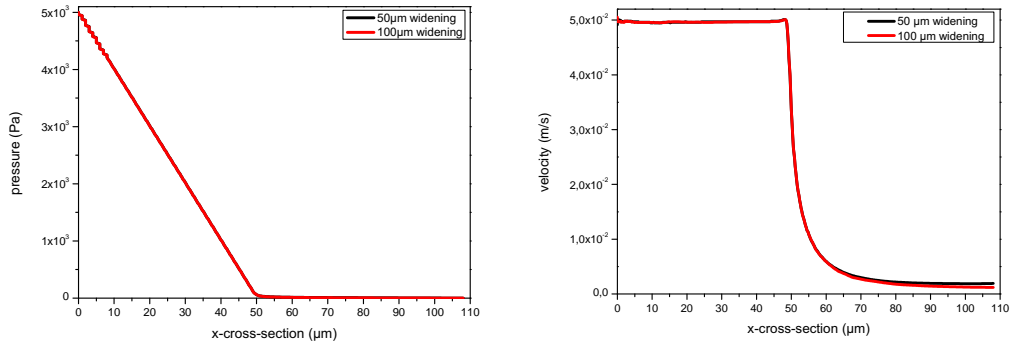
Figure 2.14: Simulated fluid velocity v_{max} (right) and simulated pressure p (left) in the center of the two described channels. The pressure drops very fast over the distance after the outlet whereas the velocity decay is not so fast. (Contains data from [38])

Figure 2.14 shows the pressure and the peak velocity of the profile (exactly in the middle of the channel). The pressure constantly drops at the inlet and

decays more slowly at expansion. The maximum velocity is constant at the small channel part and decays quickly to a constant value after the expansion. Right after the inlet and at the beginning of the widening, a nonlinear behavior can be observed. Summarizing, the $50\,\mu$m broad and $100\,\mu$m broad channels show a similar velocity decay at the expansion despite the constant final velocity.
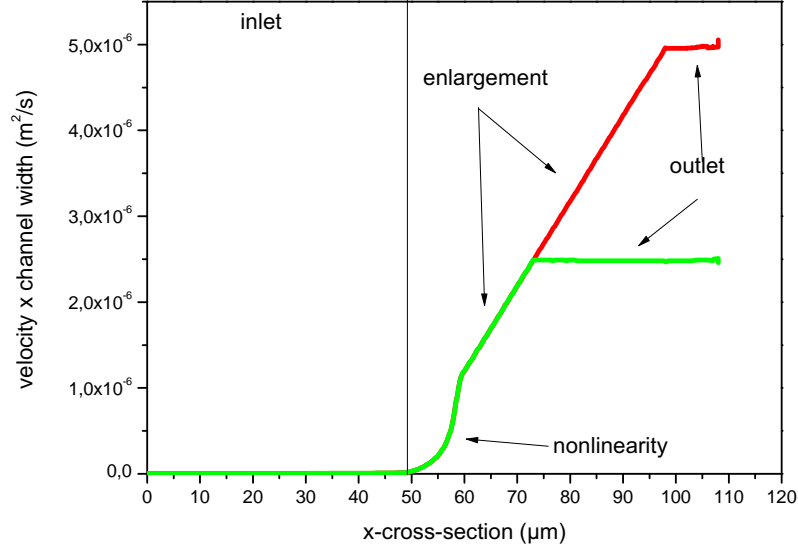
Figure 2.15: Maximum velocity multiplied by the channel width with respect to the position in the middle of the two channels. (Contains data from [38])

Figure 2.15 shows the nonlinearity more precisely. The maximum velocity multiplied by the channel width with respect to the position in the channel does not show a linear behavior over the whole channel, as one would assume by considering the Reynolds-Number.

To prove whether the simulation shows realistic results or not, the volume flow through the channel can be calculated analytically and compared with the simulations. The volume flow through a channel with a rectangular cross section can be calculated as follows [145].

$$\dot{V} = \frac{K \cdot min(b,h)^3 \cdot max(b,h)}{12\eta l}\Delta p \qquad (2.19)$$

with

$$K = 1 - \sum_{n=1}^{\infty} \frac{1}{(2n-1)^5} \cdot \frac{192}{\pi^5} \cdot \frac{min(b,h)}{max(b,h)}\tanh\left((2n-1)\frac{\pi}{2}\frac{max(b,h)}{min(b,h)}\right) \quad (2.20)$$

The analytical results confirm the result of the simulations. The same is valid for the calculated velocity at the inlet.

Further, the FEM simulation technique is used to characterize the 90 ° corner used in a set of experiments later in this thesis (see section 4.9). The flow direction change dictated by the 90 ° corner causes an asymmetric parabolic flow profile. In figure 2.16 (left), the asymmetry is plotted and the simulated shear field is shown (right). The flow profile at the cross-section of the 90 ° corner (see right line at the micrograph inset) is plotted for three different velocities. In the plot, the zero x-position represents the inner corner. Particle flow position is determined by the maximum flow velocity or the position of lowest shear and the lift force is pushing the particle away from the wall. RBCs tend to flow at channel positions of lowest shear. As the simulation shows, the flow profile maximum is shifted from the middle position to the inner side of the corner. Consequently, RBCs pass the corner at the inner side.
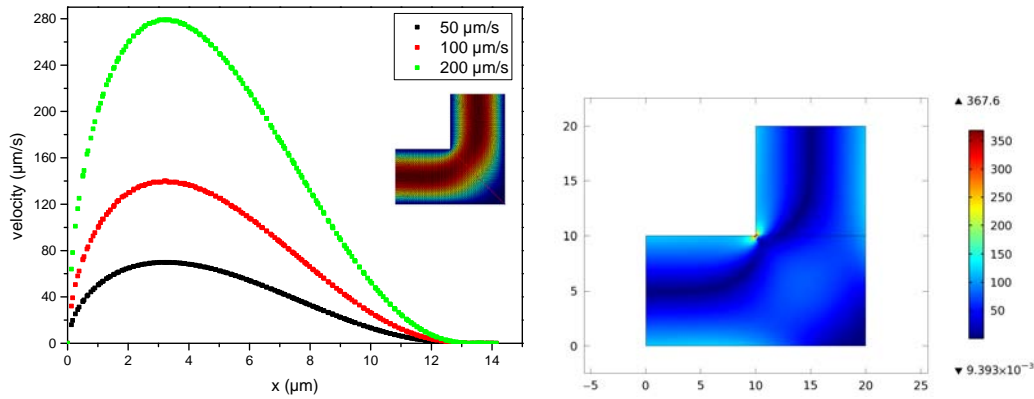
Figure 2.16: (left) Flow profiles at the cross-section of the corner for different mean velocities. The arrow in the inset indicates the dimension and position of a RBC flowing in a 90 ° corner. (right) Shear field of a water fluid at a 90 ° corner. The simulated microchannel has a width and a height of 10 μm each.

Due to the asymmetry in the flow profile, a rotational force component acts on the RBC because the flow profile along the cell dimension is not symmetrical. This rotation part of the RBC velocity v_{RBC} is determined as b and was identified to be

$$b = 0.03v_{RBC} \tag{2.21}$$

The factor 0.03 was measured by the simulation.

2.3.4   SAW Microfluidic

Surface Accoustic Waves (SAW) travel at the interface of two materials. In this chapter it will be explained how they can pump fluids when the interface is glass and water.
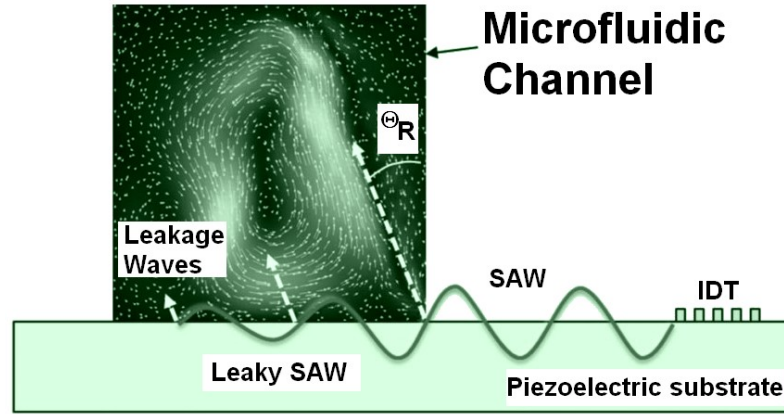
Figure 2.17: Schematic illustration of SAW coupling into microfluidics [5, 31].

In the following, the generation of flow fields by coupling a SAW into a microfluidic channel is described. Figure 2.17 illustrates such a set-up. In the scheme, an IDT is positioned on the left side. It consists of connected metallic electrodes that are on top of a piezoelectric material. The top view of an IDT is a two comb structure that is aligned in a way that always contacts the two combs alternately. By applying an electric field to the IDT, the surface of the piezoelectric material is typically displaced by the order of $10\,\text{Å}$. As two sets of electrodes (two combs) and an alternating current electrical signal in the radiofrequency range are used to deform the piezoelectric material, a SAW propagates on the surface to the left and right (see figure 2.17). The characteristics of the traveling wave are set by the number, spacing and aperture of the metallic electrodes. In addition the electrodes of the IDT are slanted meaning that the electrode width, which is directed perpendicularly to the wave propagation direction, has a gradient. There is thus the possibility of controlling the excitation of the narrow SAW beam along the finger length, because it is dependent on the applied radiofrequency [147, 32, 31]. A precise control of the SAW release is mandatory to define the coupling position in the microchannel. In figure 2.17, the SAW propagation on the surface of the piezoelectric material is illustrated. The amplitude of propagation is damped exponentially with increasing distance from the IDT. In the experimental setup that is used

later the damping is even stronger as PDMS is pressed on the piezoelectric material. Note that there is air over the IDT structure in order to increase the coupled SAW power because damping is prevented. In that way the wave can couple into the water filled channel. Some part of the travelling SAW is refracted due to the viscosity contrast of substrate and liquid and streams into the liquid as a longitudinal wave. The remaining SAW changes to a "leaky SAW" or "pseudo-SAW" [78]. The direction of the longitudinal propagating wave in the liquid is given by,

$$\phi = \arcsin(c_l/c_s) \tag{2.22}$$

where c_l and c_s are the acoustic wave velocities of the liquid and the solid. In the following experiments, the sound velocity of $LiNbO_3$ is $3990\,\mathrm{m/s}$ and $1490\,\mathrm{m/s}$ in water so that $\phi{=}22°$. This coupling is called acoustic streaming [31]. Beside acoustic streaming, acoustic radiation pressure also occurs. The refracted acoustic energy of the longitudinal coupled wave can act on the fluid medium and its particles themselves. However, in the experiments the SAW couples perpendicularly to a parabolic flow field. Thus, no further prediction of the flow environment could be given in this experiment.

2.3.5   Dynamics of a RBC in Flow

In a living system, RBCs represent half of the blood volume. Observations of single RBC at whole blood concentration in artificial systems is difficult. The total number of RBC covering each other is just to high. Therefore low hematocrit experiments enable the observation of single RBCs. In principle, RBCs are subjected to two flow environments in living systems: On the one hand, a linear shear flow as is the case for positions close to the wall in large vessels and on the other hand, a parabolic shear flow such as RBCs are exposed to in thin capillaries.

Figure 2.18 shows the two main shear fields. A linear shear field (top) can be produced in rheometers. There a fluid is in between two plates. The plates rotate in contrast to each other. Due to the friction of the fluid molecules, the flow is highest near the moving walls and has a zero shear position in between. In a rheometer in which a cone and a plate rotate with the same velocity, the zero shear position is exactly in the middle of the two plates (as in the top image). The resulting field can be separated in an elongational component and

linear shear field

parabolic shear field
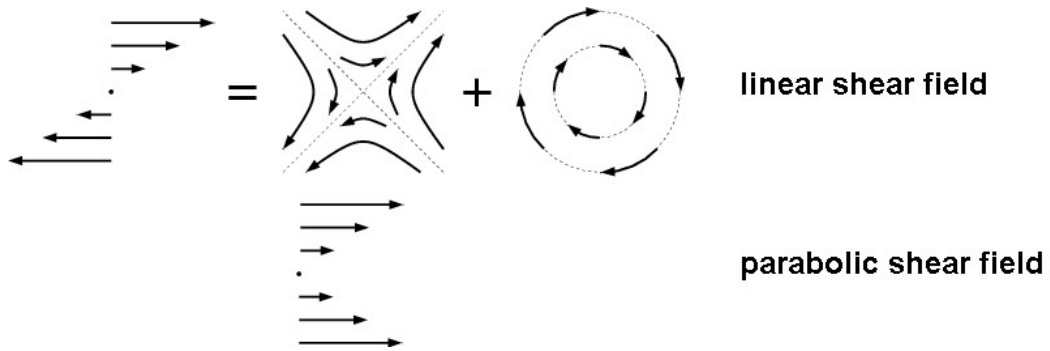
Figure 2.18: The two flow fields which occur in the used fluidic devices. The linear shear field (top) can be separated into a rotational and an elongational component. This field can be produced in a rheometer where a ground and a top plate are rotated against each other. The parabolic shear field is shown at the bottom. This is the typical shear field in a cross-section of pipettes or channels. (Modified from [4])

a rotational component.

Poiseuille flow has a parabolic flow profile. It can be seen in the bottom of the figure 2.18. The flow velocity in channels or pipes is highest in the middle of the structure and lowest at the walls. Consequently, the shear forces are highest in the area of the wall. Near the flow boundary, around a third of the channel diameter, the situation of the particle is approximately the same as in a linear shear field. There all velocity vectors increase and shear vectors decrease toward the middle of the flow.

In the following it will be discussed how RBCs flow in these two kinds of flow fields.

Stretching   Tumbling   Tanktreading   Swinging

Figure 2.19: Flow motion of single RBCs in linear flow profiles: Stretching (left), Tumbling (left middle), Tank-treading (right middle) and Swinging (right). In channels with a width around 3 times broader than the cell the situation is the same as in linear shear fields for RBCs and they show the same flow behavior. (Modified from [51])

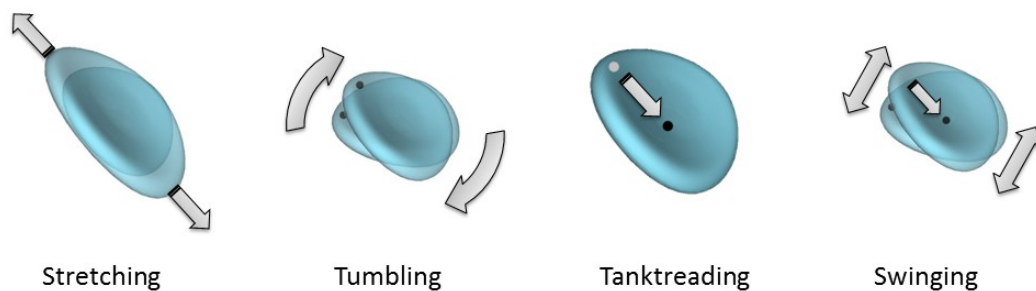RBCs exhibit an amazing variety of flow motions in linear shear flow. With increasing shear stress the RBC is elongated or stretched moderately (see figure 2.19 left). At higher shear stress, the cell starts to tumble, which means the orientation angle of the cell changes randomly (see figure 2.19 left middle). Upon higher shear stress, the fluid membrane of the cell starts to rotate around the cytosol while the orientation angle of the cell remains fixed (see figure 2.19 right middle). Vacillating-breathing or swinging (see figure 2.19 right) is an intermittent flow behavior between tumbling and tank-treading. In this case the long axis undergoes oscillations in relation to the flow-direction, while the shape shows breathing [3, 48, 51].
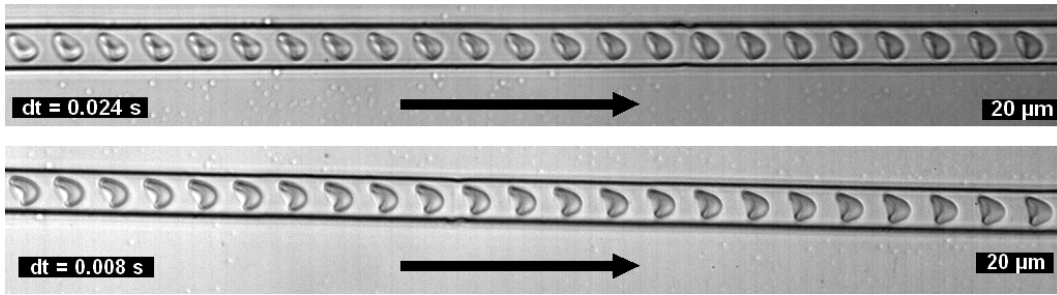
Figure 2.20: Two time-dependent overlays of a single RBC in a 10 x 10 µm PDMS microchannel (top) show a RBC that transforms into a slipper shape and (bottom) a RBC that transforms into a parachute shape.

These flow motions can also be observed near the wall of round or quadratic shaped microchannels having diameters of $2R_{cap} = 30$ µm. Approximately there the flow conditions correspond to a linear shear field.

In parabolic shear fields, the RBC has different flow characteristics. With increasing shear stress, the cell starts to change its shape. Two other shapes, different from the discocytic rest shape, are reported in the literature: the slipper shape (see figure 2.20(top)) and the parachute shape (see figure 2.20(bottom)) [104, 75, 146, 153, 4, 133]. Their occurrence will be investigated in the following experiments as Abkarian et al. [4] reported slipper shapes only at very high shear stress after the parachute shape, whereas Tomaiuolo et al. [153] reported their occurrence already at moderate shear stress. Recently, Tahiri et al. [146] simulated a shape phase diagram to describe all shapes theoretically.

Chapter 3

Methods and Materials

This chapter describes methods and materials used for investigating RBCs in static and dynamic experiments. Detailed step-by-step protocols are attached in the end of the thesis (see appendix A).

3.1 Sample Preparation

In this section, the RBC preparation and all other preparation of solution are explained in detail. All preparation steps were performed at room temperature. For storage the prepared solutions should be kept in the fridge at $T=8\,°C$ because blood samples showed a decreased lifetime at room temperature. The cells lysed and showed altered rest shapes in experiments when not freshly prepared or stored at room temperature.

3.1.1 RBC Preparation

Healthy human whole blood samples were provided by the Klinikum Augsburg (Augsburg, Germany) on a voluntary and anonymous basis. They were transported and ready for preparation within $t=3\,h$ after withdrawal. Chemically modified RBCs were produced from the whole blood stock donated by the Klinikum Augsburg. Whole blood samples from alpaca were donated by ChromoTek GmbH (Planegg-Martinsried, Germany) and reached the lab within $4\,h$ after withdraw on the same day. Spherocytosis blood was donated by patients of the Haemoglobinlabor at the Universitaetsklinikum Ulm (Ulm, Germany) on a voluntary and anonymous basis. β-Thalassemia blood was donated on a voluntary basis by Arturo Castro Nava, who joined the research group for a

summer course. He suffered from β-Thalassemia since birth. The blood was obtained by self withdrawal.

Whole blood was diluted in phosphate buffered saline (PBS) to a concentration of c=30 vol.%. By several centrifugation steps, the RBCs were isolated. Due to their higher density they are concentrated on the ground. Exact preparation steps are given in appendix A.5. In the end, a stock RBC solution with a final hematocrit concentration of 2 vol.% was prepared. Depending on the type of experiment, RBCs were diluted to even smaller concentrations. The RBCs from the stock solution were used within t=12 hours after preparation and stored in the fridge.

3.1.2 Chemical Modification

Some RBC were chemically modified by formaline (c^1_{for}= 18.4 wt % and c^2_{for}= 36.8 wt. %) or diamide (c^1_{dia}= 0.34 wt. % and c^2_{dia}= 0.68 wt. %). The chemicals were purchased from Sigma Aldrich, Germany. The RBCs were incubated in a solution of PBS and different chemicals for 10 minutes (see table 3.1). Finally, three centrifugation steps (see RBC Preparation) with fresh PBS stopped further incubation.

Chemical	Concentration	Incubation time
Formaline	18.4 wt%	10 min
Formaline	36.8 wt%	10 min
Diamide	0.34 wt%	10 min
Diamide	0.68 wt%	10 min

Table 3.1: Chemicals to modify the erythrocyte membrane, with concentration and incubation time

3.1.3 Working Solutions

For IT-AFM measurements, around 3 µl of the RBC stock solution is added to a petri dish containing PBS and 1 mg/ml of BSA. In micropipette aspiration measurements, the BSA concentration is 5 mg/ml, to prevent adhesion to the glass micropipette.

3.2 Flow Device Fabrication

This section describes the manufacturing of the flow devices used in the thesis. In general, rectangular-shaped PDMS microchannels and round shaped glass capillaries were used.

3.2.1 PDMS Microchannel

In the beginning, the channel structure is designed with the help of a CAD program (AutoCAD 2013, Autodesk). It is important that the structure is drawn as one straight line; otherwise the beam produces failures in the final mask production. Once the channel is designed, it has to be transferred into eLine software.

Using standard soft lithography and the chrome mask, a master is built of SU-8 resist. The master is then covered with PDMS to transfer the structure. Afterwards the PDMS is bound with an oxygen plasma to a glass slide. The final channel has a rectangular cross-section, having a width and height of 10 µm. (PDMS; Dow Corning, Midland USA)

In the case of PDMS channels, two pipette tips (2-200 µl) are plugged in the inlets of the channel. They serve as reservoirs to pump the RBCs through the channel.

3.2.2 Glass Capillary

Capillaries used for capillary flow experiments are produced in the same way as micropipette aspiration capillaries. The borosilicate glass capillaries are strongly and fast pulled using pipette puller to have a very small taper angle and opening diameter of 3 to 4 µm (see appendix A.3).

Figure A.9 shows a latex bead inside a glass capillary. Depending on the surrounding medium the capillary distorts the projected sphere along the capillary because it acts as an optical cylinder lens. A surrounding medium of the same refraction index (e.g. PDMS or water) prevents the optical distortion.

3.3 Experimental Setups

All measurements were performed on an inverted light microscope Zeiss Axiovert 200M (Zeiss, Jena, Germany) at room temperature.
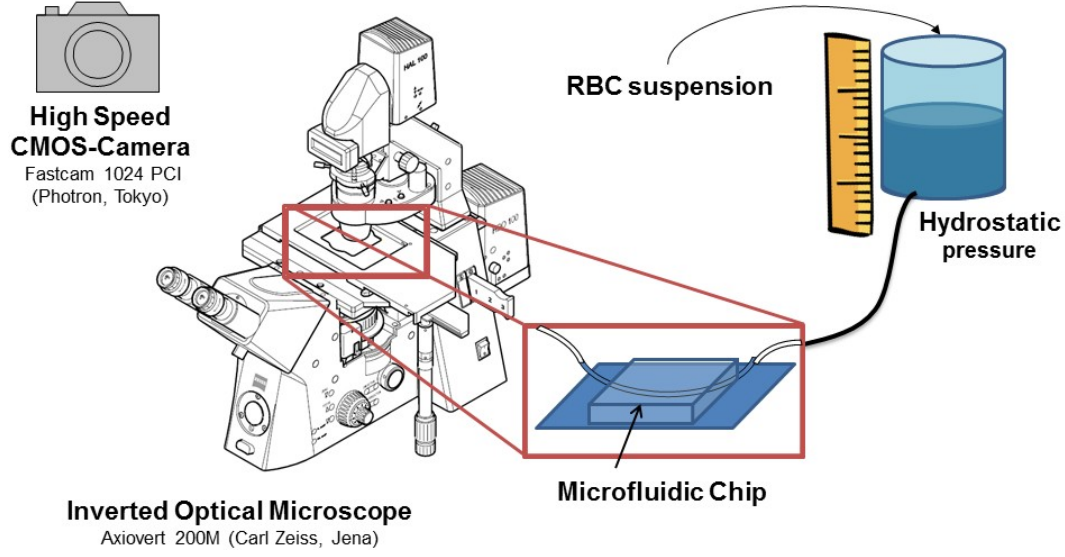
Figure 3.1: Typical microfluidic setup. An inverted microscope having a maximum magnification of 63 x (oil immersion lense) is used to observe the RBC optically.

Magnification	Photron (µm/pixel)	Hammamatsu (µm/pixel)
2.5	6.8	2.59
10	1.7	0.645
20	0.85	0.323
40	0.425	0.161
63	0.2698	0.102

Table 3.2: Conversion factors of the Photron and Hammamatsu cameras in dependency of the magnification.

3.3.1 Micropipette Aspiration Method

Borosilicate glass capillaries were pulled in a pipette puller to have a long parallel end with opening radii smaller than 1 µm (detailed fabrication steps in appendix A.4). The capillary radius was measured by optical microscopy. It was then mounted on a microstage and the tip is dipped in a PDMS chamber (w=1 cm x l=1 cm x h=0.5 cm) filled with working solution and RBCs.

3.3.2 Indentation Type Atomic Force Microscopy

IT-AFM measurements were carried out using a Nano Wizard I, (JPK Instruments AG, Berlin, Germany) with 100 µm x 100 µm lateral scan range and 15 µm vertical range. The IT-AFM was mounted on an inverted optical micro-

scope (Axiovert 200, Carl Zeiss MicroImaging GmbH, Göttingen, Germany) equipped with a CCD camera (The Imaging Source Europe GmbH, Bremen, Germany), which allowed the localization and identification of the RBC of interest. Additionally the rough positioning of the tip in the region of interest above the cells was possible. For reduction of ambient noise, the whole setup was placed on an active isolation table (Micro 60, Halcyonics, Göttingen, Germany) inside a $1\,m^3$ soundproof box. The indentation experiments were carried out using silicon nitride cantilevers (MLCT IT-AFM-Probes, Bruker, Mannheim, Germany) with a nominal spring constant of $0.01\,N/m$ and a pyramidal tip having a nominal tip radius of $15\,nm$. All measurements were carried out in PBS buffer at room temperature. The IT-AFM was used in the force spectroscopy mode and data acquisition and force curve analysis were carried out with the software JPK SPM Desktop and JPK Data Processing (JPK Instruments AG, Berlin, Germany).

3.3.3   Calibration of the IT-AFM

The calibration process was performed as described below. For the sensitivity determination, the cantilever was lowered with stepper motors close to the bottom of the petri dish. Piezo and JPK software automatization were then used to find the petri dish surface. The automatic control lowered the cantilever with the help of a piezo motor in very small increments while measuring the deflection. This was performed very rapidly until the cantilever showed a deflection caused by a strong bending through touching the surface. The surface was defined as a reference height. While the tip indented into the surface the system measured the voltage of the detector in dependency of the height given by the piezo. For positive piezo heights, the measured voltages were positive. Negative piezo heights corresponded to an indentation and bending of the cantilever. Consequently, for measured indentations values increases linearly. The sensitivity was then identified by determining the slope of this increase and measured quantity is expressed in nm/V. For a better calibration, the sensitivity was determined three times. In the next step, the cantilever was lifted from the surface to measure the spring constant k of the cantilever. For the spring constant identification, the Brownian motion of the cantilever was used. The thermal noise spectrum of the free mounted cantilever was measured. The measured cantilever fluctuation was a function of frequency. The

signal to noise ratio increased over time and the cantilever resonant frequency became a sharp peak in the spectrum. For constant temperature the resonant frequency depends only on the spring constant of the cantilever $k = k_{\mathrm{B}}T/P$. Here T corresponds to the temperature and P to the resonant frequency [67].

3.3.4   Flow Device Measurement

Flow measurements were either carried out in PDMS microchannels or glass capillaries. PDMS microchannels have a precise channel design in two dimensions. In contrast, glass capillaries always show a small taper angle, even if it is small, that allows flow experiments under constant flow conditions only for a certain channel length. Independently of the flow device, the measurements were performed in a similar way. The flow device was mounted onto the stage of an electronic microstage. The microfluidic device experiment is performed on an inverted light microscope.

3.3.5   SAW Manipulation

For the SAW manipulation experiments, a PDMS based replica had to be aligned on the SAW carrier. A small volume of isopropyl alcohol was thus pipetted on the SAW carrier that was mounted on an inverted microscope. The PDMS is then aligned to have the channel structure and the microchannel perfectly on top of each other. This was necessary because the IDT should not be covered by PDMS to reduce and to prevent damping. A tapered IDT having an aperture of $500\,\mu$m and 60 finger pairs was used in the experiment. Its wave lengths were between $24.25\,\mu$m and $23.0\,\mu$m.

3.4   Data Acquisition

All experiments performed on the microscope were recorded using optical cameras. A CMOS camera Hamamatsu C8484-05G (Hamamatsu, Herrsching am Ammersee) and a high speed CMOS camera Fastcam 1024 PCI (Photron, Tokyo) were used to save the optical light from the microscope digitally. For data recording and analysis the programs Photron FASTCAM Viewer (Photron, San Diego) and ImageJ (National Institutes of Health, USA) were used. Additionally, custom made software programs were written in Visual

Basic to facilitate efficient data analysis. Simulations were performed with the help of Comsol Multiphysics (COMSOL AB, Stockholm) that offers the possibility of finite element method simulations (FEM simulations).

Chapter 4

Results and Discussion

In this chapter, all experiments are shortly motivated, described in detail and finally discussed. In the experiments, healthy human RBCs, chemically modified human RBCs, human RBCs suffering from Spherocytosis and β-Thalassemia were investigated. Furthermore, RBCs from alpaca, having an abnormal prolate rest shape, were tested and compared to the typical biconcave discoid cells of mammals. The major flow devices, used for experiments, are glass capillaries having a round shaped cross-section or PDMS microchannels that have a rectangular square shaped cross-section.

In the beginning, static properties of RBCs were investigated. In materials science, the stress-strain relation helps to identify mechanical properties of materials. However, cells have anisotropic material parameters because of their complex architecture. This makes the same identification of a stress-strain relation very challenging. In this thesis, the static mechanical parameters were obtained by two different methods: Micropipette Aspiration and Indentation Type Atomic Force Spectroscopy.

Then, microfluidic devices which characterize the dynamic cell mechanics and flow behavior under different flow conditions are introduced. The alpaca system was shown to be special among the RBCs of mammals. Besides the characterization of their flow motions the cells were periodically deformed to identify their viscoelastic properties.

4.1   MicroPipette Aspiration

To study mechanical properties of RBCs is crucial for understanding their response to stresses in the circulatory system or capillaries inside tissues. For materials (e.g. steel) the mechanical parameters are obtained from the stress-strain relation. The small size of RBCs and their very soft character make it challenging to obtain a stress-strain relation easily. Evans [39], Skalak [135] and Hochmuth [61] developed a technique to investigate the shear modulus of living cells using a very small capillary in which the cells are aspirated. In this technique, the position of the aspirated cell volume inside the pipette is measured depending on the applied pressure. The stress-strain relationship can thus be obtained from the applied aspiration pressure and the membrane geometry and reveals the shear elasticity μ [99, 23, 35, 60]. Typical values from previous studies indicate μ=$1\,\mu\mathrm{N/m}$ to $13\,\mu\mathrm{N/m}$ [39, 58, 43, 82, 85, 135]. This high variance of the value may have several reasons. RBCs are known to slightly change their mechanical properties during their lifetime of $120\,\mathrm{days}$. Another very important fact is the different protocols for cell preparation. In addition, most studies used different donors for different experiments which makes it hard to compare because of the large biological variance.

However, this study attempts to correlate the mechanical properties of the red cells. Therefore, it is necessary to perform MPA measurements on RBCs in the same environment as in the flow experiments. In that way, the results of MPA can be directly correlated to flow deformation experiments, described later in the thesis. Another important point that makes MPA measurements necessary is to identify the influence of chemical modifications of the cells. They are modified using formaline and diamide in a high and low concentration to increase the mechanical properties to mimic blood diseases.

4.1.1   Aspiration Behavior of RBCs

In the beginning of a MPA experiment, RBCs were pipetted into a covered PDMS chamber through a small opening at the side of the chamber. The chamber was sealed with silicon paste on a glass slide that was mounted on an inverted microscope. The micropipette was introduced into the chamber through the same small opening and an area of interest with suitable cells was searched by moving the microscope stage. This was typically identified by an area where only a few cells were lying non-touching on the bottom of the cham-
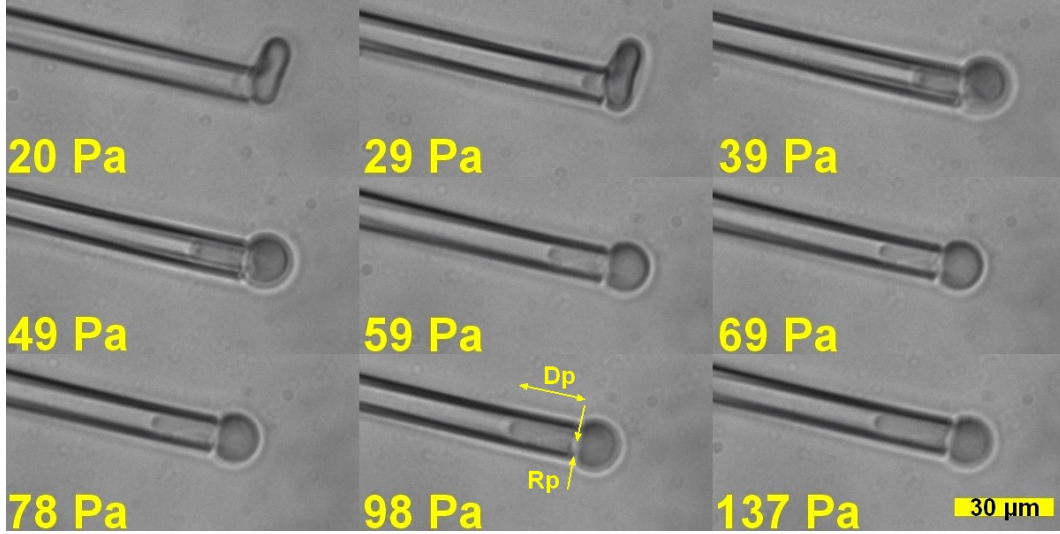
Figure 4.1: Typical image stack of a single MPA measurement of a healthy human RBC. The capillary radius R_P is around 1.2 µm. The cell is aspirated into the capillary with increasing pressure ΔP. The distance from the end of the capillary to the aspirated cell volume inside the capillary defines the aspiration length D_P.

ber. With the help of the micromanipulator, the glass capillary was brought closely to a RBC. The pressure in the glass capillary was decreased by lowering a height-adjustable reservoir attached to the other end of the microcapillary. The cell was now slightly aspirated and lifted from the ground of the chamber by raising the capillary with a micromanipulator. Finally, the pressure in the capillary was adjusted to have the cell aspirated very weakly in front of the capillary. This position marks the zero pressure point ($\Delta P = 0$) and zero aspiration length ($D_P = 0$). The data acquisition was then started. Upon lowering the height-adjustable reservoir the cell was aspirated deeper into the micropipette. There had to be at least 1 min between two measurements to let the cell equilibrate and the meniscus to adopt a constant position [39]. The height difference Δh of the reservoir and the microscope stage was used to calculate the aspiration pressure ΔP hydrostatically by $P(h) = \rho g h$. The system permitted pressures between $1\text{Pa} < \Delta P < 10\text{kPa}$ to be set. The aspiration length is directly measured from the microscopy image. The measured pixel lengths were converted to SI-units using the corresponding conversion factor (see section 3.3). A stack of images of a single MPA measurement can be seen in figure 4.1.

In figure 4.2 a typical micropipette aspiration measurement is plotted. It

shows the dependency of the aspiration pressure ΔP multiplied by the capillary radius R_P against the aspiration length D_P normalized by the capillary radius R_P. In contrast to the measurement points, the curves do not represent a single aspiration measurement but a linear fit to 10 single measurements. In general, there are two regimes. The first regime is limited by aspiration lengths of $1 < D_P/R_P < 4$ and the second one by $4 < D_P/R_P$. To identify the shear modulus μ the first regime $1 < D_P/R_P < 4$ is used. As described in section 2.2, it can be determined using equation 4.1. Here, $a_1 = 2.45$ and $a_2 = -0.63$ are theoretical constants. The offset pressure to hold the RBC at the pipette tip in the beginning of an experiment is being considered [39].

$$\frac{D_P}{R_P} = \frac{a_1 \Delta P R_P}{\mu} + a_2 \tag{4.1}$$

For all modifications, a characteristic threshold at which the aspiration length strongly increases with a small change in pressure is observed. This behavior is more pronounced for chemically treated RBCs and occurs at values $2 < D_P/R_P < 4$. Note that this coincides with the approach of the upper limit of validity of equation 4.1. The equation is only used to evaluate the shearing modulus. Higher aspiration pressures would also take into account that the membrane is stretched.

Eventually, above $D_P/R_P=7$ no data points can be obtained because membrane compartments in form of microvesicles and small buds are pinched off. The upper limit is correlated to materials having μ of around $\mu=6\,\mathrm{mN/m}$ which is 1000 times larger than measurements performed in the literature [41].

In the figure 4.2, measurements of healthy human RBC (black squares) and chemical modifications are shown. RBCs are modified by formaline of two concentrations of $c_{for}^1=18.4\,\mathrm{wt\%}$ (red circle) and $c_{for}^2=36.8\,\mathrm{wt\%}$ (green triangle) and by diamide of two concentrations of $c_{dia}^1=0.34\,\mathrm{wt\%}$ (blue turned triangle) and $c_{dia}^2=0.68\,\mathrm{wt\%}$ (purple diamond). Additionally, RBCs suffering from β-Thalassemia (yellow triangle) are presented. Furthermore, measurement data from Evans [41] are plotted as a reference for the measured healthy RBCs.

The measurement data for healthy and human RBC reveal a shear modulus $\mu_{healthy}=6.8\,\mathrm{\mu N/m}$ which compares well to $\mu=7\,\mathrm{\mu N/m}$ that Evans [41] published. In general, RBCs modified with formaline show increased val-
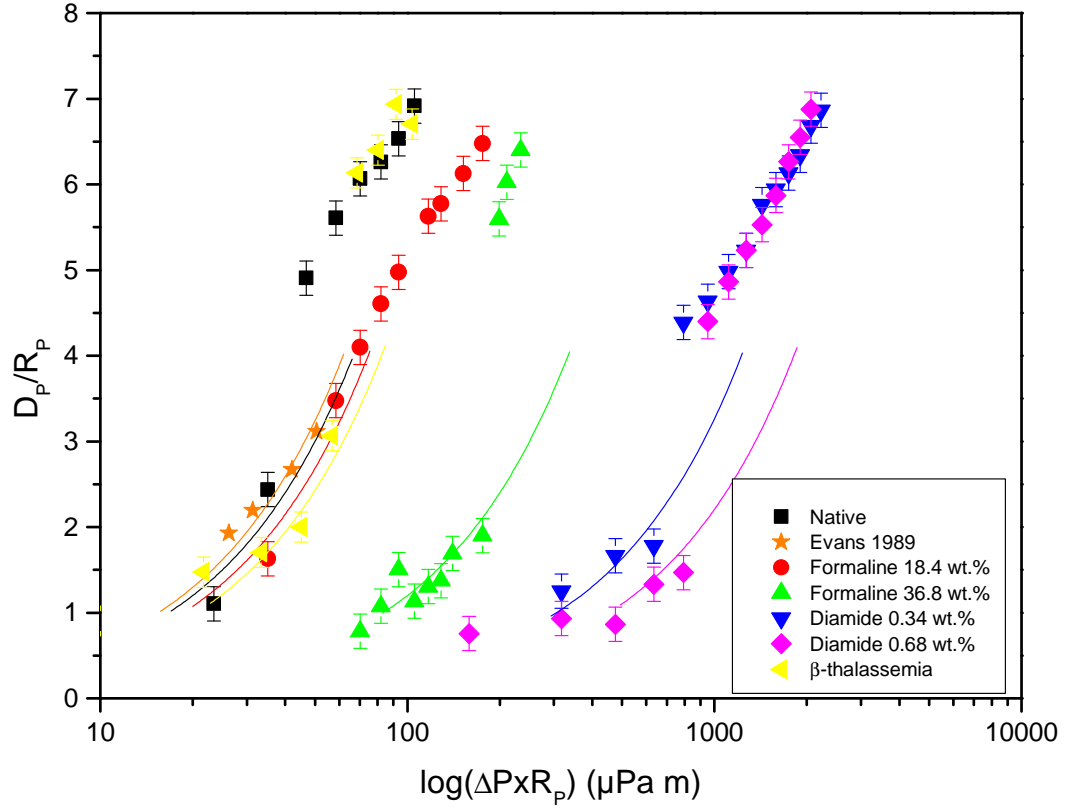
Figure 4.2: MPA of native (black squares) and chemically modified RBC. RBCs are modified by formaline of two concentrations of c_{for}^1=18.4 wt% (red circle) and c_{for}^2=36.8 wt% (green triangle) and by diamide of two concentrations of c_{dia}^1=0.34 wt% (blue turned triangle) and c_{dia}^2=0.68 wt% (purple diamond). Additionally, RBC suffering from β-Thalassemia (yellow triangle) are presented. The graph shows the aspiration length D_P normalized by inner capillary radius R_P versus applied pressure ΔP multiplied by inner capillary radius R_P. The x-axis is logarithmic. The slope in the regime $1 < D_P/R_P < 4$ allows the determination of the shear modulus. Further aspiration lengths reveal the membrane expansion modulus K_A only if the membrane is no longer sheared but stretched instead. As a reference, measurement data from Evans [41] are plotted (orange stars).

ues for μ. At a moderate formaline concentration of 18.4 wt.% μ increases to $\mu_{(c_{for}^1)}$=7.6 µN/m and for 36.8 wt.% formaline concentration a significantly higher value of $\mu_{(c_{for}^2)}$34 µN/m is found. In contrast, μ is more sensitive to treatments with diamide yielding in $\mu_{(c_{dia}^1)}$=125 µN/m and $\mu_{(c_{dia}^2)}$=185 µN/m. RBCs suffering from β-Thalassemia show a weak increase of the shearing modulus μ_β=8.4 µN/m compared to healthy RBCs ($\mu_{healthy}$=6.8 µN/m).

In all experiments a characteristic threshold of the aspiration length could be observed. There, the aspiration length strongly increased with a small change in pressure. In this regime ($D_P/R_P > 4$) the slope of the measurement cannot be used for the identification of the shear modulus. This coincided with the approach of the upper limit of validity of equation 4.1. A new parameter B was used to identify the mechanical parameters in this region. B was measured in the same fashion as μ by fitting a linear regression to the measurement data in the regime $D_P/R_P > 4$. It could be correlated to an extension of the membrane without a shearing portion.

Healthy RBCs were found to have B of $B_{healthy}$ =31±1.7 µN/m. Surprisingly, high concentration modifications showed a decreased value of $B_{(c_{for}^2)}$ =28±2.0 µN/m for formaline modification and $B_{(c_{dia}^2)}$ =267±21 µN/m for diamide modification compared to the low concentrations of $B_{(c_{for}^1)}$ =32±2.6 µN/m for formaline modification and $B_{(c_{dia}^1)}$ =340±22 µN/m for diamide modification.

β-Thalassemia does not affect B. The value is the same as for healthy RBCs.

The parameters μ and B are discussed in the following section.

4.1.2 Discussion of the Shearing Behavior of the Membrane Modifications

In the set of experiments, healthy, diamide and formaldehyde modified RBCs were characterized by MPA technique. The experiments for healthy RBC find $\mu_{healthy} = 6.8$ µN/m. Compared to measurements performed by Evans 1989 [41] the measurement showed identical cell behavior when aspirated in the capillary and similar value of the modulus. On the one hand this is a convincing proof of the measured value and on the other hand of the measurement itself.

In contrast, the value for $B_{healthy} = 31$ µN/m, which is obtained for high suction pressures ($4 < D_P/R_P < 7$) cannot be directly identified with the area expansion modulus measured in the literature because the described method de-

termines the sum of area expansion components together with shearing components. In the literature, K_A is found to be in the range of K_A=300-500 mN/m [39, 61, 80], but other studies performing optical fluctuation measurements find K_A=1 μN/m to K_A=30 μN/m [46, 29, 21]. It is a more reasonable value since K_A for pure spectrin networks has been found to be of that order [85].

Cell Type	μ (N/m)	B (μN/m)
Healthy Human RBCs	$6.8 \pm 1.4 \times 10^{-6}$	31 ± 1.7
Diamide Modified RBCs (0.34 wt%)	$1.3 \pm 2.7 \times 10^{-4}$	340 ± 22
Diamide Modified RBCs (0.68 wt%)	$1.9 \pm 2.7 \times 10^{-4}$	267 ± 21
Formaline Modified RBCs (18.4 wt%)	$7.6 \pm 2.4 \times 10^{-6}$	32 ± 2.6
Formaline Modified RBCs (36.8 wt%)	$3.4 \pm 0.2 \times 10^{-5}$	28 ± 2.0
Human β-Thalassemia RBCs	$8.4 \pm 2.2 \times 10^{-6}$	31 ± 2.1

Table 4.1: Summary of the measured constants: Shearing modulus μ and B. In contrast to the β-Thalassemia the chemical modifications show increased values.

In the following the chemically incubated RBCs are compared to healthy RBCs. Formaline introduces CH_2-groups between aminoacids inside the cytoskeleton but is also known to connect hemoglobin to the membrane. While for low formaline modifications (c_{for}^1) the shear modulus μ is slightly increased, higher incubation concentrations (c_{for}^2) increase μ about a factor of 10. This can be explained by taking the membrane architecture into account. Formaline cross-links spectrin dimers. The unfolding during cell shear is thereby disabled, but compression and expansion of the spectrin dimers are still possible.

In contrast, the diamide alteration increases only the cross-links inside the cysteine of the spectrin-actin [4, 174, 156]. This very specific modification increases shear modulus and area expansion modulus by a factor of 100. Diamide modification is known to cross-link the cysteins inside the spectrin dimers more strongly [115]. Finally, unfolding of spectrin is impeded so that shearing as well as compression are affected. These assumptions are strongly supported by the fact that the area expansion modulus correlated to parameter B is increased by a factor of 10. This indicates a stiffened spectrin polymer.

Erythrocytes suffering from β-Thalassemia show nearly no change in μ or B. Here α- and β-chains of hemoglobin are altered. This does not affect the membrane of a RBC. It only changes the inner viscosity of the cell weakly. Thus the response of these cells in the micropipette is similar to the one measured for healthy RBCs.

4.2 Indentation Type Atomic Force Microscopy

The stress-strain relation can also be gained by indenting a very stiff tip into the RBC (stiff in comparison to the cell). The measurement is performed using an AFM in the force spectroscopy mode. In the IT-AFM technique, the indentation force is measured in dependency of the penetration depth. Since the spring constant of the cantilever is calibrated, the measurements allow the determination of a bending correlated mechanical parameter.

The bending modulus of RBCs was measured by several groups and varies between κ=0.13$\cdot$10^{-19} J to κ=3$\cdot$10^{-19} J [40, 68, 124, 173, 65, 141, 159, 175, 110, 54] depending on the technique and preparation method. As outlined in the previous section, different preparation techniques, measurement techniques and blood donors influence the measured bending modulus. Consequently, using the same preparation protocol for the identification of the bending modulus of healthy and modified RBCs as in the flow measurements is necessary.

4.2.1 Indenting RBCs

Freshly prepared RBCs were pipetted in a glass petri dish that was mounted onto the stage on an inverted microscope. The petri dish contained PBS and BSA (concentration = 1 mg/ml). The AFM unit was located above the petri dish. The main parts of the instrument consists of a laser and a detector that measures the reflection light or the cantilever deflection respectively. Fast movements of the AFM-tip were performed with a stepper motor and the precise movement was controlled by piezo elements. Before cells could be measured by indenting the cantilever tip into the sample, the spring constant and the sensitivity of the measuring system had to be calibrated. The first calibration step was necessary because every time the cantilever was mounted to the device or after long measurements the calibration values could have changed. The calibration process contains two steps: First, the laser deflection which was measured in voltages by the laser detector was converted into a real distance x by calibrating the sensitivity. Second, the spring constant of the system was calibrated to calculate the force with the help of the previously calibrated distance x using Hooke's law $F = kx$. The detailed calibration process is explained in the methods and materials (see section 3.3.3). Before a cell was measured the calibration process was repeated, because the constants had possibly changed during several hours of measurement: for example the

temperature changed or proteins deposited on the cantilever.

Once the system was calibrated, a RBC that was not in contact with other cells was selected using the inverted microscope. The cell was photographed to compare the shape before and after the experiment. The cantilever was then closely positioned to the upper left side of the cell. A force scanning grid of 10 x 10 μm with subunits of 1 μm was selected in the JPK software. This is the selected square area where JPK automatization measured the located cell. After defining the scanning area, the initial height was defined to be 4 μm so that the tip always started to scan some μm above the cell. The scanning velocity was set to 4 μm/s and the maximum applied force on the cell was limited to 3.5 pN. The AFM then measured 200 force curves (extend and retract) automatically. Finally, the experiment was repeated on a decreased scanning grid of 1 μm x 1 μm with subunits of 10 nm at the rim of the cell. The 10,000 single curves obtained in that experiment give a good statistic for the measured elastic behavior of cells.

Figure 4.3 (top) shows a typical extend and retract raw data curve. The bottom graph in figure 4.3 shows data where the contribution of the tip and the sample is separated from each other in order to obtain data from the cell only. This process is described in the methods and material part in detail (see section 3.3.3). The curve shows that no force is needed to lower the tip until it approaches the surface of the cell. As the tip indents into the cell the force increases. Single curves were then fitted using the Hertz model to determine the elastic constant E.

$$F = \frac{E}{1 - \nu^2} \frac{\tan\alpha}{\sqrt{2}} \sigma^2 \qquad (4.2)$$

In the equation, F is the measured force, σ is the indentation depth, α is the face angle of the tip and ν is the Poisson's ratio which is ν=0.5. In the fitting model the modulus is very dependent on the indentation depth. Thus, for the analysis of the 10,000 single AFM curves only data points for indentations smaller than σ=100 nm are used.

The measurement and analysis described above was performed on healthy, diamide and formaline modified human RBCs. The fitting procedure revealed a higher Young's modulus for healthy human RBCs than described in other
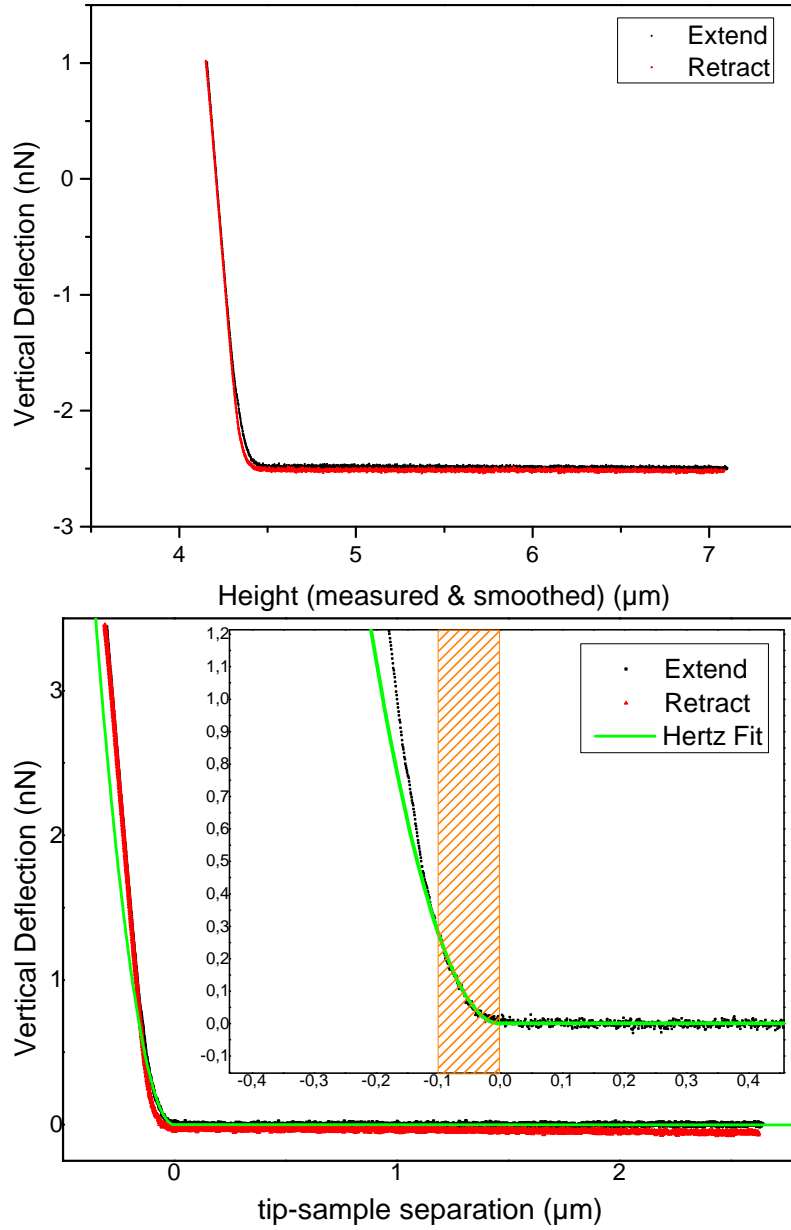
Figure 4.3: Typical indentation data of a single AFM measurement performed on a healthy human RBC. The upper image shows raw data from the AFM. The lower image shows data after having the influence of the tip separated from the sample. This is done by calibrating the system by performing a force measurement without the sample. The black lines correspond to the extend and the red lines correspond to the retract part of the indentation process. To determine the elastic constant E a Hertz-Fit is used (green line). The Hertz-Fit was only fitted for indentation data up to $100\,\mathrm{nm}$ (orange area). The magnification in the lower image shows the fit deviation clearly.
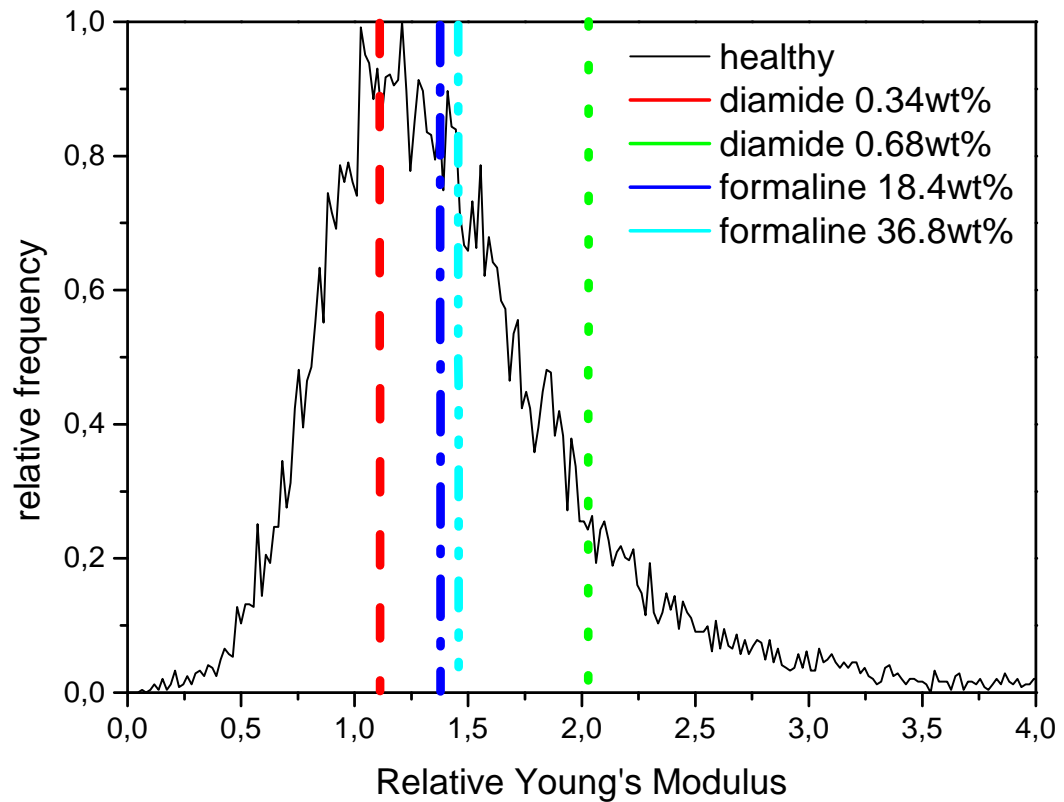
Figure 4.4: Relative frequency in dependency of the elastic constant. Healthy human RBCs are defined as the standard at 1. The maximum probability for the chemical modifications are shown as straight lines relative to healthy RBCs. Low diamide modification increases the bending by about 11% and high modification by about 107%. Low formaline modification shows a decreased bending parameter of 37% and a high modification of 45%.

works (see discussion in the next chapter). Because of that the elasticities of the chemical modifications are given relatively to the value of healthy RBCs. The selective modification of the RBC membrane properties by applying an oxidizing and a reducing agent, formaldehyde and diamide respectively, yielded an increased elastic constant E. The low diamide modification increased the constant by about 11 % and low formaline modification by about 37 %. High diamide modification increased the bending rigidity by about 107 % and high formaline modification by about 45 %. Using the model of a two-dimensional plate ($\kappa = Eh^3/9$) the bending modulus for healthy RBCs and chemically modified RBCs is determined. Here, E is the elastic constant and h is the thickness of the membrane. Using h=34 nm [86, 56, 89] and the measured Young's Modulus E=110 kPa for healthy RBCs, the bending modulus is found to be κ=4.80·10^{-19} J. This value is in good agreement to the bending modulus found by other groups (see discussion in the next section). The bending modulus was established for the chemical modifications in the same way. The low concentration of formaline and diamide yield a bending rigidity of κ=6.59 · 10^{-19} J and κ=5.33 · 10^{-19} J respectively. Modifying the cells with higher concentrations of formaline and diamide further increased bending rigidities to κ=6.99 · 10^{-19} J and κ=9.74 · 10^{-19} J respectively. All measurements are summarized in figure 4.4.

4.2.2 Discussion of the Indentation Experiment

In this thesis the standard Hertz-model is used. The model is only valid for indentation depths of 100 nm where it establishes the viscoelastic properties of RBCs. The measured value for the Young's modulus of healthy RBCs is $\approx$ 110kPa which is more than 5 times higher compared to other IT-AFM studies [84, 36]. Recently, Dulinska et al. [36] measured the Young´s modulus by IT-AFM using the Hertz-model. Their Young´s modulus value was 10 to 100 times larger than the ones obtained for other cells [84, 36]. However, they immobilized the cells using 0.5 % concentration of glutardialdehyde for 1 min.

The relative changes of the bending modulus can be used to extrapolate the bending moduli of the chemically modified cells. This estimation assumes a linear increase of the bending modulus in dependency of the chemical modification (see κ in table4.2).

IT-AFM measurement shows that the bending modulus of the RBCs is af-

Cell Type	Bending Increase (%)	κ (J)
Healthy RBCs	0	4.80×10^{-19}
Diamide RBCs (0.34 wt%)	11	5.30×10^{-19}
Diamide RBCs (0.68 wt%)	107	9.74×10^{-19}
Formaline RBCs (18.4 wt%)	37	6.59×10^{-19}
Formaline RBCs (36.8 wt%)	45	6.99×10^{-19}

Table 4.2: Summary of the IT-AFM measurement. The chemical modifications lower the bending modulus of the membrane and increase the bending modulus κ of the whole cell.

fected weakly by chemically modifications compared to the shearing behavior (see section 4.1) measured by MPA. Some studies [20, 166, 36] report that the measured modulus using IT-AFM reflects the properties of the cytoskeleton only. However, the AFM tip monitors the response from the cytoskeleton as well as from the plasma membrane. It is difficult to separate the both contributions, because both influence each other as pointed out in the beginning of the thesis (see chapter 2.1.1). Both can influence the overall stiffness of erythrocytes. [36] However, the increase of the bending modulus of the chemical modifications can be explained by the cytoskeleton architecture. Formaline modification increases the bending modulus in a moderate way. Both concentrations strengthen the bending modulus of the cells by a similar amount (increase of 37 % and 45 %). Formaline cross-links the spectrin polymers. As a consequence, the skeletal network decreases its mesh size. Indenting a small tip into a denser network should not affect the indentation process so much. The moduli are thus increased slightly. In contrast, modifying the cells with diamide introduces cross-links inside the cysteins of the spectrin. Therefore, the unfolding of the spectrin is hindered, thus indenting the tip into a network of higher spring constants requires more force. A low diamide modification increased the modulus only by about 11 % but double the diamide concentration increased the modulus by 107 %.

4.3 Deformation of RBCs in Shear Flow

So far, mechanical properties of RBCs have been measured statically by either indenting a tip into the cell or aspirating the entire cell. These two methods are invasive, as the cell is in contact with a tip or glass pipette that may affect the cell properties by adhesion. Moreover, these methods are problem-

atic for identifying the mechanics of the entire cell itself. Measuring the cell deformation contactlessly mitigates these disadvantages.

Contact-free and non-invasive deformation of lipid vesicles [74, 30, 28, 75, 79, 104, 158] and RBCs in hydrodynamic flow fields in microchannels have been studied in experiments [16, 50, 153, 150, 149, 152, 151, 105] and simulations [75, 146, 104, 129, 128, 127].

In the following experiment, the deformation of healthy and chemically modified RBCs was measured depending on their mean velocity in a 10 x 10 µm PDMS microchannel. These channel dimensions correspond to tiny capillaries in the human body for example in organs or the capillaries of the testicles. The deformation versus average velocity is supposed to identify a stress-strain correlation because the shear force acting on the cell increases with rising flow velocity. Note that in this section the cell shape changes are initially ignored and will be discussed in the following sections in detail.

4.3.1 Deformation Experiment in a 10 x 10 µm PDMS Microchannel

To analyze RBC deformation in hydrodynamic shear flow, the cells were introduced in a straight PDMS molded microchannel. A hydrostatic pressure difference between the in- and outlet was applied to control the RBC velocity. Then the RBCs were observed with a high speed camera (Photron) at physiological velocities up to $v_{RBC}=3500\,\mu m/s$.

In figure 4.5, the strain is quantified by the Taylor deformation $D = (b - a)/(b + a)$, where a and b is the length and width of a bounding box around the cell as depicted in the inset of figure 4.5. In the plot of figure 4.5 D increases with increasing flow velocity and reaches a plateau at higher velocities for all samples. For healthy RBCs, a maximum deformation of $D \approx 20\,\%$ is reached at velocities of $v_{RBC} \approx 1000\,\mu m/s$. This sigmoid-like behavior has been simulated by Secomb [129] in slightly smaller channels. The simulated deformations in the channels having 8 µm width were in good agreement to the ones we observed in our 10 µm channel (see inset figure 4.5). Generally, the chemically modified RBCs showed a lower deformability. Formaline treated RBCs saturated at higher velocities of $v_{RBC} \approx 1700\,\mu m/s$ and showed smaller Taylor deformation. Diamide modifications saturated at higher velocities of around $v_{RBC}=2000\,\mu m/s$ and showed lower Taylor deformations. The cells modified
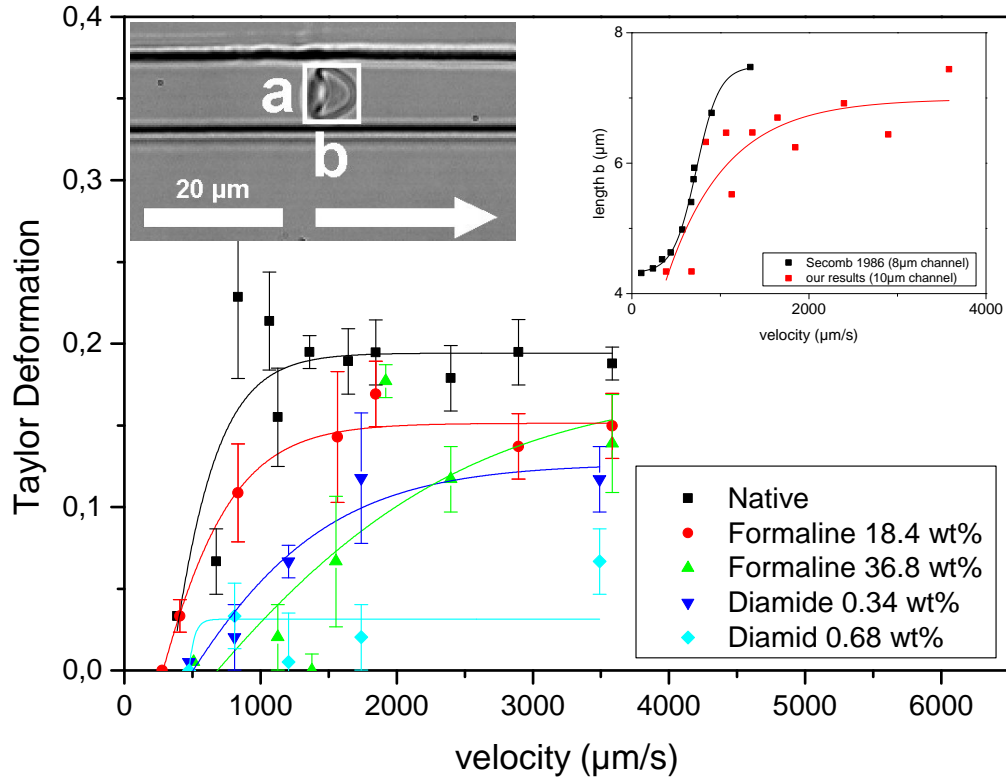
Figure 4.5: Taylor deformation ((b-a)/(b+a)) versus cell velocity of healthy and chemically modified RBCs in the microchannel. Each data point represents the average Taylor deformation of ≈ 20 RBC. With increasing flow velocity the Taylor deformation increases. The solid lines are guides to the eye and show a sigmoid-like behavior. The deformations for native RBCs reach levels (D=0.20) well above those of chemically modified RBCs (D=0.03-0.15). The micrograph in the upper left inset illustrates a RBC in the microchannel with its corresponding bounding box. The micrograph in the upper right inset is a comparison of our data for the cell length b with theoretical calculations of Secomb [129]. Both experimental data and theoretical predictions show similar saturation behavior of cell length dependent on cell velocity. Note that the maximum value for the cell length in our experiment is smaller than compared to the theoretical predictions because smaller capillaries were used here.

with the highest diamide concentration (c=0.68 wt%) were only deformed at very high velocities (more than v_{RBC}=4000 μm/s).

4.3.2 The Taylor Deformation as a Parameter for Altered Shape of RBC

Recent advances using microfluidic techniques enabled high-throughput characterization of cells. However, the stress-strain relation is quite complex and it is challenging to relate the deformation to the mechanical parameters. To complement the MPA and AFM measurements, RBCs were deformed hydrodynamically in PDMS microchannels. Exposed to the parabolic shear flow in the channels, the deformation of chemically modified cells is lowered and a higher shear stress is needed to reach the same deformation levels as in healthy RBCs. In the case of native RBCs, a Taylor deformation increase up to 20 % was observed. This is in good agreement with theoretically [127] and experimentally [153] determined deformations at the same shear levels. The deformation behavior follows a sigmoidal progression with increasing shear stress similarly to the observations by Tomaioullo et al. [153]. Abkarian et al. [4] used round shaped channels and higher viscosities compared to our measurements. They observed a similar sigmoid behavior in deformation as well. In the experiments the chemical incubation shifted deformation to higher shear stress and lowered the maximum deformation. Several studies report an increase in stiffness of RBCs by either using glutardialdehyde [174, 150, 102, 50, 156] or diamide [115, 10, 143, 50, 173] at various concentrations and for different preparation techniques. In a microfluidic study [50] and a study using filtration techniques [106, 148] no deformation of diamide modified RBC was observed. This discrepancy may be explained by the significantly 10 times lower diamide concentration they used. Other MPA and cone-plate viscometer studies report a lower Taylor deformation ($D \approx 0.2$) as well which supports the measured results [49, 71]. More consistently, the effect of formaline modification has been found to influence the Taylor deformation (regarding $D \approx 0.2$) in the same fashion for glass capillary or PDMS microchannel experiments[150, 102, 174, 50, 156].

4.4 Morphology of Shapes in Bounded Flow

The last section showed that it is possible to characterize the mechanical resistivity of RBCs upon their deformation in a parabolic flow profile. The Taylor deformation parameter D is not a completely satisfying parameter for characterizing the mechanics of RBCs, because the deformation parameter does not consider the shape of the RBCs. As already remarked RBCs are known to change their shape in parabolic flow profiles with increasing flow velocity (see also section 2.3.5). Beside the discocytic rest shape, there are two other meta stable shapes - slipper and parachute shapes. In the last section the deformation parameter D increased for healthy RBCs and velocities of around $v_{RBC}{=}1000\,\mu\text{m/s}$ dramatically. For higher velocities D was lowered again. Obviously the slipper shape (expected to be in the mentioned regime) yields higher deformation parameters than the parachute shape does. This section thus investigates the shape morphology in detail.

High-speed imaging microscopy and novel channel design techniques allow the observation of RBCs under quasi physiological conditions. Mimicking the physiological environment of the cell allows new insights in cell deformation. While travelling through the narrow capillaries of the cardiovascular system the cell experiences a permanently acting shear stress. This shear stress mainly depends on the capillary diameter $2R_{cap}$. In addition, the shear stress will also deform RBCs or change the cell shape.

In 1969 Skalak and Branemark [133] published microscopy images of human RBCs flowing in a $7\,\mu\text{m}$ thin capillary in vivo. On these images the RBCs are not in their discoytic rest shape but in slipper and parachute shapes. In the literature there are further investigations concerning the shape of RBCs exposed to shear stress. In simple linear shear flow [4] or in capillary flow [1] RBCs were studied experimentally. The axisymmetric parachute shape is a well accepted and studied shape of RBCs, whereas the experimental parameter necessary for slipper shape formation is not clear. Some publications [133, 4] claim that the shape is only a transient shape and not stable. In other publications, the cell properties of chemically stiffened RBCs were investigated to simulate blood diseases. Diseased RBCs of patients suffering from diabetes mellitus often have increased mechanical cell stiffness. However, in the literature, the cells are observed with respect to various chemicals of different concentrations and different fluid viscosities compared to the used ones in this thesis. Thus,

the main focus of this section is the characterization of the three shapes in detail. In this thesis, the slipper is found to be a stable shape in addition to the discocyte and parachute shape. For each chemical modification a typical representative of a discocyte, slipper and parachute is shown at its maximum shape probability (more than 50%) in a 10 x 10 μm PDMS microchannel. The shapes are characterized and compared by their size and curvature.

In the following experiment, the stable shapes (discocyte, slipper and parachute) of healthy, chemically modified and diseased RBCs are investigated in detail to investigate whether the shape itself is altered among the various modifications.
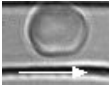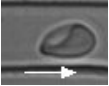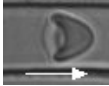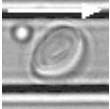
4.4.1 Experiments
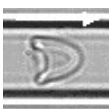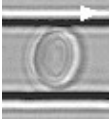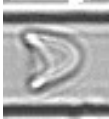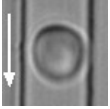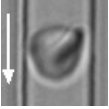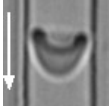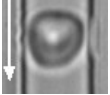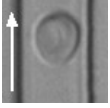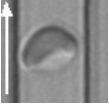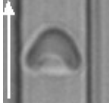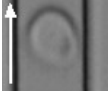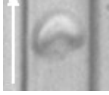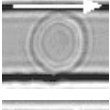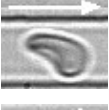
RBCs were observed while flowing in a small square-shaped cross section microchannel, having a width and height of around 10 μm. The images were taken 1 cm after the inlet. This ensured that the cells had enough time to relax into a stable shape and a constant flow velocity.

Table 4.3 shows the three stable shape configurations (discocyte, slipper and parachute) for healthy cells, formaline modified cells, diamide modified cells, RBCs suffering from Spherocytosis and β-Thalassemia. Furthermore, the shape configuration of RBCs from alpaca is depicted.

The discocyte of healthy human RBCs at very low flow rates (less than $v = 500\,\mu$m/s) was very similar to the shape at rest. The biconcave discoid shape was slightly elongated in flow direction. The curvature of the front (C_f^{disco}) and rear (C_r^{disco}) has a value of around $C_f^{disco}=C_r^{disco}=0.265\,\mu$m^{-1}. The curvature of the cell shape (front or rear) is measured as the inverse radius of a fitted circle to the two dimensional projected shape.

When the cells were modified with formaline, the discocyte shape was the same as for healthy cells, in general. They had the same cell dimensions and were also elongated in flow direction. The center of the cell seemed to be thinner for increasing formaline concentration. For low formaline modified RBCs (c=18.4 wt%) the front and rear curvature was around $C_f^{disco}=0.240\,\mu$m^{-1} and $C_r^{disco}=$-0.248 μm^{-1}, respectively. High formaline modification (c=36.8 wt%) showed a further increase of the curvature having a front curvature of $C_f^{disco}=$ 0.212 μm^{-1} and a rear curvature of $C_r^{disco}=$-0.140 μm^{-1}. The modification of the RBCs with diamide led to an even thinner center of the cell. The dimen-

sions were comparable to healthy ones and the discocyte was also elongated in flow direction. Low concentrations of diamide (c=0.34 wt%) showed a front curvature of C_f^{disco}=0.240 μm^{-1} and a rear curvature of C_r^{disco}=-0.308 μm^{-1}. The high diamide concentration (c=0.68 wt%) showed a curvature of C_f^{disco}= 0.371 μm^{-1} at the front and C_r^{disco}=-0.239 μm^{-1} at the end. Introducing additional cholesterol to the membrane caused a front curvature of C_f^{disco}=0.218 and a rear curvature of C_r^{disco}=-0.232 μm^{-1}. Minor cholesterol concentration in the plasma membrane resulted in a front curvature of C_f^{disco}=0.247 and a rear curvature of C_r^{disco}=-0.249 μm^{-1}.

	Discocyte	Slipper	Parachute

Healthy

259 mOsm

405 mOsm

Formaline 18.4 wt%

Formaline 36.8 wt%

Diamide 0.34 wt%

Diamide 0.68 wt%

Cholesterol Enriched wt%

Cholesterol Depleted wt%
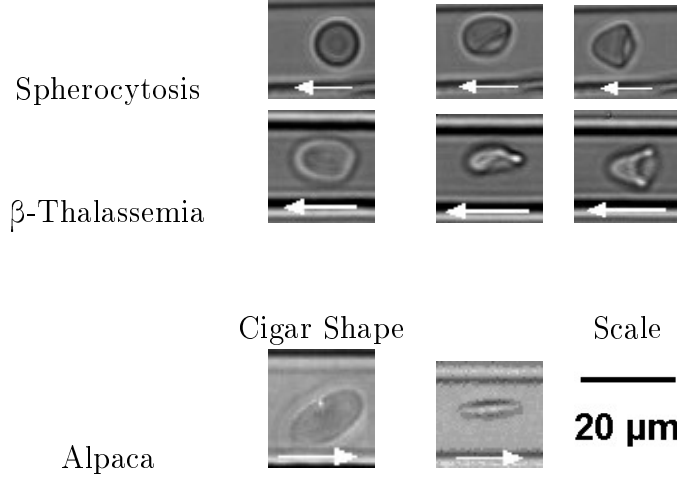
Table 4.3: Shape configurations of healthy, chemically modified and diseased human RBCs. Additionally, RBCs from alpaca are depicted. The micrographs show the three typical and stable shapes (discocyte: first row, slipper: second row and parachute: third row) the cells adopt while flowing (direction indicated by the arrow) in a narrow capillary of around 10 μm. The images of the shapes were taken at the velocity of the corresponding maximum shape probability. In the case of alpaca RBCs there is only the rest shape configuration, even at very high shear stress. Different chemical modifications affect the cell size additionally.

For RBCs suspended in a hypotonic buffer of c_{osm}=405 mOsm a front curvature of C_f^{disco}=0.245 μm^{-1} and a rear curvature of C_r^{disco}=-0.253 μm^{-1} was measured. For a hypertonic buffer of c_{osm}=259 mOsm, the curvatures of front and rear were C_f^{disco}=0.230 μm^{-1} and C_r^{disco}=-0.235 μm^{-1}, respectively. The situation was different for RBCs suffering from Spherocytosis. The discocyte was smaller (see appendix A.7) and the shape was spherically with a thick rim. The front and the rear curvature value of the discocyte was around C_f^{disco}=C_r^{disco}=±0.371 μm^{-1}, respectively. RBCs suffering from β-Thalassemia did not show a size decrease. Their front curvature was C_f^{disco}=0.412 μm^{-1} and their rear curvature was C_r^{disco}=-0.353 μm^{-1}.

Under increasing shear stress the biconcave discoid red cells deformed into a slipper-like shape. As the name suggests, the configuration of the cell adopted a slipper. The sole of the slipper was always close to the wall and the cell was flowing off the center. For the shape characterization of the asymmetric slipper shape the front curvature $C_f^{slipper}$ of the cell is measured only. This is mainly because the rear part of the cell is not spherical and shows an excrescence. In addition, the ratio of excrescence to the cell length

($R^{slipper}$) is measured. For healthy slipper it was measured to be $R{=}0.571$ with a curvature of $C_f^{slipper}{=}0.436\,\mu\mathrm{m}^{-1}$. Modifying healthy human RBCs with formaline led to a modified slipper shape. In general, the slipper was not as pronounced and the excrescence is thicker. Low formaline modification (c=18.4 wt%) had a longer protuberance. The ratio of the excrescence was increased to $R^{slipper}{=}0.632$. Compared to healthy RBCs, the front curvature was decreased to $C_f^{slipper}{=}0.322\,\mu\mathrm{m}^{-1}$. A higher concentration of formaline incubation (c=36.8 wt%) increased the $R^{slipper}$ further to a ratio of $R^{slipper}{=}0.725$. The curvature of the front decreased to a value of $C_f^{slipper}{=}0.265\,\mu\mathrm{m}^{-1}$ as well. When the cells were modified with diamide, the situation is different. Depending on the incubated amount of diamide, the shape configuration was altered. Low diamide incubation (c=0.34 wt%) showed a slightly compressed healthy slipper having $R^{slipper}{=}0.412$ and a front curvature of $C_f^{slipper}{=}0.285\,\mu\mathrm{m}^{-1}$. In contrast, high diamide modification (c=0.68 wt%) showed a similar slipper compared to formaline modification with $R{=}0.636$ and a front curvature of $C_f^{slipper}{=}0.265\,\mu\mathrm{m}^{-1}$. By increasing the cholesterol content in the plasma membrane, the front was curved by $C_f^{slipper}{=}0.412\,\mu\mathrm{m}^{-1}$ and the length ratio is $R^{slipper}{=}0.441$. In contrast, cholesterol depletion showed a front curvature of $C_f^{slipper}{=}0.529\,\mu\mathrm{m}^{-1}$ and a length ratio of $R^{slipper}{=}0.740$. Decreasing the tonicity of the buffer to $c_{osm}{=}205\,\mathrm{mOsm}$ showed a front curvature of $C_f^{slipper}{=}0.402\,\mu\mathrm{m}^{-1}$ and a length ratio of $R^{slipper}{=}0.441$, whereas an increased tonicity showed a front curvature of $C_f^{slipper}{=}0.623\,\mu\mathrm{m}^{-1}$ and a length ratio of $R^{slipper}{=}0.689$. Spherocytosis-RBCs again had smaller dimensions and looked like a compressed healthy slipper with $R^{slipper}{=}0.741$ and a front curvature of $C_f^{slipper}{=}0.390\,\mu\mathrm{m}^{-1}$. In the case of the disease β-Thalassemia the front curvature increased to about $C_f^{slipper}{=}0.741\,\mu\mathrm{m}^{-1}$ and the excrescence length was half the cell length ($R^{slipper}{=}0.500$).

Another shape that occurred at high shear stress was the parachute shape. Again, as its name suggests, the shape looked in a two dimensional projection like a parachute having a convex front with two concave protuberances in the back. The parachute was axisymmetric and always flew at the center of a capillary. As for the slipper shape the rear of the cell showed two excrescences. Their length compared to the cell length was measured as R^{para}. Again, the front curvature C_f^{para} was measured. Healthy human RBCs showed a front curvature of $C_f^{para}{=}0.494\,\mu\mathrm{m}^{-1}$ and a length ratio of $R^{para}{=}0.375$. As in the case of the slipper configuration, formaline modifi-

cation decreased the curvature of the front. The curvature of low formaline treatment was C_f^{para}=0.353 μm^{-1} and C_f^{para}=0.322 μm^{-1} for the higher treatment. The protuberance-length ratio was R^{para}=0.486 in the case of moderate formaline incubation and 0.512 for higher formaline modification. The two protuberances of the parachute were not as pronounced in the case of high formaline incubation as compared to healthy ones. In the case of diamide modified RBCs, the curvature was also decreased to values of C_f^{para}=0.371 μm^{-1} and for twice the incubation concentration to C_f^{para}=0.322 μm^{-1}. The ratio was found to be R^{para}=0.333 for the low and R^{para}=0.533 for the high diamide concentration. Modifying the plasma membrane with cholesterol affected the parachute as follows. Cholesterol enrichment showed a front curvature of C_f^{para}=0.570 μm^{-1} as well as cholesterol depletion C_f^{para}=0.570 μm^{-1}. The length ratios remained nearly the same with R^{para}=0.600 (enrichment) and R^{para}=0.679 (depletion). Suspended in a hypotonic solution the front of the parachute was curved by C_f^{para}=0.482 μm^{-1} and the length ratio was 0.613. In contrast, hypertonic buffers affected the parachute in a way that the front curvature increased to C_f^{para}=0.603 μm^{-1} and the length ratio was R^{para}=0.683. Parachutes suffering from Spherocytosis were accompanied by a front curvature of C_f^{para}=0.618 μm^{-1} and R^{para}=0.667. The curvature in the case of β-Thalassemia was increased to about C_f^{para}=0.927 μm^{-1} at the same length ratio of R^{para}=0.692.

As already discussed in the theoretical part (see section 2.1.4), RBCs from alpaca are characterized having an altered shape in the class of mammals. Adopted to shear stress in microcapillaries, the cells also show altered behavior. As described, the discoid biconcave shapes of humans and other mammals show two other stable shapes when they flow in parabolic flow profiles. In the experiments, no shape deformation of RBCs from alpaca has been observed when they were flowing in microcapillaries. As table 4.3 indicates the shape configurations of the alpaca RBCs were always a flattened ellipsoid.

4.4.2 Shape Morphology in Dependency on Membrane Configuration

The transition of RBCs from a discocytic rest shape into a parachute shape is quite known and discussed in the literature [1, 133, 54]. However, the situation for the slipper shape is still undefined. For example, Abkarian [4] observes

slipper only at very high shear stress. In contrast, Tomaiuolo et al. [153] also observes an asymmetric slipper-like shape before the transition into parachutes. However, theoretical studies claim a slipper shape [104, 146]. Recently, Tahiri et al. [146] simulated a phase diagram with various RBC shapes. Beside the typical discocyte, slipper and parachute shapes defined in the experiments, they additionally found a centered snaking, off-centered snaking and a peanut shape. But the flow environments where these theoretically calculated shapes occurred were very narrow. In addition, it is hard to distinguish these varied slipper-like shapes from the observed slipper shape in real experiments (compare images in table 4.3).

In the experiments, the measured curvatures C and length ratios R were obtained in a flow regime where the shape showed its highest probability (see section 4.5). Admittedly, the length ratios vary critically on the shear stress. In contrast, front curvatures C_f of the shapes were found to be very stable over the complete shape flow regime. Thus in figure 4.6 the front curvature for all RBC modifications and diseases is used.

Interestingly enough, the discocytic rest shape showed comparable front curvatures over all modifications. With the exception of high diamide modification and the two blood diseases, the discocyte showed a curvature of C_f^{disco} $\approx 0.25\,1/\mu m$. Diamide and formaline modifications, two chemicals that change the mechanical properties directly, showed a very low curvature for their slipper and parachute shape. Even the rest shape showed a lowered curvature. Incubation of cells with these chemicals increases the number of cross-links inside the cytoskeleton. Thus the bending and stretching of the membrane is hindered and smaller curvatures of the membrane is measured. In total, the curvature was lowered by about 50 % for both chemicals. An indirect modification of RBCs by adding or removing cholesterol from the plasma membrane resulted in a higher bending of the cell membrane. Both cholesterol enrichment and depletion showed an increased curvature ratio between discocyte and parachute, but showed variations in the slipper shape. In the case of cholesterol depletion, the slipper showed a higher curvature than the cholesterol enrichment. The stronger curvatures of cholesterol enriched RBCs could be explained by the increase of plasma membrane area by the additional amount of cholesterol lipid. From that point of view, cholesterol depletion should decrease the curvatures of all three shapes. Obviously, cholesterol modification did not influence the curvatures of the complete membrane. Increasing the inner pressure of the
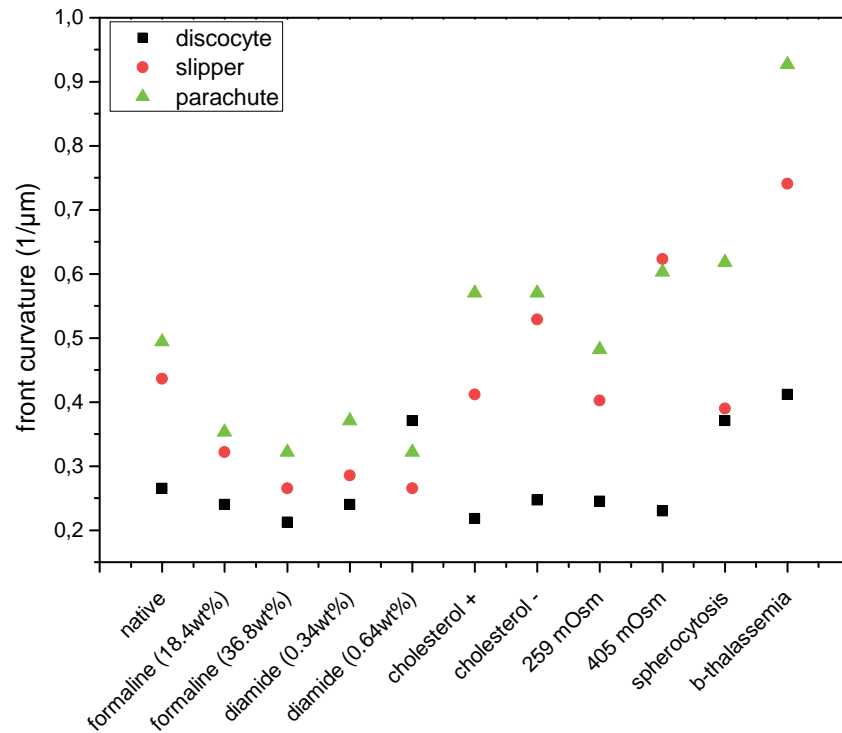
Figure 4.6: Front curvatures C_f of discocyte (black), slipper (red) and parachute (green) shapes for all RBC modifications and diseases. In general, the curvatures of the discocyte are lower than the slipper and even lower than the ones of the parachute shape. Especially the modifications in which the membrane is under tension show a higher difference in the curvature changes among the shapes.

RBCs did not change the curvatures of the shapes. Since c_{osm}=259 mOsm is very close to the native osmolarity of blood serum ($c_{osm} \approx$290 mOsm) it was only a weak change. In contrast, decreasing the inner pressure by increasing the buffer osmolarity to c_{osm}=405 mOsm yielded high curvatures. This could be explained by the compressing tension inside the membrane due to the lowered inner water pressure. However, the situation for real blood diseases is completely different. Spherocytosis RBCs showed an increased curvature for all three shapes. This could be explained by the smaller cell size (see appendix A.7) and the lowered volume to surface ratio. The situation was even more dramatic for β-Thalassemia because the curvatures were even higher. The cells were very flexible due to the alterations in the membrane by hemoglobin bindings.

Recently, Noguchi and Gompper [104] simulated the front curvature of elastic and fluid parachute shaped vesicles in dependency on the bending modulus. The simulation predicted that with increasing bending modulus κ the front ends became more smoothly rounded [104]. From that point of view, diamide and formaline modification showed an increased bending modulus κ, whereas cholesterol modification and osmolarity changes decreased the bending modulus weakly. The two diseases Spherocytosis and β-Thalassemia, showed a stronger decrease in bending modulus upon these simulations.

Another interesting fact is that both the slipper and the parachute showed very smoothed excrescence edges (see table 4.3) compared to the micrographs of Abkarian et al. [1]. This is possibly due to the 20 times higher external viscosity they used in the flow experiments.

Alpaca RBCs showed their characteristic morphology in the form of a flattened elliptical shape but in the experiments no shape change could be found. The cells remained in their rest shape even at shear stresses of τ=320 N/m^2. The non-deformability upon acting shear stress is also reported in the literature [108].

4.5 Shape Distribution of Flow Induced Shapes in a Straight PDMS Microchannel

The last experiments showed that RBCs deform upon increasing shear stress in PDMS microchannels. Measuring their Taylor deformation can be used to

identify altered mechanical properties. However, the RBCs change their morphology with increasing external shear force. Furthermore, the single characterization of the RBC shape also shows variations among altered mechanical properties of RBC. Now, after the deformation and the shape parameters have been characterized in detail this section is intended to identify the exact flow conditions under which certain shapes occur. The cells are observed in a PDMS microchannel having a quadratic cross-section. Furthermore, a huge number of cells is observed to improve statistics. In addition, this experiment is suitable for testing whether the slipper is a totally stable shape in between the discocyte and parachute.

4.5.1   Measurement of Shape Distributions in a PDMS Microchannel

The microchannel, with a square cross section of 10x10 µm, was mounted onto a motorized stage of the inverted microscope. RBCs were then pipetted to the inlet of the PDMS microchannel and the pressure in the channel was decreased by lowering a height-adjustable reservoir of 30 cm. The reservoir was connected to the outlet of the channel and allowed precise adjustments of the RBC velocity in the range of v_{RBC}=0 µm/s and v_{RBC}=4000 µm/s. After 30 s, RBCs were constantly flowing through the microchannel. The RBCs were then recorded by the high-speed camera 1 cm after the inlet.

In the following it is tested whether the cells are relaxed into a stable shape for different positions after the inlet of the channel. The typical relaxation time for healthy RBCs is found to be in the range of t=0.1 ms [17] so that the cells ideally needed 500 µm to relax in a stable shape for velocities of v_{RBC}=5000 µm/s. Figure 4.7 shows that the cells adopt constant shapes after around 2000 µm for a velocity of v_{RBC}=525 µm/s.
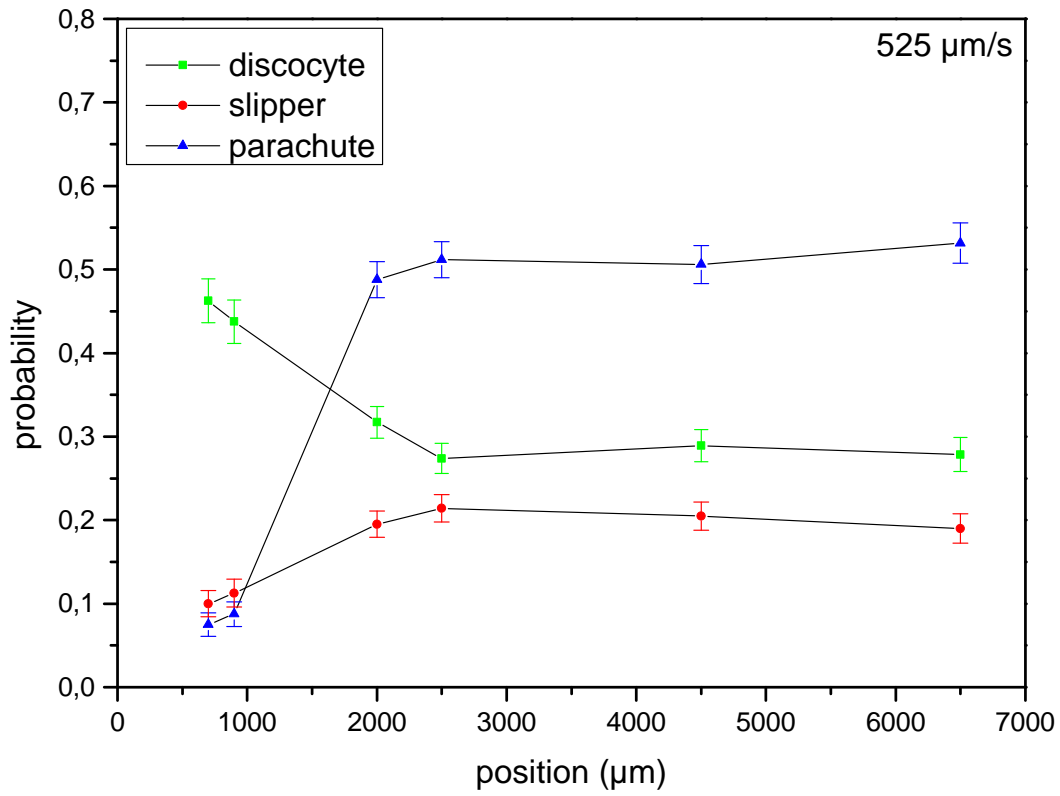
Figure 4.7: Shape probability of healthy human RBC in dependency on the channel position in a 10 x 10 μm microchannel. The graph shows that for a velocity of v_{RBC}=525 μm/s the cells need some time or channel length to adopt stable shapes.[1]

---

[1]Experiment is based on work done by Susanne Braunmüller [15] jointly with myself [38].

In the following the RBC shape probabilities 1 cm after the inlet were investigated in dependency of their velocity. Before each video acquisition, the reservoir was set to a constant height to measure shape probabilities at a constant velocity. At each measurement, 20 to 70 RBCs were recorded while flowing through the channel. Then the videos were analyzed and the total numbers of discocytes, slippers and parachutes were counted. For each constant velocity, a data triple representing the probability of discocyte, slipper and parachute occurrence could be determined. The accuracy of the estimate was calculated by a confidence interval of 68 %. The velocity was calculated from the frame rate and the traveled cell distance. Finally, all data was plotted in dependency on the velocity. Data points of the parachute and discocyte probabilities were fitted using a Boltzmann fit. The slipper line was the difference of 100 % and the two other probabilities (discocyte + parachute). The main purpose of the curves is to provide a guide to the eye. However, they qualitatively explain the observed behavior and its main feature as monotone increase and decrease, saturation and sum of probability to be always $P{=}100\%$. To identify a transition velocity from one shape into the other two positions were used. The intersection of the two Boltzmann fits v_c and the maximum slipper velocity v_c^* were used.
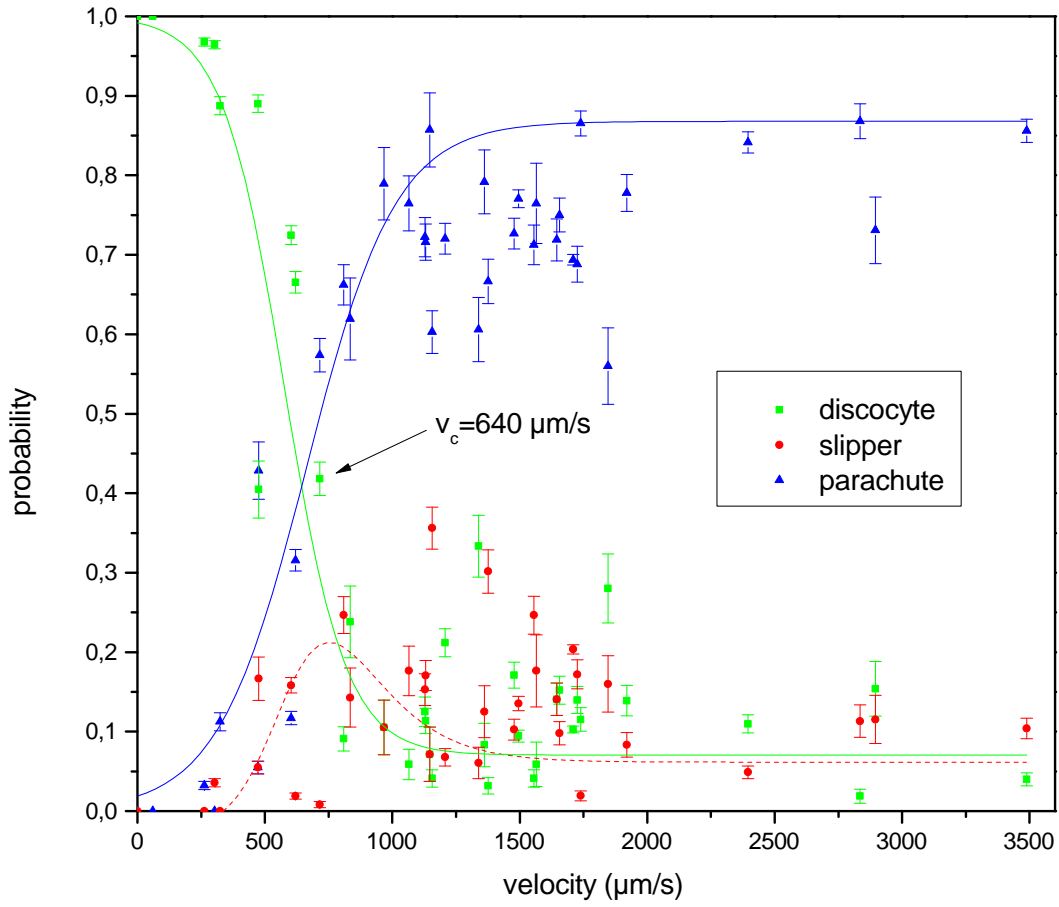
Figure 4.8: Observed native RBC shapes in a 10 x 10 μm PDMS microchannel depending on mean cell velocity. Error bars indicate the confidence interval of 68% as the estimation accuracy. The continuous lines are fits (sigmoid Boltzmann). The dashed line describes the probability of slipper occurrence. As transition point, the intersection of parachute and discocytes is used ($v_c = 640$ μm/s) and the maximum of slipper probability is found to be at $v_c^* = 750$ μm/s.[2]

_____

[2]Experiment is based on work done by Susanne Braunmüller [15] jointly with myself [38].

Figure 4.8 shows all the data for healthy human RBCs. The discocyte shape configuration shows very high probabilities of P=90 % to P=100 % for velocities up to v_{RBC}=480 µm/s. In the velocity-regime of v_{RBC}=480 µm/s to v_{RBC}=750 µm/s there is a strong decrease of the probabilities to only P=15%. For cell velocities higher than v_{RBC}=750 µm/s, the probability stays as low as around P=15 %. In contrast to the discocytes the parachute occurrence increases inversely. For slower velocities than v_{RBC}=500 µm/s, the probability is lower than P=20 %. The probability increase is slightly lower and thus in a larger velocity regime from v_{RBC}=500 µm/s to v_{RBC}=1250 µm/s. Here, the probability increases from P=20 % to around P=80 %. This is also the maximum shape probability for parachutes even at very high velocities of around v_{RBC}=3500 µm/s. The weak increase of parachutes and strong decrease of discocytes is accompanied by an increasing slipper probability. In the transition region between v_{RBC}=500 µm/s and v_{RBC}=1500 µm/s this shape configuration reaches a maximum probability of P=20 % and keeps a constant probability of P=10 % even for very high velocities. Finally, the two shape transition velocities can be indicated: $v_c = 640$ µm/s and v_c^*=750 µm/s.

In figure 4.9, the same experiment is depicted with RBCs that are incubated with either diamide or formaline. Modification of RBCs with diamide (c=0.34 wt%) increases the transition velocity v_c to v_c=2250 µm/s, a dramatic increase compared to v_c of native RBCs (see figure 4.9 (top)). Consequently, for higher velocities the parachute probability is very low and the discocyte probability very high, respectively. The slipper probability reaches its maximum probability of P=40 % at a velocity of v_{RBC}=1000 µm/s. Compared to native RBCs the slipper probability is increased by a factor of 2. However, the minimum observed discocyte probability is increased to a factor of P=20 % and the maximum parachute probability is lowered to P=20 %. In summary, the diamide modification shows an increased slipper probability and a lowered parachute number. Modifying the RBCs with formaline (c=18.4 wt%) yields a different probability distribution (see figure 4.9 (bottom)). The transition v_c is increased by a factor of two to about v_c=1300 µm/s. Again, the minimum discocyte probability is lowered to about 20% and the maximum parachute probability is lowered to about P=50 %. However, slipper shapes are increased to a maximum probability of P=60 % at velocities of around v_{RBC}=1100 µm/s.
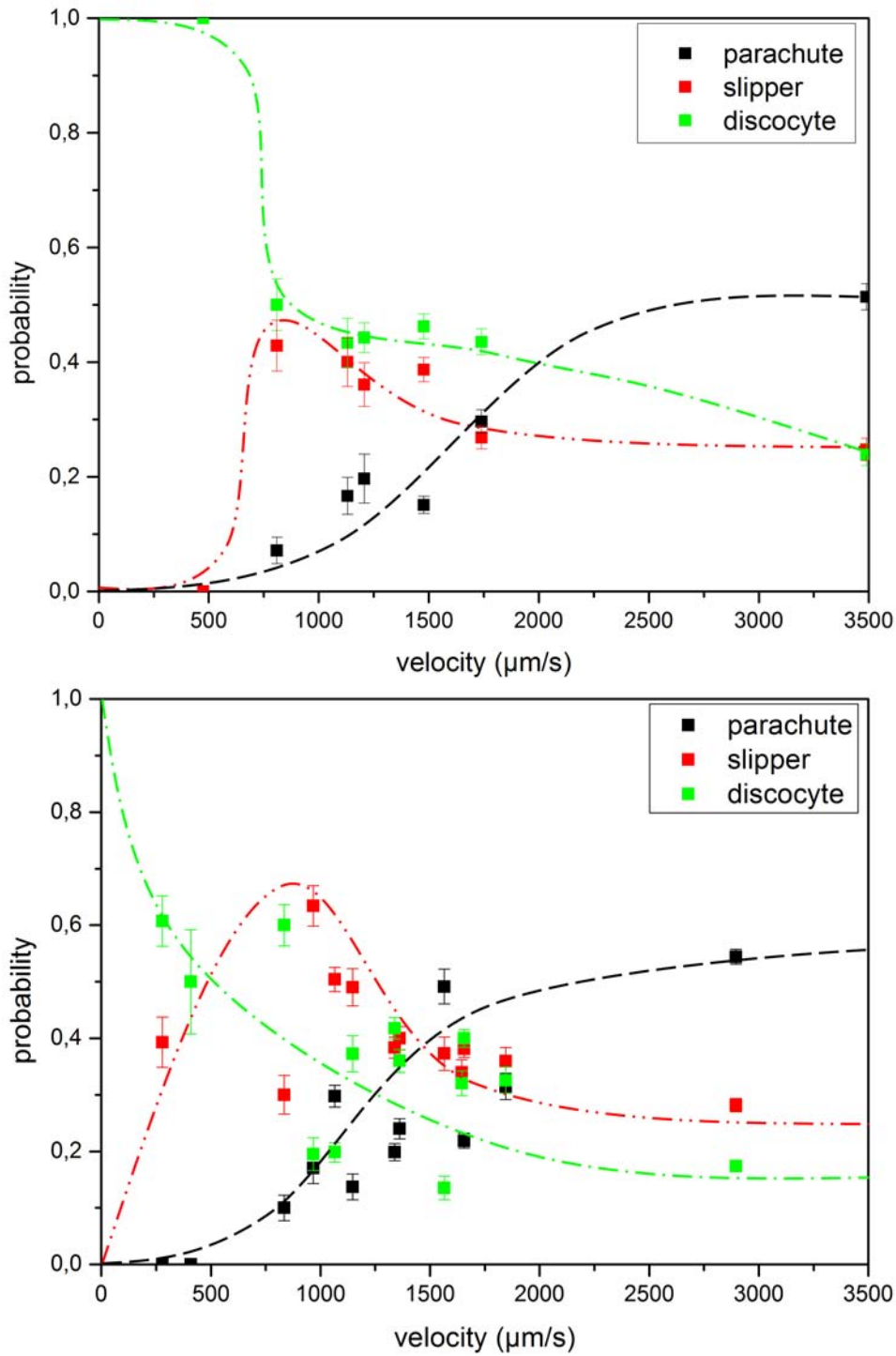
Figure 4.9: Observed shape probabilities of human RBCs modified with di-amide (top) and formaline (bottom). Dashed lines are a visual aid and error bars indicate a confidence interval of 68%. Both chemicals show an increased transition behavior from discocyte (green squares) to slipper (red circles) to parachute (blue triangles) shapes. (Contains data from [38])

In the following the shape probability of cholesterol modified RBCs is described. The experiments were performed in the same way as described above. In the materials and methods (see section 3) it is described that RBCs were either cholesterol enriched or depleted. Figure 4.10 (top) shows the shape probability for RBCs having a high cholesterol content in the membrane and figure 4.10 (bottom) illustrates the influence on the shape probability for RBCs with a low cholesterol concentration.

Discocytes that have a cholesterol enriched membrane were only observed until velocities up to v_{RBC}=100 μm/s, with a very high probability of around 100 %. The probability for discocytic shapes decreased from P=100 % to P=20 % in the velocity regime of v_{RBC} =100 μm/s to v_{RBC}=800 μm/s. For higher velocities, the probability was as low as P=10 %. In contrast, discocytes which had a cholesterol depleted membrane showed a very high probability of P=100% up until velocities of v_{RBC}=250 μm/s. The probability decreased in a much broader velocity range from v_{RBC}=250 μm/s to v_{RBC}=1250 μm/s to a very low probability of less than P=10 %. For very high velocities, no further discocytes were observed. Again, the parachute shape probability increases as the discocyte probability decreased, for both the cholesterol enriched and depleted RBCs. Cholesterol enriched parachutes increased their probability from P=0 % to a maximum probability of P=90 % in the range of v_{RBC}=250 μm/s to v_{RBC}=1100 μm/s. The cholesterol depleted parachutes showed a very slow increase in probability. For velocities up to v_{RBC}=250 μm/s hardly any parachutes were observed; then the probability increased to P=90 % up to a velocity of v_{RBC}=1250 μm/s.

In the case of cholesterol enrichment, the slipper shapes showed a very low probability in total. For mean cell velocities between v_{RBC}=250 μm/s and v_{RBC}=1250 μm/s there was a low probability of maximally P=10 %. Cholesterol depleted cells show higher probabilities. They occurred at velocities of around v_{RBC}=250 μm/s, with a maximum probability of P=20 % at a velocity of v_{RBC}=700 μm/s. At high velocities there was also a very low probability of P=5 % for slipper shapes.
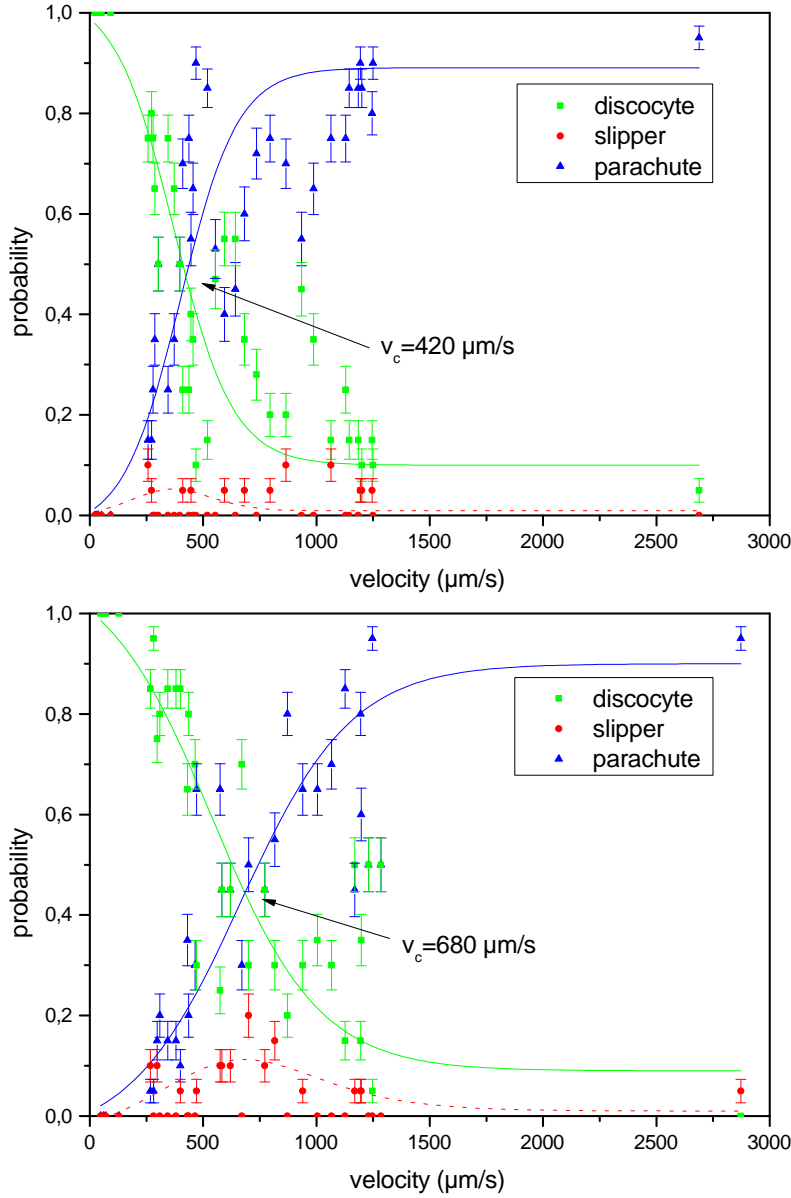
Figure 4.10: Observed shape probabilities P of human RBCs for both a cholesterol enriched (top) as well as a cholesterol depleted (bottom) plasma membrane (see section 3). Shape probabilities in dependency of mean cell velocities were measured in a 10 x 10 µm PDMS microchannel. The error bars indicate a confidence interval of 68% and the continuous lines are visual aid fits (sigmoid Boltzmann). The dashed line calculated by 1-parachutes-discocytes describes the probability behavior for slippers.[3]

---

[3]Experiment is based on work done by Kerstin Wittmann [164] jointly with myself.
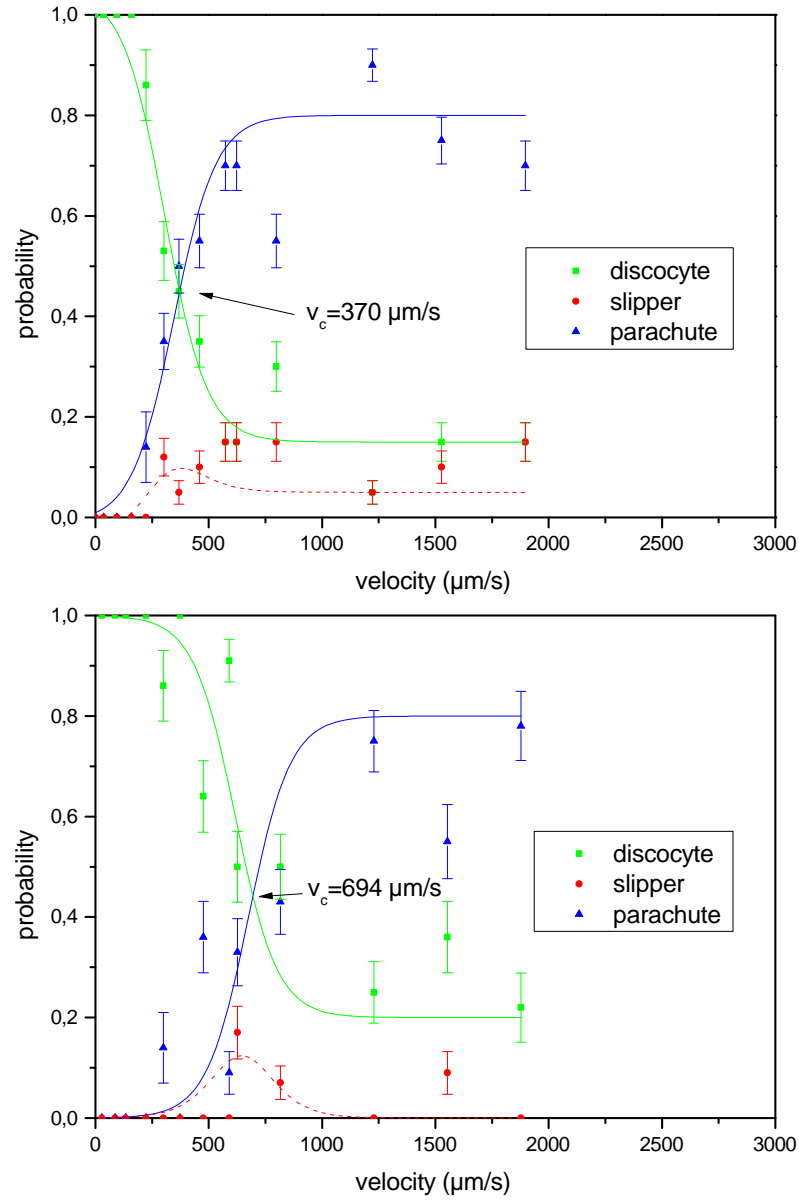
Figure 4.11: Observed shapes of human RBCs in two different buffer osmolalities. The top image shows the results of a measurement at a buffer osmolality of c_{osm}=259 mOsm and the bottom image c_{osm}=404 mOsm. The shape probabilities are counted in a 10 x 10 μm PDMS microchannel. The velocities are mean cell velocities. Error bars indicate the confidence interval of 68% as the estimation accuracy. The continuous lines are fits (sigmoid Boltzmann) and should be interpreted as a visual aid. The dashed line is calculated in the same fashion as in the experiment with healthy RBCs.[4]

---

[4]Experiment is based on work done by Kerstin Wittmann [164] jointly with myself.

In the following, experiments of RBCs treated at different osmolarities are described. Two osmotically different solutions were used as flow medium (c_{osm}=259 mOsm and c_{osm}=404 mOsm). In previous experiments (see appendix A.11) the cells were tested for different osmolarities to see whether they lyse or not. In these tests the range between c_{osm}= 259 mOsm and c_{osm}= 404 mOsm was identified (blood serum has an osmolality of c_{osm}=290 mOsm to c_{osm}= 300 mOsm). The low osmolality shrinked the RBCs due to the lowered water content of the cytosol, while the high osmolality swelled the cells. Figure 4.11 (top) shows the shape probability for a flow medium with c_{osm}= 249 mOsm and figure 4.11 (bottom) for a flow medium having an osmolality of c_{osm}= 404 mOsm.

Regarding the discocyte shape occurrence, the discocyte number decreased from nearly P=100 % steeply in the transition region. For RBCs having a high inner pressure (c_{osm}=259 mOsm), the discocyte probability decreased between v_{RBC}=250 µm/s and v_{RBC}=750 µm/s from P=100 % to P=15 %. P=15 % was also their final probability, even for the high velocity-regime. On the other hand, discocytes having a lower inner pressure decrease in the region of v_{RBC}=400 µm/s to v_{RBC}=900 µm/s from P=100 % to P=20 %. Again, the probability stayed as low as P=20 % for the high shear stress region. In similar fashion the probability for parachute shapes increased with velocity. RBCs flowing in the low osmolality buffer had an increasing probability from P=0 % to their maximum probability of P=80 % in the velocity range of v_{RBC}=250 µm/s to v_{RBC}=600 µm/s. In contrast, RBCs flowing in the high osmolality medium had a probability increase from P=0 % to a maximum probability of P=80 % in the range of v_{RBC}=300 µm/s to v_{RBC}=1000 µm/s. For osmotically treated RBCs, the slipper probability was different compared to healthy RBCs. The low osmolality modification shows an increased probability of P=20 % starting at a velocity of v_{RBC}=250 µm/s. Even at high shear stress the probability was as high as P=20 %. While a high osmolality showed a maximum slipper probability of P=20 % at v_{RBC}=500 µm/s. Up to 500 µm/s and after v_{RBC}=1500 µm/s the slipper probability was P=0 %. The two shape transition velocities for RBCs which flowed in a medium with an osmolality of c_{osm}=259 mOsm is: v_c=370 µm/s and v_c^*=750 µm/s. In contrast, the two shape transition velocities for a buffer osmolality of c_{osm}=404 mOsm were found to be v_c=694 µm/s and v_c^*=750 µm/s.

After the measurements for healthy and chemically modified human RBCs,

in which artificial alteration was meant as a model for blood diseases, measurements performed with RBCs having real blood diseases will be described in the following. Again, shape probabilities in the PDMS microchannel were evaluated as described in the beginning of this section. Two diseases were investigated: β-Thalassemia and Spherocytosis. Figure 4.12 (top) shows the shape behavior for β-Thalassemia RBCs and figure 4.12 (bottom) for Spherocytosis RBCs.

In the case of β-Thalassemia, the transition from discocyte to parachute was measured to be at v_{RBC}=800 µm/s. The minimum discocyte probability was P=0 % and the maximum parachute probability is P=100 %. The highest slipper probability increased to about P=90 % at a velocity of v_{RBC}=1200 µm/s. However, the shape probability distribution looked different compared to healthy RBC. At a very high velocity of around v_{RBC}=2250 µm/s, the parachute probability decreased and the slipper probability increased again.

The measurements regarding the disease Spherocytosis showed a completely different picture compared to healthy RBCs or even β-Thalassemia. The transition velocity v_c was found to be v_c=1250 µm/s and the minimum discocyte probability was identified as P=10 %. The highest parachute probability was only 30%. The slipper shapes seemed to be the favorable shape for diseased RBCs, because the probability reached its maximum of P=60 % at v_{RBC}=3000 µm/s. Interestingly, the parachute shape probability and the slipper shape probability behaved oppositely compared to healthy RBCs.
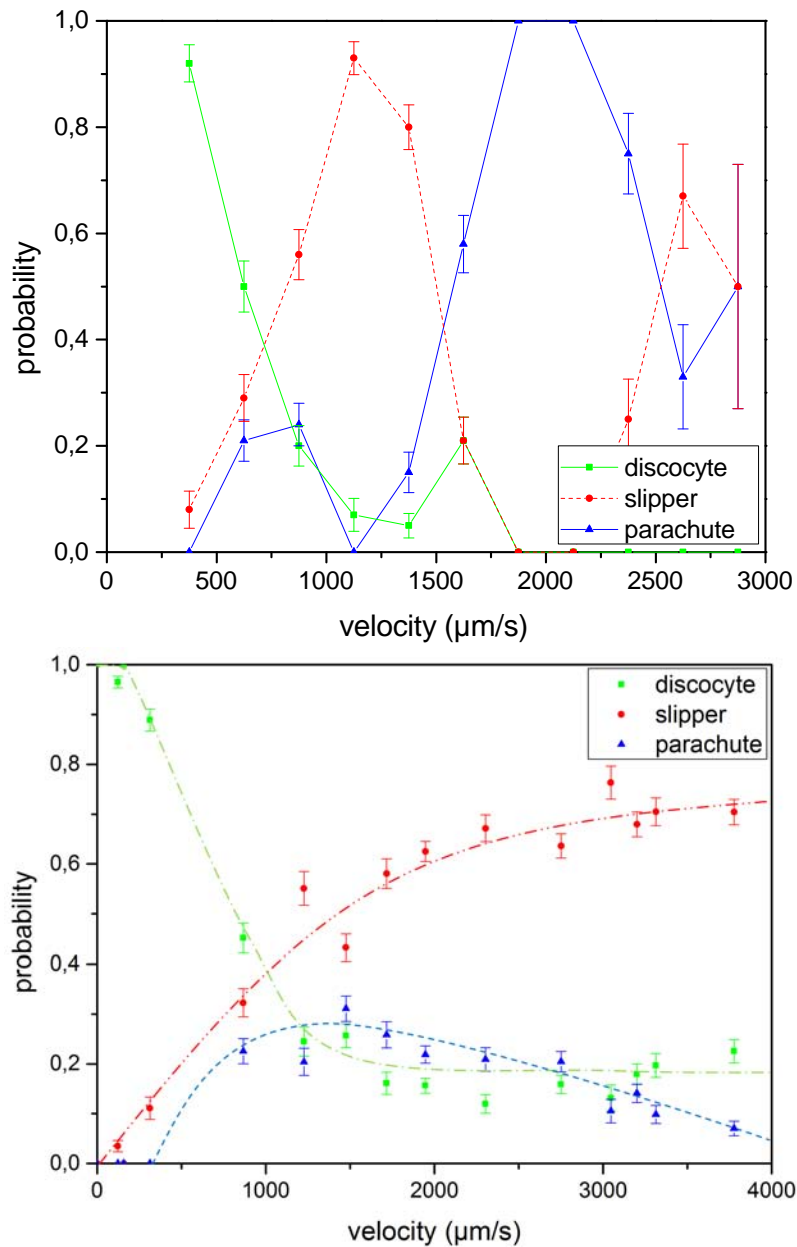
Figure 4.12: (top) The graph shows the shape probability in dependency of the mean cell velocity for RBCs suffering from β-Thalassemia. (bottom) There the measurement for RBCs suffering from Spherocytosis is shown. The error bars indicate a confidence interval of 68 % and the solid lines are guides to the eye.[5]

---

[5]β-Thalassemia-experiment is based on work done by Arturo Castro Nava jointly with myself.

4.5.2 Dependency of the Transition Velocity on deformed RBCs

Several studies investigated shapes of healthy, chemically modified or diseased RBCs in confined geometries at different velocities. It was commonly stated that RBCs changed their shape to axisymmetric parachutes or asymmetric slippers while the shear force acting on them increases [146, 54, 4, 104]. Shapes are physically caused by the interplay of bending and stretching forces acting on the membrane. Governing forces are in an equilibrium mainly determined by the lubrication forces of the fluid passing in the narrow gap between the cell membrane and the capillary walls and the membrane force itself in blood vessels [129].

In contrast the formation of slipper shapes in tiny capillaries with high shear stress is not fully understood [146, 75]. Their existence was experimentally and theoretically observed rarely. The few works dealing with them theoretically confirmed: the slipper existence is dependent on the cell velocity [104] and the center of mass position of the cell relatively to the centerline of flow [146, 75]. In experiments, the slipper was only observed at very high shear stress [1, 153, 54] so far. The RBC shape dependance on flow rate was thus observed in the experiment. For healthy RBCs, slippers occurred in the intermediate velocity regime between the discoid and parachute morphology as already predicted by the mesoscopic simulations of Noguchi et al. [104]. In the described experiment, these non-axisymmetric slippers were remarkably stable, supporting theoretical results by Kaoui et al. [75]. They performed simulations of two dimensional vesicles.

Furthermore, chemical modifications and RBC diseases were investigated. The transition velocities are summarized in table 4.4.

In the theoretical part of the thesis, the architecture of the RBC was introduced (see section 2.1.1). RBCs are governed by an excess surface area. In the biconcave discoid rest shape, the surface area encloses a volume of around 90 fl and the surface area A_S is around $A_S=97\,\mu m^2$ [24]. Exposed to shear stress the spectrin inside the cytoskeleton unfolds comparable to an entropic spring [12]. The excess surface area is expanded up to areas of $A_S=140\,\mu m^2$ [24]. The spectrin tetramers have a characteristic length of $a=70\,nm$ in the unfolded state [97] which is one side (a) of a triangle. The number of triangles

	v_c	v_c^*	P1	P2	P3
native	640	750	5%	85%	20%
formaline (18.4wt%)	1300	1100	20%	50%	60%
diamide (0.34wt%)	2250	1000	20%	20%	40%
cholesterol +	424	370	1%	89%	5%
cholesterol -	685	675	9%	90%	11%
259 mOsm	370	375	15%	80%	10%
405 mOsm	694	645	20%	80%	12%
Spherocytosis	3000	1250	10%	30%	60%
β-Thalassemia	800	1200	0%	100%	90%

Table 4.4: Results of the shape probability determination. v_c denotes the critical velocity determined by the intersection of the parachute and discocyte probability and v_c^* identifies the velocity for the highest slipper probability P3. P1 characterizes minimum discocyte probability and P2 the maximum parachute probability.

N expanding the hexagonal network can be calculated as follows

$$N = \frac{4A_S}{\sqrt{3}a^2} \tag{4.3}$$

Setting A_S as $97\,\mu m^2$ and $a = 70\,nm$ a total triangle number N of 45,717 can be calculated. Upon shear stress on the hexagonal network the spectrin domains unfold and A_S increases to $140\,\mu m^2$ and the tension of a single spectrin tetramer can be calculated (see equation 2.3). Accordingly, the maximum length variation of the spectrin tetramer is $\delta a = 14\,nm$, so that the total length increased to $a = 84\,nm$.

The unfolding of the network is displayed in figure 4.13. As explained in the caption, the red line describes the relation between surface increase and spectrin tetramer length. The start describes the unfolding situation as is the case for the discocyte and the end depicts the situation for the complete unfolding situation as for parachute shapes. Between the start and the end, the slipper shape is stable. Higher shear stress does only deform the parachute shape.

This model can be applied to the chemical modifications as well as to the diseases. As mentioned in the theoretical part, cholesterol enrichment increases the plasma membrane area only. The cytoskeleton and the plasma membrane are connected by trans-membrane proteins. Modifications of the cytoskeleton affect the plasma membrane vice versa. Consequently, the cytoskeleton is
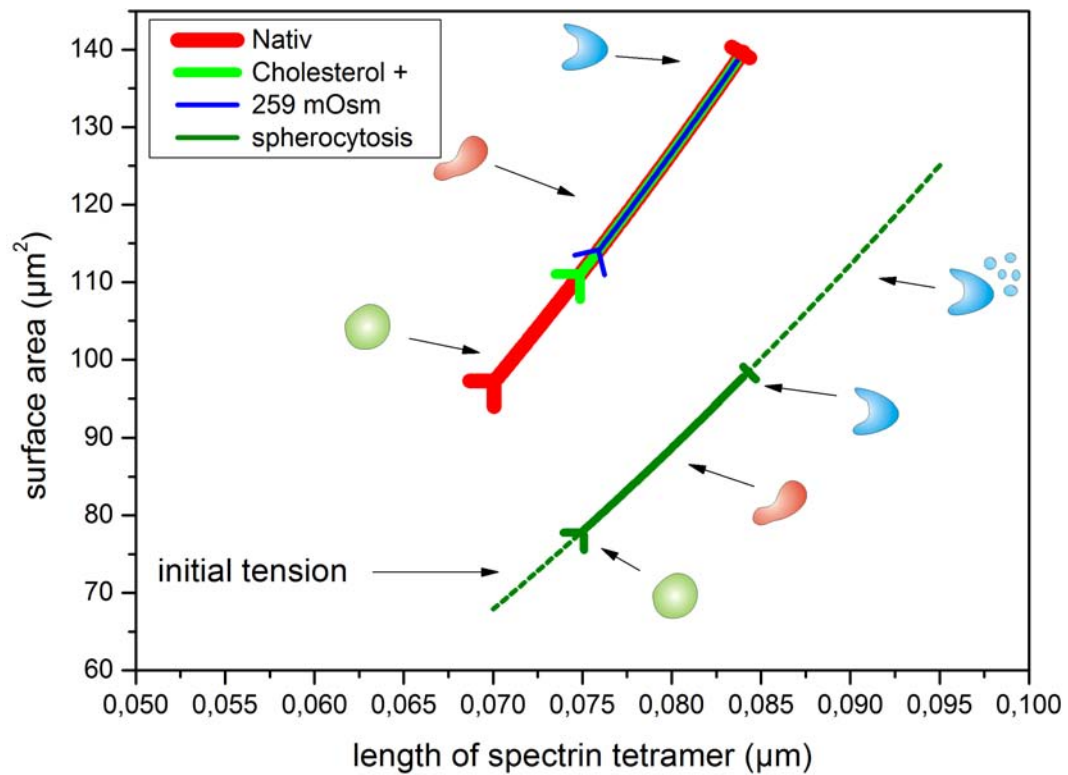
Figure 4.13: Illustration of the RBC surface area in dependency on the spectrin tetramer length. The red line displays the situation of healthy RBCs. The beginning of the line characterizes the situation of the discoid rest shape and the end characterizes the situation of the parachute shape. Between the start and the end, the probability for forming a slipper shape increases and decreases respectively.

under an initial tension. In the experiment the cholesterol modified RBCs were observed changing their shape from discocyte to parachute at lower shear stress than healthy RBCs. The initial tension is a possible explanation for the lowered transition velocity. Moreover, slipper shapes show a lowered maximum probability and occur at even lower velocities. In the model framework, this also corresponds to an initial tension, since the spectrin tetramers need less external tension to unfold. In contrast, cholesterol depletion corresponds to a plasma membrane area decrease. This compresses the cytoskeleton so that the spectrin unfolding is hindered. Upon shear stress, the spectrin cannot unfold on the same time scale as for healthy RBCs because the tension caused by the reduced plasma membrane has to be overcome first. The experiment supports the model as the transition velocities are increased.

Compared to the cholesterol enrichment the same effect as for osmotically swollen RBCs should be observed because the increased inner pressure should correspond to an initial tension of the cytoskeleton. In the experiment, the transition velocity was lowered to half the shear stress compared to healthy RBC. On the other hand, lowering the inner pressure by increasing the osmolarity compressed the cytoskeleton and the plasma membrane in the same fashion as cholesterol depletion. The model reflects the increased transition velocity correctly.

Both osmotic pressure changes and cholesterol modification are indirect methods for altering the cytoskeleton. Diamide and formaline modification directly changes the mechanical properties of the cytoskeleton. The chemicals are known to increase the number of cross-links. In the model this corresponds to a modified spring constant. In the case of formaline, cross-links are introduced between spectrin dimers and tetramers. In the experiment, the formaline modified RBCs showed a transition velocity that was increased to $v_{RBC}=1300\,\mu m/s$. Regarding the spectrin monomers as springs in a hexagonal network, the effective spring constant of the complete network was increased due to the cross-linking. The increased effective spring constant did not affect the unfolding of the spectrin tetramer of $\delta a=14\,nm$, but higher forces were necessary to unfold it completely. In the model the parachute only occurs for unfolded spectrin tetramers. The situation for diamide modification was similar. The chemical cross-linked the cysteins inside the spectrin monomer. Consequently, the single springs show an increased spring constant. The very high transition velocity of around $v_{RBC}=2250\,\mu m/s$ supports the model.

In summary, regarding the hexagonal network as a triangular connected spring network, which is able to extend by about δa=14 nm per side, the shape changes from a discocyte to a parachute with an intermittent slipper shape can be understood. Cholesterol and osmotic variations change the network indirectly by applying an initial tension, while chemical modification influences the network directly by varying the spring constants. However, is the model also able to explain real anemia?

In the case of hereditary Spherocytosis, the surface to volume ratio of the cells was lowered because the RBCs lose membrane area by the release of microvesicles. The reasons for the release are defects in the transmembrane proteins (see section 2.1.2). The samples measured in the experiments were found to have an ankyrin and spectrin defect (discussion with Prof. Kohne). For this mutation, Mohandas and Perrotta [109] identified a reduction of spectrin by about 15 to 50 %. In the here measured RBCs, the reduction was around P=30 % (discussion with Prof. Kohne). In contrast to cholesterol depletion, not only the plasma membrane was affected but also the cytoskeleton as the released microvesicles removed material from the membrane (plasma membrane and cytoskeleton parts). Thus the total number of triangles N is lowered to N=32,002 if a 30% lower surface area A_S is used for equation 4.3. RBC suffering from Spherocytosis show a decreased cell size so that the visible surface area is lowered to A_S=77 μm² (see appendix A.7). The spectrin tetramer length is a=75 nm and the cytoskeleton has an initial tension length of δa=5 nm (see olive line in figure 4.13). The initial tension favored the transition to slipper shapes, but parachute shapes were hard to achieve because high shear stress was necessary to unfold the decreased network. Measurements of Waugh and La Celle [160] reported that the plasma membrane area of Spherocytosis RBCs was lowered to A_S=131 μm². Consequently, the connection between cytoskeleton and plasma membrane is reduced and it is not possible to expand the complete excess surface area. Moreover, very high shear stress favors the release of microvesicles.

4.6   Phase Diagram

RBCs in the human body are not subjected to an unbounded flow, since the flow environment of the circulatory system is characterized by capillary diameters ranging from 2 μm to 2 cm. It is important to characterize the shape distribution for RBCs at the same shear stress and different capillary diameters to simulate physiological flow environments. In the experiments, the shape distribution of healthy, chemically modified and diseased human RBCs were measured in small and slightly tapered glass capillaries. In that way, the influence of the wall on the shape distribution could be measured.

Recently, Abkarian et al. [1] published a shape phase diagram. There, the shapes are characterized as a function of external shear stress in dependency of the dimensionless particle cell size (see figure 4.14 (top)). Above a shear stress of τ=700 Pa, the cells transform from a parachute shape into a slipper shape. Furthermore, the presented phase diagram is measured at larger viscosities than 1 mPas. As mentioned before, the situation for lower shear stresses is more interesting from a physiological point of view. Microvessel networks consist of venules (diameter: $2R$ =20.6 μm), arteriols (diameter: $2R$ =13.2 μm) and capillaries (diameter: $2R$8.72 μm) [113, 116] and average blood velocities of v_{RBC}=1070 μm/s, v_{RBC}=2030 μm/s and v_{RBC}=850 μm/s [116, 8], respectively.

A phase diagram of shapes showing seven distinct regions depending on flow and structural parameters (=dimensionless number measuring the flow strength over the cell deformation) and the degree of confinement (=cell diameter in dependency on the channel width) was simulated by Tahiri et al. [146] (see figure 4.14 (bottom)). The symbols refer to the computed data, while the line is a visual aid. The phase diagram is calculated for a viscosity ratio of 5.
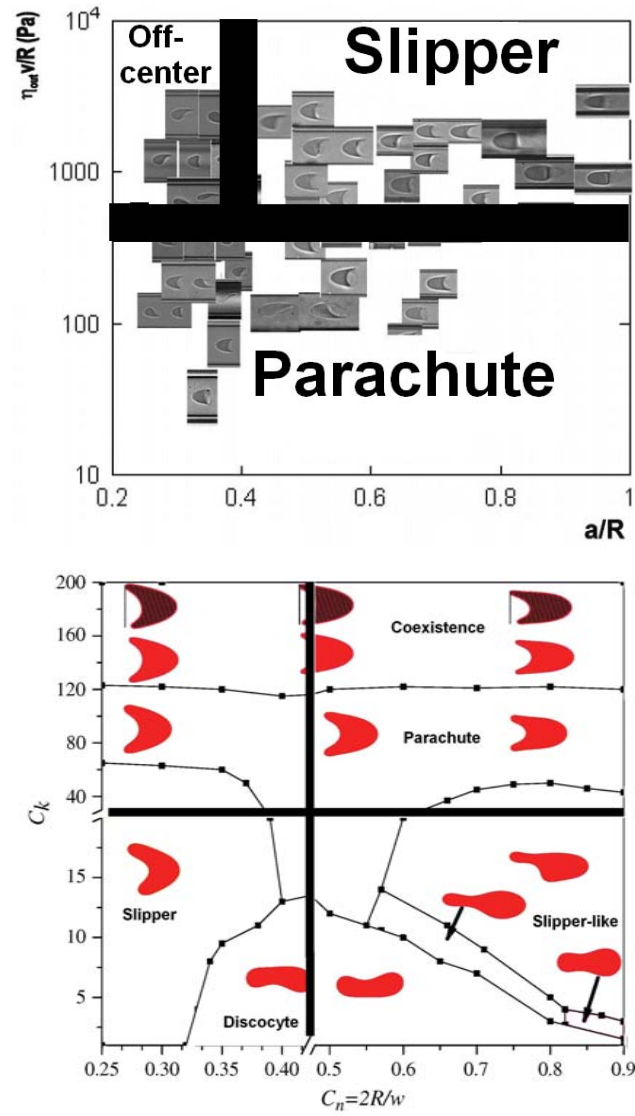
Figure 4.14: (top) Phase diagram of RBC shapes. The shapes are characterized as a function of external shear stress in dependency on the non-dimensional particle cell size. Above a shear stress of 700 Pa, the cells transform from a parachute shape into a slipper shape. (reprint from [1]) (bottom) A simulated phase shape diagram shows seven distinct regions depending on flow C_k and structural parameters C_n (=dimensionless number measuring the flow strength over the cell deformation) and the degree of confinement (=cell diameter versus the channel width). The symbols refer to the computed data, while the line is a visual aid. The phase diagram is calculated for a viscosity ratio of 5. For $C_k > 120$ (very high shear stress) a new domain where the parachute can transform into a slipper shape with possible coexistence between the parachute and slipper shapes is predicted. This new domain is not found for a viscosity ratio of 1. (reprint of [146])

For $C_k > 120$ (very high shear stress) a new domain where the parachute can transform into a slipper shape with possible coexistence between the parachute and slipper shapes is predicted. This new domain is not found for viscosity ratios of 1.

The next section identifies the shape distribution of healthy and modified RBCs for a broader range of fluidic environments than in the previous section because the channel diameter is slightly tapered. Note that the glass capillaries have a round shaped cross-section. The transition conditions are thus not exactly the same.

4.6.1 Determination of Shape Phase Diagrams

The experiment was conducted in a comparable way as described in section 4.5. Via a tube, the reservoir was connected to the wide end of a glass capillary. The capillary was fixed on a glass slide and the other end of the glass capillary was introduced into a PDMS basin that also contained flow solution. Furthermore, the tip of the capillary was tapered, having a taper angle of around $0.15°\pm0.01°$ and an inner diameter of $2R_{cap} \approx 2\,\mu m$. By lifting the height-adjustable reservoir, the flow in the capillary started and RBCs flowed through the narrow tip into the PDMS basin. The height difference between the reservoir and basin controlled the medium velocity and thus the cell velocity. Since the capillary was tapered, a range of channel diameters could be measured in one experiment. In the following experiments, the capillary diameters were between $2R_{cap} = 3$ to $10\,\mu m$ and velocities up to $v_{RBC}{=}4000\,\mu m/s$. Firstly, the three shapes: discocyte, slipper and parachute were counted at a constant diameter and different velocities. A systematic variation of both the flow rate and the capillary radius (different observation position along the tapered capillary) in the experiments yielded a phase diagram of the shape probability. As the experiments of section 4.5 showed, the shape transition from the discocyte to the parachute shape with an intermittent slipper shape was dependent on the shear stress. The transition was characterized by the curvature of the parabolic velocity profile of the capillary flow (see section 2.3). The parameter that is investigated to see the connection between flow and shape is the radial curvature of the velocity flow profile. To identify the critical curvature, an unbounded flow was assumed. The critical velocity v_{RBC}^* and the factor $R^2{-}\frac{2}{3}r_{RBC}^2$ which is explained in section 2.3 are used to calculate

the curvature of the unbounded flow.

$$c = 2 \cdot \frac{v^*_{RBC}}{R^2 - \frac{2}{3}r^2_{RBC}} \tag{4.4}$$

In the following v_0 is the maximal Poiseuille-flow velocity and R may be identified with the capillary radius but has no physical meaning in an unbounded flow. The transition occurs for a critical value c^*. Assuming $r_{RBC} \ll R$ and $v_{RBC} \ll v_0$ the critical velocity of an infinitesimal small cell is given by $v^*_{RBC} = c^* \cdot R^2/2$. Note that this is valid only for a very small object and neglecting wall effects. However, the velocity of the cell is always smaller than the maximal velocity at the center of the undisturbed flow v_0. An axis-symmetric cell of finite size always extends into regions of lower velocities of the Poiseuille-flow. For a rigid sphere or a cell with radius r_{RBC} the cell velocity is given by the parameters v_0 and R of the undisturbed flow without the cell: $v_{RBC} = v_0 \cdot (1 - \frac{2r^2_{RBC}}{3R^2})$. This is independent of r because it is assumed that the cell is always flowing in the center of the capillary. The critical velocity for a finite cell is then shifted to $v^*_{RBC} = \beta \cdot \frac{c^* R^2}{2} (\beta = 1 - \frac{2r^2_{RBC}}{3R^2})$. v^*_{RBC} is linearly dependent of the capillary radius R^2. The linear curve has an intersection $v^*_{RBC} = 0$ at $R = \sqrt{2/3}r_{RBC}$. Figure 4.15 shows the phase diagram for healthy human RBCs. Each measurement point contains a data triple identifying the shape probability of discocytes, slippers and parachutes. The squares represent the probability for the discocyte shapes, the circles represent the slipper shapes and the triangles reflect the parachute shape probability. The edge length of the symbol is scaled to the probability of the corresponding shapes. The linear curve is using data points for the highest slipper probability (50 %<P<100 %) and the lowest parachute and discocyte probabilities (0 %<P<20 %) in the phase diagram. In that way, the transition can be characterized by the slope of the linear regression.

The discocyte shape probability is highest for low shear environments. For small capillary radii of around 5 μm, the discocyte probability is only high for very small velocities v_{RBC}<500 μm/s. In contrast, capillaries having a radius of $R \approx$17 μm also show a high probability for discocytes at mean cell velocities of v_{RBC}=2500 μm/s.
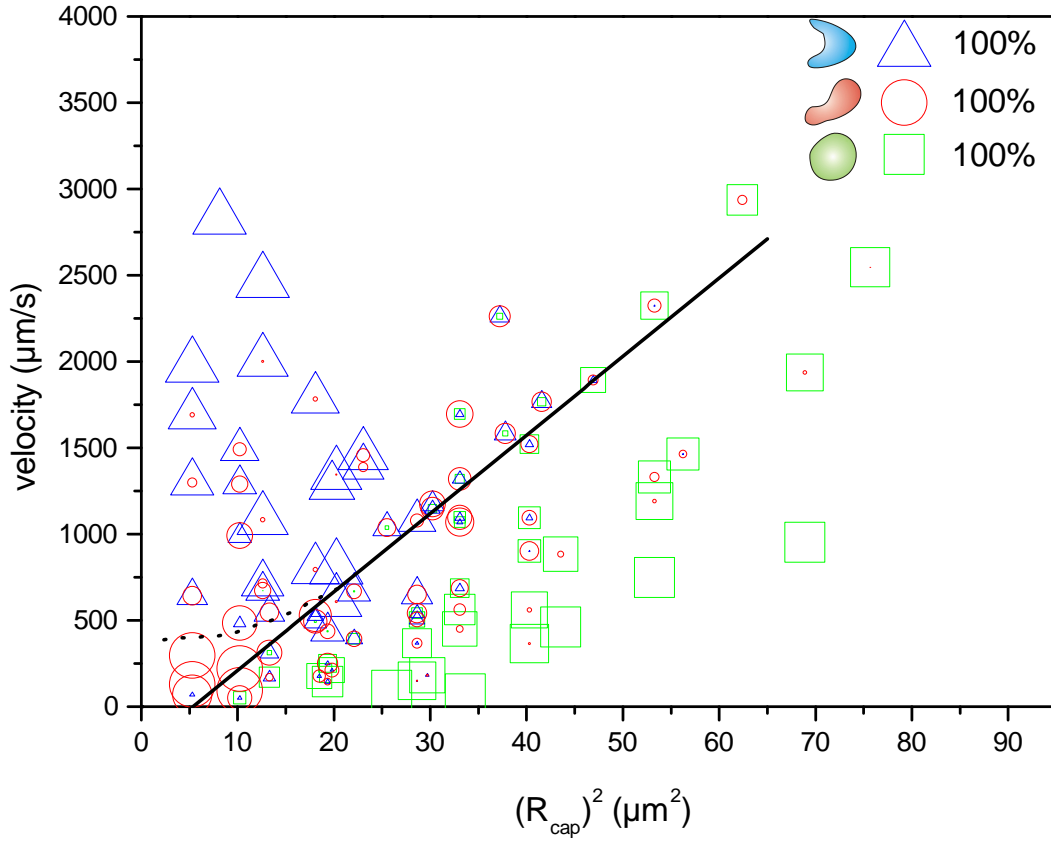
Figure 4.15: RBC shape phase diagram of healthy human RBCs. The size (or more precisely the edge length of the symbol) indicates the probability for the specific shape. In addition to the initial discocyte (square) a slipper (circle) and a parachute (triangle) shape occur. The phase diagram shows the shape probability in dependency of the mean cell velocity and the squared capillary radius. The sum of all probabilities of one triplet is always 100%. The fitted linear regression marks the transition from the discocyte to the parachute shape with an intermittent slipper shape. To obtain the linear fit only data points for the highest slipper probability (50%<P<100%) and the lowest parachute and discocyte probabilities (0%<P<20%) were taken into account. The curve follows the formula 4.4. The corresponding critical curvature is found to be $c^* = 45.4 \pm 13.5 \, (\mu ms)^{-1}$.[6]

Parachutes dominate the shape distribution in small capillaries from 0 to $5\,\mu m$ in capillary radius and for velocities larger than $v_{RBC}{=}1{,}000\,\mu m/s$. Otherwise, the parachute showed a probability of $P{=}30\,\%$ for high shear stress.

The slipper shapes have high probabilities in the intermediate regime between discocytes and parachutes. For radii of $4\,\mu m$ to $6\,\mu m$ and velocities up to $v_{RBC}{=}600\,\mu m/s$ the slippers showed very high probabilities. The fitted linear regression that characterizes the shape transition of healthy human RBCs had a slope of $c^* = 45.4 \pm 13.5\,(\mu m s)^{-1}$.

Figure 4.16 shows the phase diagram for different chemical modifications (formaline [top left], diamide [top right] and cholesterol [bottom left]) as well as for RBCs suffering from Spherocytosis (bottom right). Regarding the critical flow profile curvatures at the defined shape transition, formaline showed the strongest effect. The slope was found to be $c^* = 95(\mu m s)^{-1}$. In contrast, diamide modification showed a transition parameter of $c^* = 71(\mu m s)^{-1}$. Both chemicals cross-link the cytoskeleton and hinder the unfolding of the spectrin polymers. In contrast to the measurements in the $10\,\mu m$ x $10\,\mu m$ PDMS microchannel, formaline modification affected the transition more than diamide modification. Additionally, cross-linking the spectrin polymers among themselves showed an increased probability for slipper shapes in the flow environments. In contrast, cross-linking inside the spectrin showed a decreased slipper probability. Modifying the RBCs with cholesterol lowered the transition parameter to $c^*{=}36(\mu m s)^{-1}$. In this case, the slipper probability was increased in a wider channel diameter where a high probability in the discocyte and parachute regime was also observed. The disease Spherocytosis showed an even lower transition parameter of $31(\mu m s)^{-1}$ and slightly increased slipper probabilities. In contrast to the $10\,\mu m$ x $10\,\mu m$ PDMS microchannel, parachutes were more often observed.
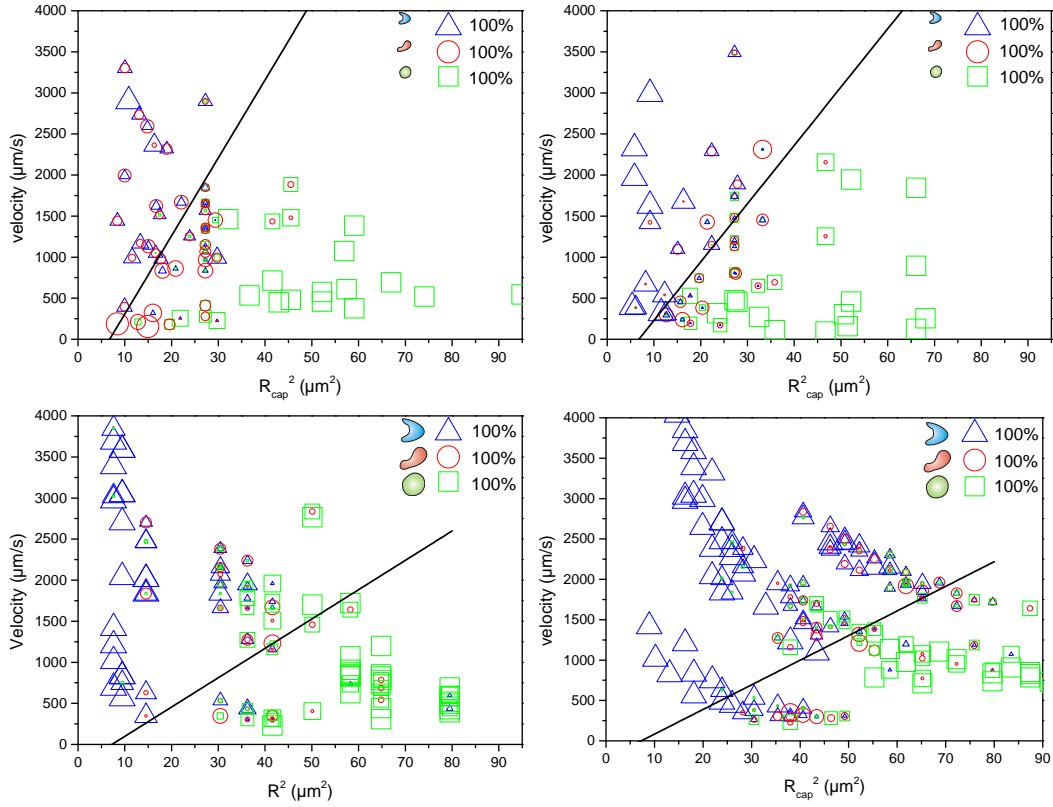
Figure 4.16: Shape phase diagram of formaline modified (top left), diamide modified (top right), cholesterol modified (bottom left) human RBCs, and human RBCs suffering from Spherocytosis (bottom right). The edge length of the symbols indicates the probability for each shape (discocyte is represented by square, slipper is represented by circle and parachute is represented by triangle). The diagrams show the shape probability in dependency on the mean cell velocity and the squared capillary radius. The linear curve is fitted as explained for healthy RBCs.[7]

---

[7]Cholesterol-experiment is based on work done by Santiago Andrade-Cabrera jointly with myself. Spherocytosis-experiment is based on work done by Andreas Wörl [165] jointly with myself.

4.6.2 Phase Diagrams of the Membrane Modifications

Recently Kaoui et al. [75] and Tahiri et al. [146] simulated a phase diagram for dynamic RBC shapes in the microvascular system. For an internal to external viscosity ratio of 5 and a fixed reduced volume, the phase diagram shows constant shape regimes in dependency of the capillary number measuring the flow strength over the bending energy of the membrane and the degree of confinement. The capillary number can be converted into maximum flow velocities and the degree of confinement into a squared capillary radius as in the described measurements to make it comparable to our measurements that are plotted with these parameters. Figure 4.17 is the recalculated theoretical phase diagram.

The phase diagram shows a discocyte regime for low shear stress. This regime is in good agreement with the findings in the measured phase diagram. In contrast, the measurement shows that the parachute probability is not as low as the simulation predicts (see dashed green line). In the capillary experiment parachute shapes become favorable as c of the parabolic flow profiles increases to $c^* = 45.4(\mu ms)^{-1}$. The measurement does not show the coexistence of parachute and slippers at high shear stresses, since no data points are obtained. However, the simulation and the experiment support the finding that slipper shapes are favorable in small capillaries and moderate shear stress. Other experiments by Abkarian et al. [1] and Tomaiuolo et al. [153] have reported that slipper flow occurs upon very high flow strength. Abkarian et al. determined the transition from parachute to slipper to be $c^* \approx 90(\mu ms)^{-1}$ which is significantly higher than $c^* = 45.4(\mu ms)^{-1}$. In the experiments of Tomaiuolo et al., a slipper was observed for high shear stress at velocities of $\approx 0.36\,\mathrm{cm/s}$ (in this theses the upper limit is $0.3\,\mathrm{cm/s}$). Both did not observe slippers at capillary diameters with wall-interaction or between a discocyte parachute transition.

Just as in the $10\,\mu m$ x $10\,\mu m$ (see section 4.5) channel the chemical modifications formaline and diamide shift the shape transition to higher shear stress. For diamide alteration the shear stress to transform RBC from a discocyte to a parachute shape increased by a factor of 1.5 or for formaline by a factor of 2, respectively. However, compared to the transition experiments of section 4.5, the present phase diagram shows that diamide modification is not hindering the shape transition. The increased slipper probability for formaline alteration
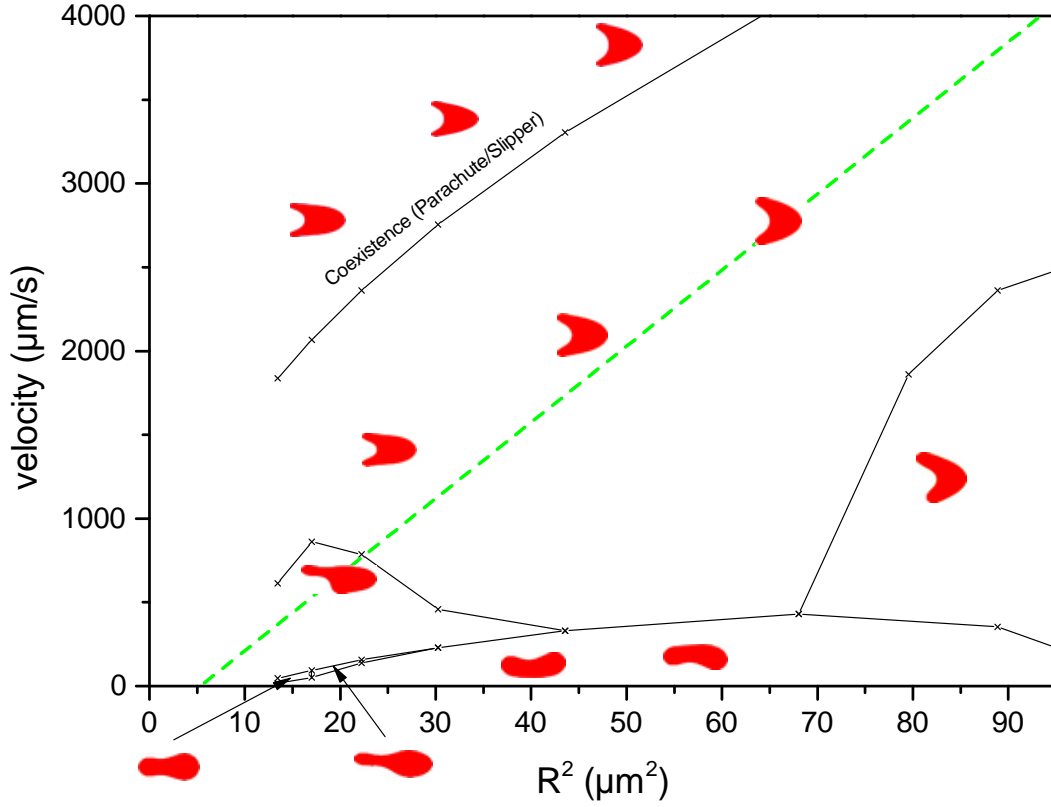
Figure 4.17: Simulated phase diagram for a viscosity ratio (η_{RBC}/η_{fluid}) of 5 (similar to the physiological regime) [146]. In the theoretical work of Tahiri et al. the degree of confinement C_n is dependent on the capillary number C_κ. Both are dimensionless numbers for the flow description. The capillary number C_κ is converted into undisturbed maximum flow velocities by $v_{max} = (C_\kappa \kappa R/2\eta r_{RBC}^3)$ and the degree of confinement C_n to $R^2 = (r_{RBC}/C_n)^2$. RBC radius r_{RBC} is assumed to be $3.3\,\mu m$ [104], viscosity of water $\eta_{fluid} = 1\,mPas$ and $\kappa = 3 \times 10^{-19}\,J$ [11]. Modified from Tahiri et al. [146].

compared to diamide modifications was observed. Nevertheless diamide modification shows a high slipper probability only in the regions between the shape transition from discocyte to parachute. Formaline modifications maintain a very high slipper probability for small capillary radii, in which wall interaction plays an important role. Consequently, the macroscopic model of introducing cross-links in two different ways is verified again. Diamide cross-links the cysteins inside the spectrin tetramer so that unfolding is hindered. The sharp transition from discocyte to parachute with a narrow region of increased slipper probability supports the view that the spectrin unfolding is a very rapid process at a given shear stress. In contrast, the chemical formaline introduces cross-links randomly inside the cytoskeleton. Since the phase diagram looks qualitatively similar compared to the one for healthy RBCs but shifted to higher shear stress, it supports the theoretical model of a denser crosslinked cytoskeleton.

In terms of cholesterol enrichment, the required shear stress for RBC shape change is lowered similar to the observations in the microchannel experiments. Nevertheless, the phase diagram reveals a lowered slipper probability and correlates with the results gained before. However, there is no increased slipper probability for capillary radii supporting wall interaction. The theoretical picture of an initial tension may explain the situation for cholesterol enriched RBCs. The initial tension lowers the RBC shape transition so that lower shear forces are needed to transform the RBCs. Wall interaction behavior of RBCs is similar to very high shear stresses. Consequently, the RBCs can transform into slippers easily in these flow regimes.

RBCs suffering from Spherocytosis need 30% less shear stress to transform into a parachute shape. As already mentioned, the cells show a decreased cell size because the cytoskeleton and the lipid membrane anchoring is decreased so that they lose membrane compartments during their lifetime. As a consequence, the reduced lipid membrane area induces an initial load, comparable to cholesterol modifications. In similar fashion, a lowered shear stress is needed to transform the shapes in the case of Spherocytosis. Additionally, a very increased number of slippers is observable. Not only in the transition region but also for low and high shear stresses, the slipper probability is high. Additionally, the phase diagram shows that there are also flow regimes where the parachute shape is dominant.

4.7   Slip Velocity

In the last sections, the main focus was on the mechanical properties, shape deformation and morphology, as well as on the transition conditions of human RBCs. As introduced in chapter 2.3.5, the deformation of RBCs is not only a change in length and width but also in shape. Three shapes were observed: the discocytic rest shape, an asymmetric slipper and an axisymmetric parachute shape. These symmetric and non-symmetric shapes were observed in the experiments in vivo [133] and in vitro [142, 143, 53, 1, 153] but also in theoretical simulations[75, 146, 104]. The physiological background and the reason for their occurrence is not fully understood. As mentioned the slipper shape is a non-symmetric (related to the flow direction) shape and the membrane is thus able to tank-tread. It is believed that the cells change their shape to increase cytosol mixing and enhance oxygen supply in very small capillaries. However, another alternative functional reason may be the decreasing flow resistance. In a theoretical study (2D simulation), assuming a perfectly flexible membrane and lubrication theory, Skalak et al. [134] have found that asymmetric red blood cell shapes reduce cell velocity and therefore enhance flow efficiency. Recently, Kaoui et al. [75, 146] (2D simulation) have addressed the problem of asymmetric shapes in an unbounded Poiseuille flow more thoroughly. In a two-dimensional analysis they found that a simplified RBC model disregarding shear elasticity (giant fluid vesicle) was sufficient to obtain non-symmetric slipper shapes. With decreasing flow velocity, they observed a continuous shape transition from a parachute to a slipper and concluded the character of the transition to be a supercritical pitchfork bifurcation. Here, one stable branch (parachute shape) was above the critical parameter and two stable branches (slipper shape) below the critical parameter. The transition was accompanied by a reduction of the slip velocity, which was defined as the difference between RBC velocity and fluid velocity of the unperturbed flow at the same position.

In the next section, the transition of a healthy human RBC was observed in detail. The slip velocity v_s is defined as the difference between the RBC velocity v_g and the corresponding unperturbed velocity v_{th} measured at the center of mass position. This means that the RBC velocity does not reflect the maximum velocity of the undisturbed flow velocity without the cell. The slip velocity strongly correlates with the shape transformation. The slip velocity is thus a key parameter to reduce the friction in the vessel. Not only the lifetime

but transport efficiency of the RBCs are expected to be increased by the existence of this lag [75]. In a tapered capillary, the complete shape transition of a single RBC is demonstrated. In the next section the measured RBC velocity is compared to the theoretical undisturbed flow velocity to identify the slip velocity. In that way the slip velocity can be correlated with the hematocrit discharge (see section 2.1.1).

4.7.1 Measuring Slip Velocity

A strongly tapered ($4\degree$) glass capillary was fixed on a glass slide and embedded in PDMS to avoid lens effects by the curvatures of the capillary. The wide end was connected to a height-adjustable reservoir, whereas the tip was connected to a waste reservoir of constant height. The RBCs were pipetted into the tube connected to a height-adjustable reservoir and started to flow through the microcapillary as it was lifted relative to the waste reservoir. The cell velocity could thus be controlled by the height difference very precisely (mirometerscrew). The flow rate was set to a constant value and RBCs were captured flowing through the capillary using the high speed imaging camera.

The strong taper angle $\alpha \approx 5\degree$ of the capillary changed shear stress dramatically over the observation length of $276\,\mu\text{m}$. Consequently, it was possible to observe RBCs changing their shape from a discocyte into a parachute or slipper shape. The inset of figure 4.18 (top) shows an overlay of one healthy human RBC that transits from a discocyte shape into a slipper shape and in the end it started to form a parachute. The two black circles mark the transition positions and the arrows point to the position of the measurement curve. The measurement curve showed the change of the measured cell velocity v^g against the theoretical cell velocity v^{th}. Both v^g and v^{th} were normalized by a reference velocity v_0^g and v_0^{th}. The reference velocity was obtained from the first two frames of the video at the beginning of the experiment. The normalization is necessary because the prefactors $\nabla p/4\eta$, which are necessary to calculate the specific velocity value ($v = (\nabla p/4\eta)(R^2 - r^2)$) correctly, cannot not be measured directly. However, the flow rate Q in the capillary was constant because the overall flow resistance did not change significantly when a single RBC passed the capillary and the pressure drop across the RBC was negligible.

As can be seen from the measurement data in figure 4.18 (top), the measured

RBC velocity increases discontinuously (non-linear). Particularly at positions that correspond to the shape transitions v^g increases more strongly than v^{th} indicating a reduced flow resistance. The blue bisecting line shows the expected behavior of a particle. The measurement shows two important facts. First, the parachute shape has a lower flow resistance compared to slipper and discocyte, due to its high velocity and second, the shape transition lowers the kinetic energy of the particle (lower flow velocity).
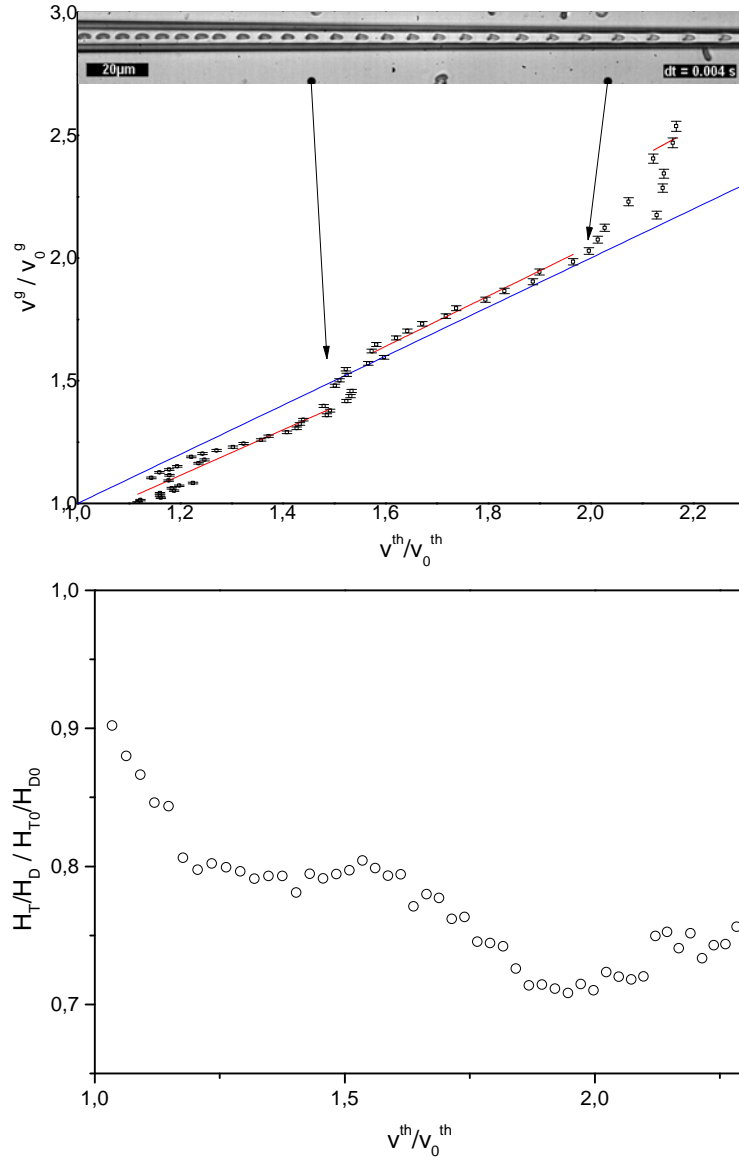
Figure 4.18: (inset micrograph) Chronological sequence of RBC shape changes from a discocyte to a slipper to a parachute of a single RBC in a strong tapered capillary. The flow direction is from left to right. (upper) Measured velocity v^g in dependence of vth normalized by the corresponding reference velocities v_0^g and v_0^{th} at the beginning of the micrograph. The blue curve is the bisecting line indicating an infinite small particle. The red lines show linear fits for the three shape regimes in the tapered glass capillary. During the shape transitions the slope of the measured data changes stepwise. This indicates a changed slip velocity $v^g - v^{th}$. Each data point is the average of 10 measured velocities and is plotted with its standard deviation. (lower) Ratio of hematocrit in the cylinder H_T and discharge H_D, normalized by the value at the reference H_{T0} and H_{D0}. We calculated the ratio from $H_T/H_D = v_m/v^g$ ($v_m = Q/(r^2\pi v^g)$).

The H_T/H_D-dependency of the normalized theoretical cell velocity v^{th}/v_0^{th} was plotted as a macroscopic quantity, again normalized by its value at the reference position H_{T0}/H_{D0}. H_T/H_D is the ratio of hematocrit in the cylinder H_T and discharge H_D and is calculated from $H_T/H_D = v_m/v^g$ ($v_m = Q/(r^2\pi v^g)$). The hematocrit was defined as the volume fraction of RBCs. The plot indicated that the hematocrit in the cylindrical capillary tube $H_T(R)$ was lower than the discharge hematocrit H_D that is collected at the end of the tube. Furthermore, $H_T(R)$ strongly decreased with decreasing capillary radius R and increasing v^{th}. This was a direct consequence of the RBC velocity that was higher than the mean velocity of the fluid $v^g > v_m$ (according to the Fahraeus effect), with the mean velocity given by $v_m = Q/(r^2\pi v^g)$.
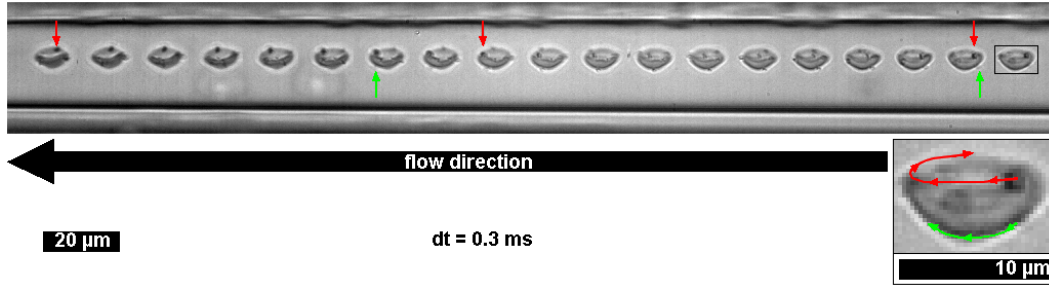
Figure 4.19: Time overlay of an asymmetric slipper shaped RBC. The cell is flowing through a parallel glass capillary of a diameter of $2R_{cap} \approx 23\,\mu$m. The flow direction is from right to left. The first time-shot is magnified and two trajectories of attached beads identify the movement. Red and green arrows mark a specific point on the cell. Due to the Poiseuille flow the RBC shows tank-treading not being located directly in the middle of the channel.

In a theoretical model, Kaoui et al. [75] have found that the slip velocity is related to the lateral position in the channel. Unfortunately, the lateral position of an asymmetric shape, as it is the case for slippers, cannot be determined to such a precision necessary to find a correlation of the shape barycenter and the RBC velocity. The uncertainty of the position introduces a high error value for the velocity of a certain shape that is much larger than the difference of velocities among different shaped RBC.

However, the lateral position or the distance of the RBC from the centerline of a capillary should give rise to a tank-treading motion of the RBC membrane. For a symmetric parachute at the centerline, tank-treading is absent because of the cylinder symmetry of the Poiseuille flow. To demonstrate that membrane tank-treading occurs for off-centered RBC, small polystyrol beads were

attached to the cell membrane. Their trajectories in a parallel cylindrical glass capillary ($2R_{cap} = 23\,\mu$m) could be tracked. The trajectories are displayed in figure 4.19.

4.7.2   Energy Harvesting for Shape Change

The presented experiments showed that RBCs that adopt a parachute or a slipper shape lower the flow resistance because their mean velocity is larger compared to the undisturbed theoretical flow velocity. Theoretical simulations by Kaoui et al. [75] and experiments by Skalak and Branemark [133, 52] show that for small arteries and venules slippers are more favorable than they are in large arteries. At this point it has to be mentioned that most studies treat the slipper shape as a non-stable intermittent shape between the transition from discocyte to parachute. Kaoui et al. conclude that a major advantage of the slipper shape is a reduction in the slip velocity and enhancement of transport efficiency. This theoretical prediction is strongly supported by the reduction in flow resistance (retention time is shorter). The reduction in flow resistance can be directly compared to a hematocrit discharge. The decreased tube hematocrit is therefore explained by the fact that faster RBCs leave the microcapillary earlier compared to the suspending fluid. The results are in accordance with previous studies [153, 142].

Moreover, the theoretical prediction states, that the slipper manifestation is not dictated by the cytoskeleton. Simulations of vesicles without shear elasticity still show slipper shapes. However, it is discussed whether or not, beyond the transport efficiency, the slipper shape is dictated by other physiological determinants. They suppose that the membrane tank-treads in order to efficiently mix the hemoglobin and enhance oxygen distribution in tissues [75]. In the experiments the exact position in narrow capillaries where RBC transit from discocyte to slippers or parachutes is hard to measure. However, in large capillaries and a very high velocity ($v_{RBC} > 2000\,\mu$m/s) a RBC is shown that is off-center (see figure 4.19). The cell adopts a slipper shape and the attached latex beads allow the observation of tank-treading. From that point of view, the results support Kaoui et al. In narrow capillaries RBCs adopt parachute or slipper shape that lower the flow resistance. Furthermore, slipper shapes enhance oxygen transport by tank-treading, thus mixing hemoglobin inside the cell.

4.8 Special Case: RBCs from Alpacas

In this section, the uniquely shaped RBCs from cameloidae in particular from alpacas are investigated. First the flow behavior is characterized and then an induced shape relaxation is measured to characterize the bending modulus of RBCs from Alpaca.

4.8.1 Flow Behavior of Alpaca RBCs

The capillaries of the cardiovascular system in all mammals have a mean diameter of $2R_{cap} \approx 4\,\mu\text{m}$, while slits in the spleen or bones can be as small as $R=0.5\,\mu\text{m}$. The discocytic red cells of mammals show radii from $R=1.05\,\mu\text{m}$ up to $R=4.6\,\mu\text{m}$ and a high deformability is also expressed by shape changes to sustain these enormous high shear stresses reversibly. As an exception, RBC from camels and lamas were found not to deform or change shape although their cardiovascular system is similar to other mammal [137]. The stiffness of RBCs from alpaca was found to have a four times higher bending modulus than human RBCs when performing flickering spectroscopy [173]. So far, only an orientation alignment of the cells from camel and lama has been observed in linear shear stress by taking diffraction patterns on a microscope [137]. However, no data for alpaca RBCs are reported. Thus, the question that is posed, how do RBCs from alpaca behave while traveling through the small capillaries and how do they compensate their lowered deformability, although the mechanical stress for the cells is similar as in other mammals? Observing cells while flowing and deforming in microchannels using high speed imaging is a new method to study flow dynamics and mechanical properties in detail.

Measurements

RBCs from alpaca were investigated in squared PDMS microchannels having a width and height of $w = h=10\,\mu\text{m}$ as well as in round shaped glass capillaries of various diameters. The maximum achievable shear stress τ in these systems was approximately $\tau=320\,\text{N/m}^2$.

Glass Capillary Experiments

RBCs from alpaca were added to the inlet of the glass capillary microstructure that was mounted onto the stage of an inverted microscope. While lowering

Figure 4.20: The time-stack overlay shows a round shaped glass capillary having a diameter of $2R_{cap}$ =8µm. The time-stack overlay shows a typical RBC from alpaca having a mean cell velocity of v_{RBC} =960 mm/s. This velocity is our upper limit and corresponds to a shear stress of τ=320 N/m². The cell does not show any deformation.

a height-adjustable reservoir connected to the outlet of the capillary, cells were sucked into the capillary propagation toward the tip. The height of the reservoir directly controlled the flow velocity and thereby the cell velocity. Using a high-speed imaging camera, the flow of the RBC was observed in the middle of the capillary.

Figure 4.20 shows a RBC from alpaca at the maximum achievable velocity of v_{RBC} =960 mm/s. This velocity corresponded to a shear stress of $\tau \approx$ 320 N/m². Even at this enormous shear stress the alpaca RBC did not show any deformation as indicated by experiments from RBCs of camel and lama.

For studying the flow motions, a capillary having a diameter of $2R_{cap}$ =60 µm was used. Figure 4.21 shows the described microcapillary. In the following, two flow regimes for the specific microcapillary were identified where the typical flow motions of alpaca RBCs were observed. Therefore, an orientation angle Φ was introduced (figure 4.21(d)).

The first regime, the low shear stress regime, was found to be from v_{RBC} =0 to $v_{RBC} \approx$ 1000 µ/s. When increasing the velocity, the cells showed a random tumbling motion. The 180 °-rotations of the cells were found to be independent of the cell position in the channel. However, some of the cells stopped their tumbling motion intermittently for time periods of up to v_{RBC}=500 ms and kept a constant orientation angle Φ of $\Phi \approx$+45° or $\Phi \approx$-45°. This constant flow orientation occurred more often and was more stable for increasing cell velocity. The second regime was identified in the range of mean cell velocities of v_{RBC}=1000 µm/s to 5100 µm/s. In this flow regime the orientation angle Φ started to oscillate. The oscillation of Φ was typical around Φ =0 ° with an amplitude of Φ =35° and Φ =-35° respectively. As Φ oscillated to angles larger than Φ =40 ° the cell tumbled instantly. The intermittent tumbling was always one single rotation of Φ =180 ° before the cell starts oscillating around
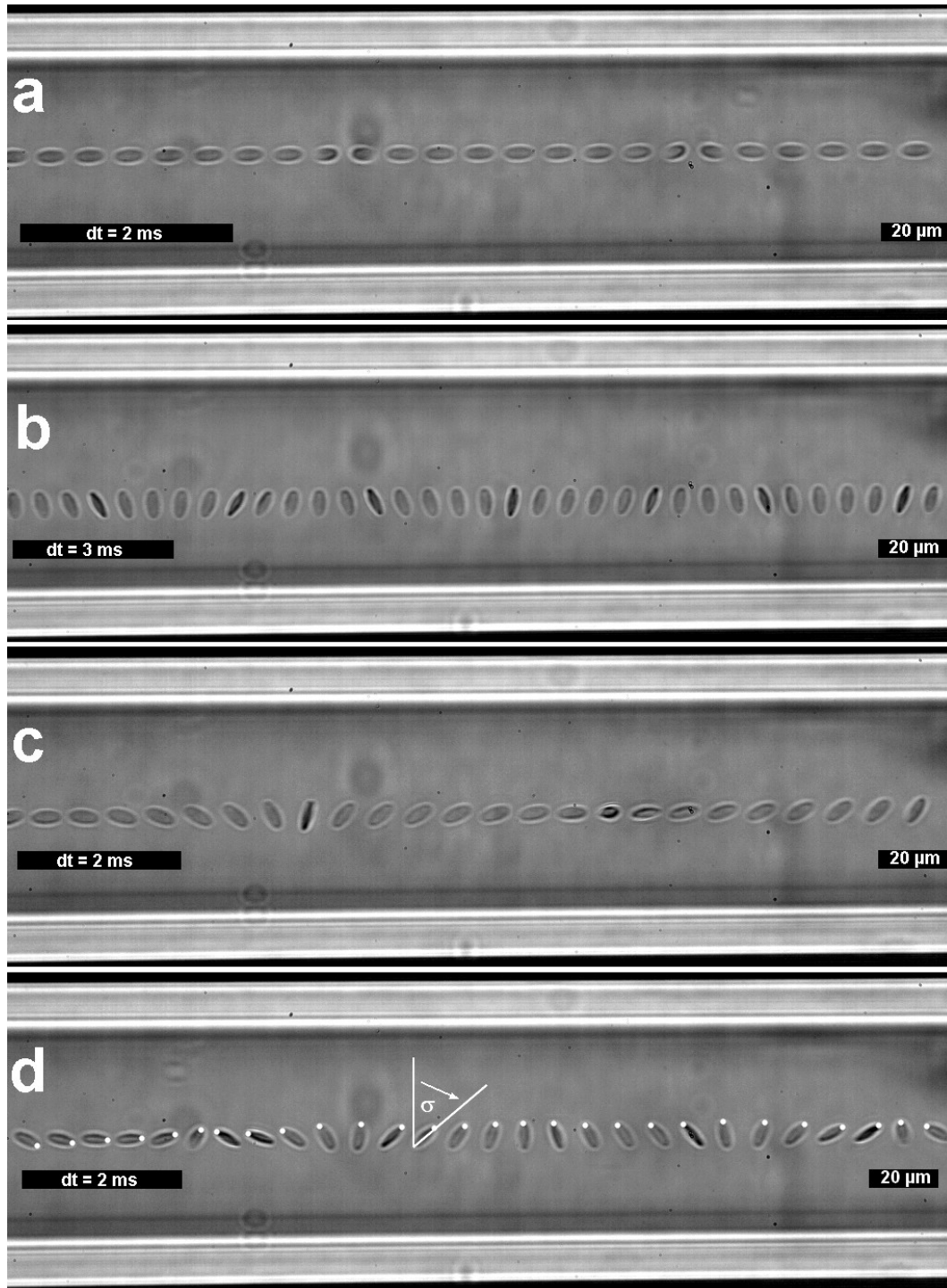
Figure 4.21: Typical flow characteristics of alpaca RBCs at high shear stress in round shaped glass capillaries. The capillary diameter is $2R_{cap} = 60\,\mu$. The images show overlays of recorded high-speed videos. The time step is noted in the corresponding image. Flow direction is from the left to the right. RBCs show a swinging with intermitted tumbling motion. The first image shows the motion viewed from the top and the second image from the side. The flow motion can also have a rotation as the third image shows. The last image shows a RBC with marked cell positions used for accessing the tumbling motion.

0 ° again. For increasing cell velocity, the intermittent tumbling probability decreased slightly and the oscillation of the orientation angle became more stable. In the literature, a comparable flow motion is identified for human RBCs. It is called vacillating breathing or swinging [98, 28, 50, 2]. In figure 4.21 the oscillation of the orientation angle is measured from the top (a) and from the side (b). Sometimes the intermittent tumbling motion also shows a rotation in z-direction (c).

Furthermore, the diameter of the glass capillary was reduced to 20 μm to increase the shear stress for the RBC. Nevertheless, no difference in flow motions was observed. The cells showed the same flow motions as described before.

PDMS Microchannel Experiments
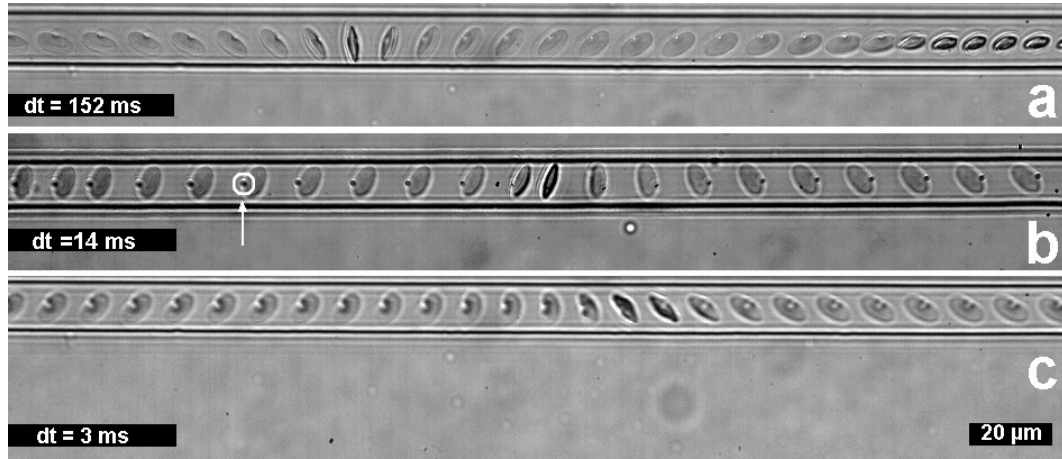
Figure 4.22: Alpaca RBC in square shaped PDMS channels at very high shear stress. The channel diameter is $2R_{cap} =10$ μm. The typical combination of swinging and tumbling can be observed as well in the glass capillary. (a) shows an oscillation and tumbling motion. (b) shows a RBC having a latex bead attached to the RBC membrane that oscillates, too. (c) shows a RBC with the characteristic indentation on the side in the oscillation regime. The overlays demonstrate that the RBC also shows a rotation while the orientation angle is 0 ° in the oscillating regime.

In a next step, the RBC flow behavior in square shaped PDMS microchannels was investigated. As in the glass capillary experiments, cells were added to the inlet of the PDMS microchannel and the cell velocity was controlled by the height-adjustable reservoir connected to the outlet. Figure 4.22 shows a time-stack overlay of an alpaca RBC flowing through the channel of $w = h =10$ μm height and width. At this high shear stress, the flow behavior was an oscillation

around the orientation angle of $\Phi = 0°$ having amplitudes of $\Phi \approx 35°$. In the experiments, the oscillating motion became more and more stable and the cells decreased their intermittent tumbling as the mean cell velocity increased. In addition, we marked a position on the membrane of a RBC by polystyrene latex beads. When the RBCs oscillated around the orientation angle, sometimes they revolved themselves as the orientation angle was $\Phi = 0°$. This behavior was random so that no parameter could be identified.

Discussion

So far only cell deformability of RBCs from camel and lama have been tested in linear shear flow by measuring their diffraction patterns. The studies report that even at shear stresses of $\tau \approx 800\text{N/m}^2$ these RBCs do not deform but orient to the linear shear flow. Here, for the first time, RBCs from alpaca in parabolic flow profiles were measured. Like RBCs from the Camelidae they showed no deformation upon high shear stresses up to $\tau = 320\,\text{N/m}^2$. However, in the experiments the alpaca RBC flow motion exhibited an oscillation of their orientation angle with an intermittent tumbling motion. Until now, this behavior is only known for human RBCs in linear shear flows [2]. Some studies on human RBCs name this motion swinging, vacillating-breathing or trembling. The alpaca RBC flow motion is identified as an intermittent regime between tumbling and tank-treading [75, 172, 136].

In the flow range observed alpaca RBCs do not deform. To understand this behavior even better the next chapter tries to identify the mechanical properties of the cell in more detail. Cells are forced to deform by pushing them through very tiny capillaries where they touched the capillary walls. Their relaxation is observed and the elastic modulus of the unbending process is measured.

4.8.2   Forced Relaxation of Alpaca RBCs

The relaxation experiments were performed in very tiny glass capillaries where the cells touched the inner walls. Then their relaxation after leaving the tiny glass capillaries is observed. For human RBCs the relaxation time was found to be $t = 300\text{ms}$ [41] in a experiment where the cells could relax after an induced deformation. Measuring the relaxation time is a precise method for identifying the viscoelastic mechanical properties of cells. However, there is no relaxation

time measurement for alpaca or camel RBCs in the literature so far because it is difficult to deform them.

Experiments

In shear flow alpaca RBCs did not deform, neither in parabolic (see section 4.8.1) nor in linear [137, 173]. But when the constrictions were much smaller than the dimension of the cell itself, alpaca also deformed to pass through such extreme confinements. Here, the cells from alpaca were squeezed in a tiny glass capillary having a diameter smaller than $2R_{cap} = 2\,\mu\mathrm{m}$. The tip of the capillary was placed in a reservoir and the release of RBCs was observed using the high-speed imaging camera mounted to the inverted microscope. The strong confinement forced the cells to bend at the indentation sides of the cells (see figure 2.10 for indentation sides). Surprisingly, the cells did not orient themselves with the long side parallel to the flow direction. The prolate shape flowed with its long side perpendicular to the flow direction and the strong wall interaction bent the cells (see micrograph in figure 4.23). The squeezed cells then exit into the reservoir with velocities of $v_{RBC} \approx 35\mathrm{mm/s}$. Released from the wall constriction, they could relax back to their initial prolate shape. As well as human RBCs, this demonstrated that red blood cells from alpaca also showed a shape memory effect [47]. The relaxation time was influenced by two major parameters: the drag force of the fluid and the mechanical properties of the cell. The inset of figure 4.23 shows an overlay of a single relaxation experiment at five different times. The graph in figure 4.23 shows the measurement of the bending angle Φ in dependency of the time. The angle was identified between the indentation sides which is always the center of the cell projection and the bent cell parts. In the diagram, the data points are mean values of 10 single experiments. Angles relax from a initial value of $\Phi \approx 74\,^\circ$ to a maximum observable value of $\Phi = 168\,^\circ$. Outside of the field of view the cells fully relaxed. The relaxation behavior is fitted by an exponential fit:

$$\Phi(t) = A\exp(-\frac{t}{t_0}) + B \qquad (4.5)$$

A and B are constants and t_0 is the relaxation time. The time is determined

to be t=1.03 ms $\pm$ 0.10x10^{-4} ms.

With the help of the relaxation time, the bending modulus of the entire Alpaca cell can be estimated. Evans identified a correlation of the relaxation time τ_b and a bending modulus κ for the shape recovery [41]. τ_b is correlated by

$$\kappa \approx (\frac{\eta_f l}{\Delta c^2})/\tau_b \qquad (4.6)$$

In this equation η_f is the viscosity of the surrounding medium (η_f=1mPas), l the length of the cell ($l \approx$8μm) and c the curvature of the fold. In the experiments, the curvature was determined by fitting a circle to the bending point (see inset figure 4.23 at time t1) and was around t1=1.119 μm^{-1}. Consequently, the bending modulus was found to be κ=62.1·10^{-19} J $\pm$ 6.97·10^{-19} J.
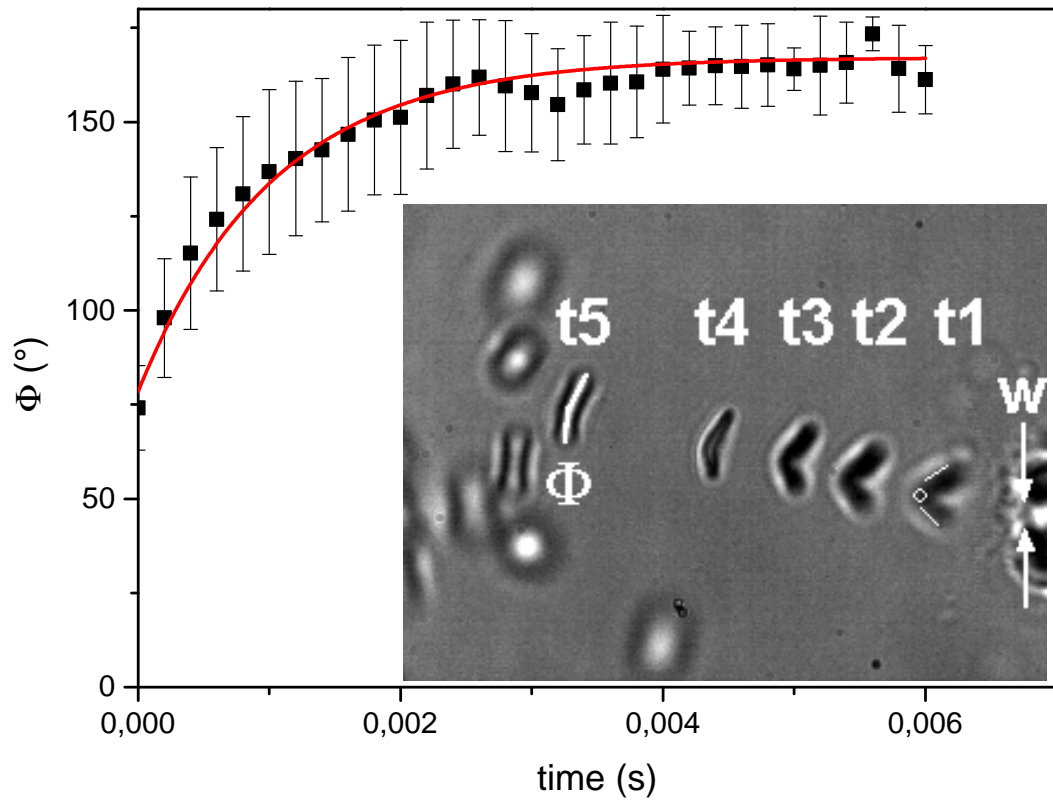
Figure 4.23: Black squares show the mean deformation angle in dependency of the time. The bending angle Φ relaxes from its maximum value of around 74° to its rest and maximum value of 168°. The red line is an exponential fit that reveals a time constant of $1.03\,\text{ms} \pm 0.10\text{x}10^{-4}\,\text{ms}$. The inset shows an overlay of 5 micrographs of a typical measurement (t1=0 ms, t2=0.12 ms, t3=0.32 ms, t4=0.72 ms and t5=2.36 ms).

Discussion

The only way to deform the stiff RBCs from alpaca was to externally force the alpaca RBCs to bend through extreme constrictions while flowing through a very tiny capillary having a diameter smaller than $2R_{cap} = 2\,\mu m$. While they were exiting of this capillary into a reservoir, as described in the experimental part, they were relaxing from a bent shape back to their original shape. The cell bending occurred always at the indentation sides of the alpaca RBC. In general, two important facts can be learned from the relaxation experiment. First, the cells also show a shape memory effect as they relax back to their initial shape equally to human RBCs [47]. Second, the relaxation process allows the calculation of the mechanical properties. So far, comparable experiments have only been performed on human RBCs. Evans found the relaxation time for human RBCs to be $t = 300\,ms$ [41]. Detailed measurements identified the relaxation time in the range of $162\,ms$ (young cells) to $353\,ms$ (old cells) or $271\,ms$ for the whole population [19]. However, alpaca RBCs relax much faster in about $\tau_b = 1.03\,ms$. The short relaxation time already implies dramatically increased stiffness. A bending modulus of $\kappa = 62.1 \cdot 10^{-19}\,J \pm 6.97 \cdot 10^{-19}\,J$ can be calculated using the relaxation time. Flickering spectroscopy measurements on human and camel RBCs showed that the membrane viscosity and the bending modulus of camels are increased by a factor of twenty and four, respectively [173]. In contrast, a 30 times higher bending modulus was identified for RBCs from alpaca.

In the experiments, the determination of the bending modulus depends critically on the curvature determination. The bending curvature of the cell was identified by fitting a circle to the bent part at the middle of the cell (see circle in figure 4.23). Assuming the complete cell was bent (see figure 4.23 at a time of t1) the approximated bending modulus increased to $\kappa = 12.4 \cdot 10^{-17}\,J$, an even higher modulus.

In the literature Evans also added the viscous dissipation ($\nu = 3\eta_m h^2$) to the bending of the membrane for his approximation. As the membrane viscosity was very complicated to be measured and no values for alpaca could be found we neglected this viscous part. In any case, it increased the bending modulus only slightly as the membrane thickness was very thin ($h = 34\,nm$ [12, 56, 86]).

To summarize, the high increase of the bending modulus fits perfectly to the altered molecular structure as described above. The increased content of

band3 [94] yields a highly cross-linked cytoskeleton so that the deformation of the cytoskeleton is reduced and mechanical properties increase [92].

4.9 Cell Orientation in Curved Channels

The cardiovascular system of mammals is a closed network of small capillaries and larger vessels. The heart pumps the blood into the large blood vessels (aorta). From these vessels, the network branches out in capillaries and further in even smaller capillaries having a diameter as small as $2R_{cap} = 2\,\mu\text{m}$. In y-branches the RBC undergoes a sudden change in shear stress and flow direction or in the pulmonary capillary network which is a geometrically complex and vastly interconnected network [64]. A typical blood cell encounters 40 to 100 segments in passing from arteriole to venule [34, 62, 63, 139, 64]. Generally, the red cells traverse the lung in a few seconds [114, 64]. However, the detailed flow behavior of RBCs is quite unknown under varying the flow conditions such as in junction or in capillary bends. For this purpose, RBCs are observed flowing around a $90\,°$ corner. This represents a very extreme physiological situation that a RBC may experience in the microvascular.

In contrast to RBCs, the situation for hard spheres or droplets has been studied, Figure 4.24 shows two droplets passing a corner of $90\,°$.
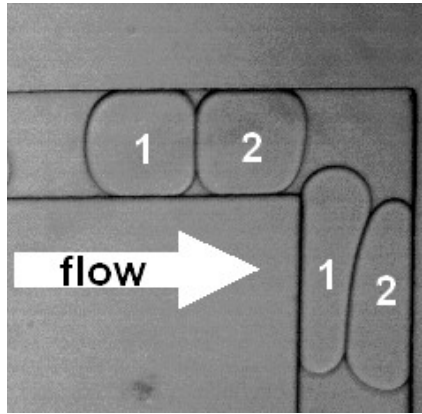
Figure 4.24: Two touching droplets flowing in a PDMS microchannel. The channel has a corner of $90\,°$. The touching interface allows a good identification of the orientation. The droplets pass the corner and keep their orientation irrespectively of the flow direction change.

In figure 4.24, the droplets are in contact with each other, forming an interface that allows the observation of their orientation with respect to the flow

direction. The two droplets pass the corner by keeping their initial orientation, although the flow direction changed by $\Phi = 90°$. In the following experiments the situation for RBCs in corner flow is investigated.

4.9.1 Single Corner Flow Experiment
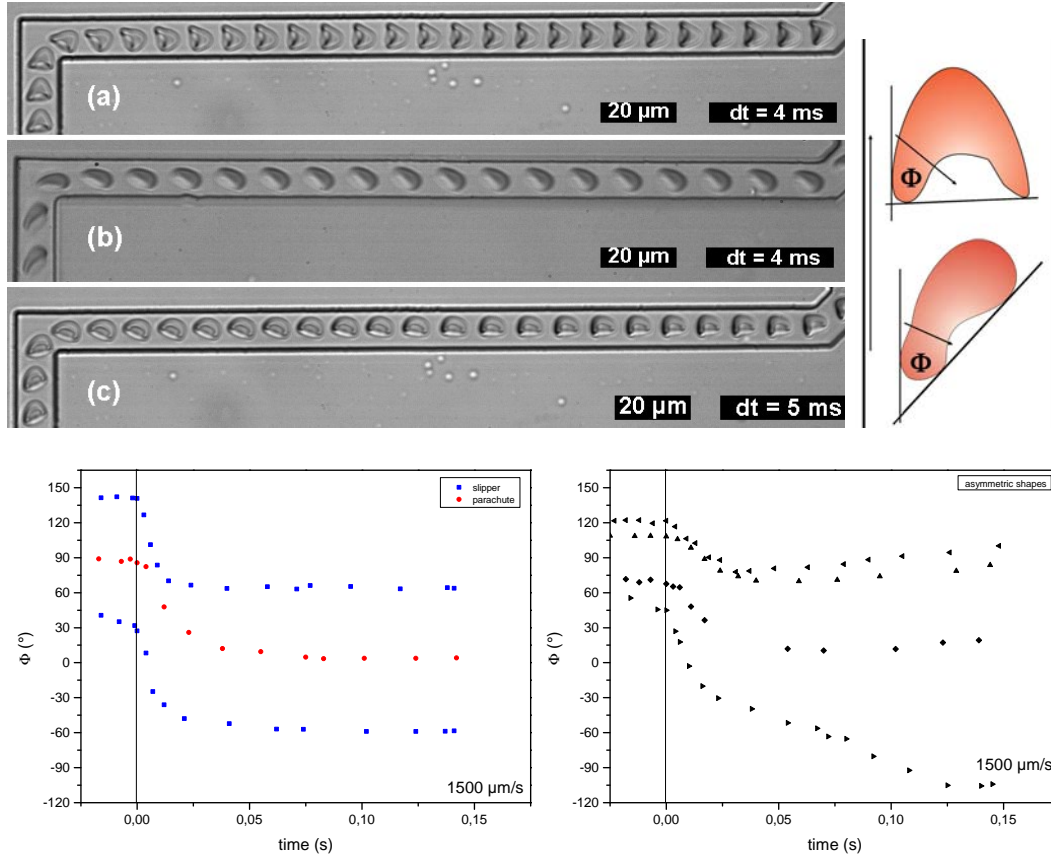
Figure 4.25: (a),(b) and (c) show time-dependent overlays of human RBC flowing in a microchannel of 10 x 10 μm width and height that has a rectangular corner. The orientation angle of slipper and parachute shapes is determined as demonstrated in the scheme. Parachute shapes that adopt $\Phi = 90°$ and slipper shapes that adopt either $\Phi = 45°$ or $\Phi = 135°$ follow the change in flow direction perfectly. In contrast, asymmetric slipper shapes of different orientation angles start to rotate after the flow direction change. Some of them adopt a new shape identified with two dimples. The corresponding measurement of orientation angle in dependency on the time is shown in the bottom row. The left one represents perfectly aligned parachute and slipper shapes and the right one the case for asymmetric shapes of different orientation angle.

Healthy human RBCs were observed in a rectangular PDMS microchannels having a width and height of 10 μm and a corner of exactly 90°. The

PDMS chip was mounted on the inverted light microscope stage and the cells were observed using the high speed imaging camera. Figure 4.25 shows three time-overlays of a single RBC passing a 90° corner. As the orientation angle, with respect to the flow direction, of a flat round shaped discocyte was hard to distinguish, only slippers and parachutes were investigated. The angle with respect to their flow direction was measured, as the schematic drawing in figure 4.25 shows. The parachute shape flowing around the corner is traced in micrograph (a). In the beginning, the parachute shape had taken on a 90° orientation angle and was rotated by $\Phi = 90°$ after the rectangular corner. The left graph in figure 4.25 displays the RBC inclination angle in dependency of time. In contrast to the parachute, the slipper shape adopted either $\Phi = 45°$ or $\Phi = 135°$ and also performed a rotation of 90° due to the corner. However, the right graph in figure 4.25 illustrates the situation of asymmetric slipper shapes that are characterized by orientation angles between $\Phi = 45°$ and $\Phi = 135°$. After the 90° corner, their value of the orientation angle was not decreased by about $\Phi = 90°$ as it was the case for perfectly aligned parachutes or slippers. Asymmetric shapes which had an orientation angle larger than $\Phi = 90°$ performed a left-hand rotation and cells which have an orientation angle smaller than $\Phi = 90°$ performed a right-hand rotation. Additionally, these cells started to adopt a new shape as the micrograph (c) in figure 4.25 shows. The slipper shape did not rotate by $\Phi = 90°$ after the corner as its orientation angle was different to $\Phi = 45°$ or $\Phi = 135°$. Additionally the flow indented a new dimple into the cell. Obviously, inclination angles of $\Phi = 45°$, $\Phi = 90°$ and $\Phi = 135°$ are favorable equilibrium orientations, since cells of this inclination angle follow the flow change perfectly.

4.9.2 Multi Corner Flow Experiment
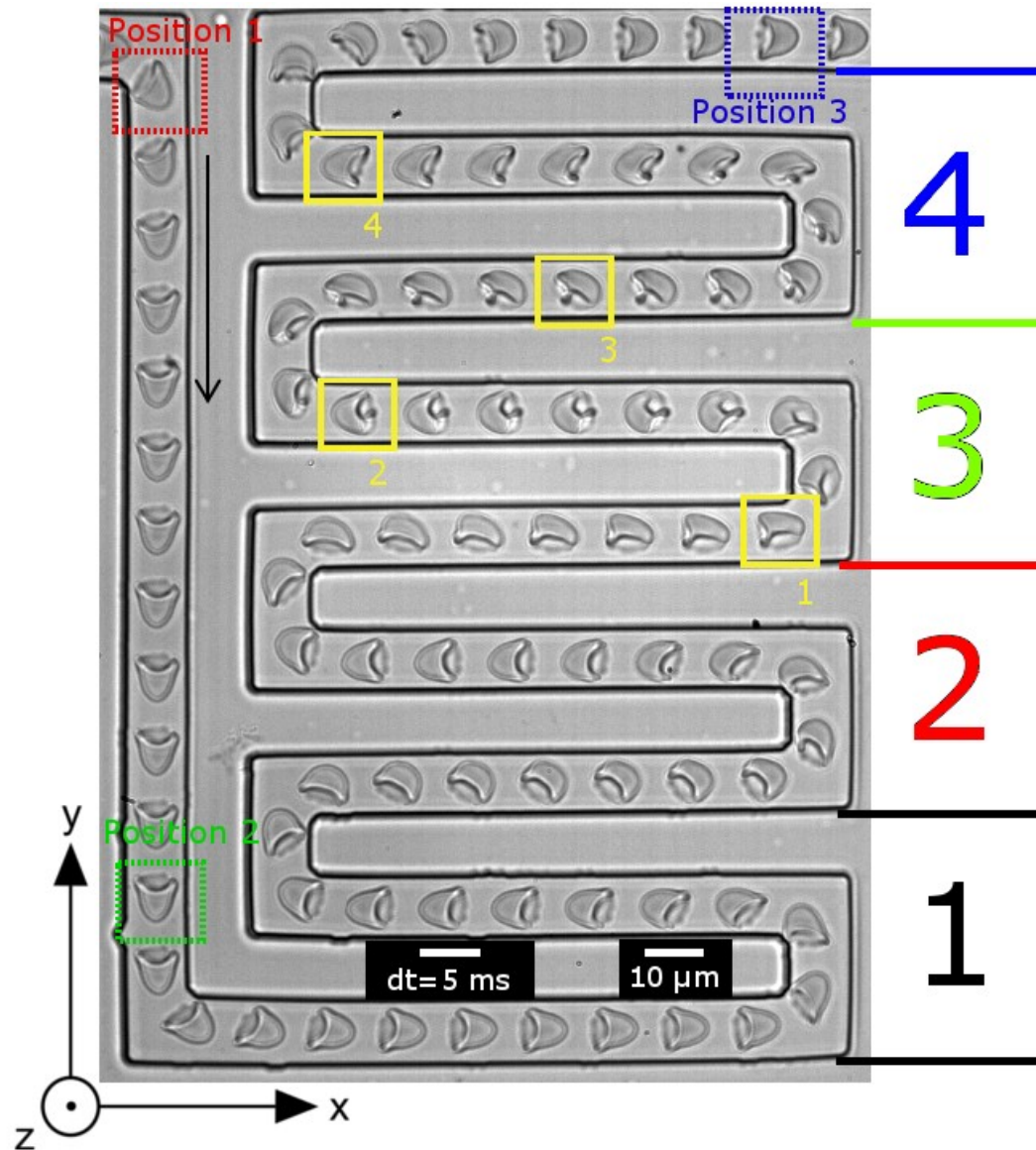
Figure 4.26: The micrograph shows a time dependent overlay of a human RBC at a mean velocity of 2000 μm/s.[8]

---

[8]Experiment is based on work done by Andreas Link jointly with myself.
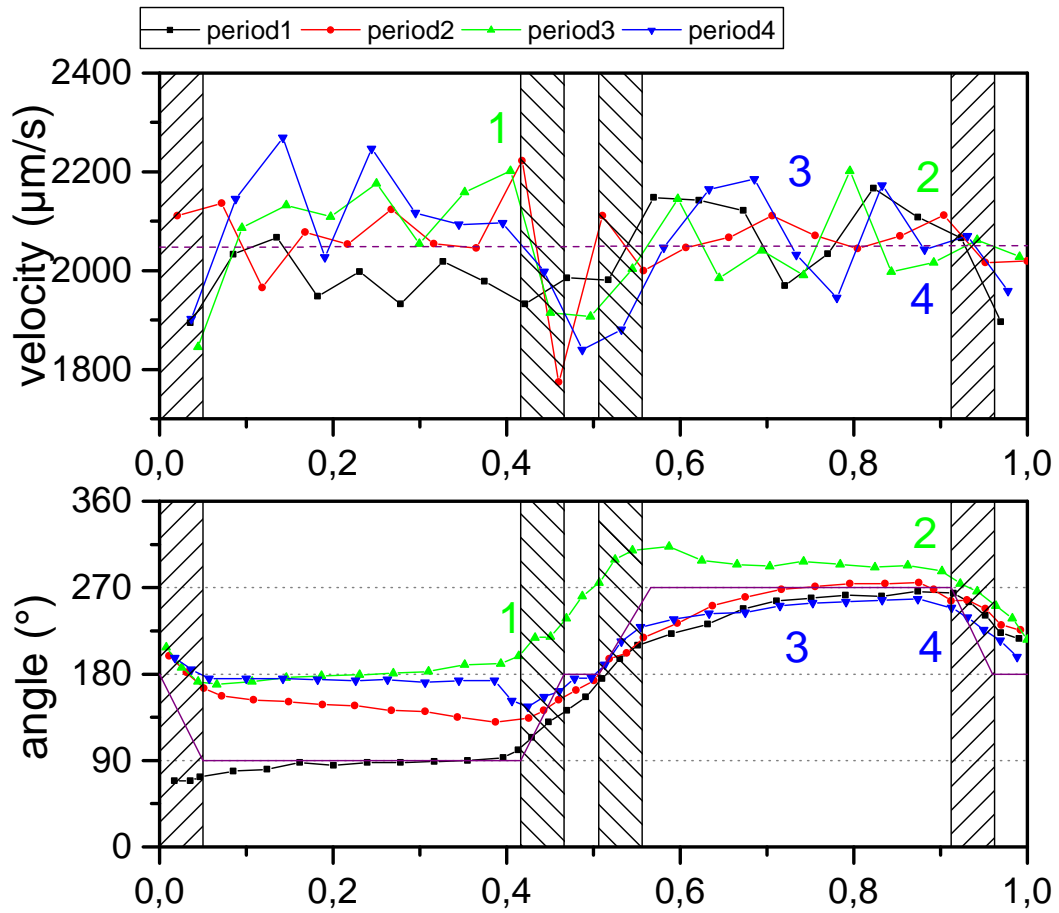
Figure 4.27: Position 1 and Position 2 mark the situation described in the one corner flow experiment. Position 3 marks the final shape that is the same as in the beginning. (1) shows a shape characterized by two dimples (knizocyte). (2) and (3) show that the two dimples tank-tread to the rear of the cell and finally disappear at (4) so that a perfect parachute shape is adopted again. The measurement graph shows the orientation angle with respect to the flow direction and the velocity in the four corner periods.[9]

---

[9]Experiment is based on work done by Andreas Link jointly with myself.

In a next set of experiments, healthy RBCs were investigated in the same channel (width and height are 10 µm) but structured with several periodically aligned rectangular corners (see figure 4.26). At the marks position 1 and position 2 (yellow) the flow situation is comparable to the long relaxation path experiment as described in the previous experiment. Position 3 marks the cell after having passed four periods in which the cells have to flow around 2 rectangular corners with an intermittent relaxation path as the micrograph in figure 4.27 shows. For low shear stress, more explicitly, in the discocyte regime (see section 4.5) the cells pass the corner structure without any shape or velocity changes. In the high shear stress or parachute regime (see section 4.5) the cells always followed the flow directions because their orientation angle was always perpendicular to the flow. In the slipper regime ($250 < v_{RBC} < 2000$ µm/s) the cells adopted asymmetric slipper shapes of varying orientation angles. Since the experiment of only one corner showed orientation angles of $\Phi = 45°$ or $\Phi = 135°$ it was favorable for the asymmetric shapes to follow the flow direction without rotation. However, the shape of the cells was not as constant as for parachute or discocyte shapes. A typical example can be seen in figure 4.27. The mean cell velocity was $v_{RBC} = 2000$ µm/s. In the beginning, the parachute followed the direction change of 90° nicely (position 1 and position 2). The cell then entered the four periods of repeating flow direction changes with intermittent relaxation paths. In period 1, the cell handled the two left-handed (from the cell's point of view) corners as expected. However, in the last corner the orientation angle start was different to 90° with respect to the flow direction. However, in period 2 the orientation angle of the cell got back to $\Phi = 90°$. Again, in the end of period 2 the cell got off-center and showed an orientation angle different to $\Phi = 90°$. In the beginning of period 3 the cell could not compensate for this and the complete parachute was rotated by $\Phi = 90°$. The cell forms a new dimple in the back while the old dimple remains at the bottom of the cell (yellow box (1)). In the literature, this shape is similar to a knizocyte. However, knizocytes have been reported in the litereatur at rest only and have not been observed in flow. In the following the two dimples tank-tread to the rear of the cell. The cell is now characterized by two dimples that are separated by a membrane part (yellow box (2)). At this membrane part, the curvature is very high. In period 4 the two dimples amalgamated as the highly bent membrane part diminishes slowly (yellow box (3)). Interestingly, the cell relaxes back to a parachute shape (yellow box (4))

over a kind of slipper shape. Finally, at position 4 and the end of the left- and right-handed corners, the cell is in the parachute shape again, still showing a small membrane knot in the rear dimple. Additionally, the parachute shape is shorter than it was in the beginning (compare position 2 and 3). In the graphs of figure 4.27, the angle and velocity with respect to the position in each of the four periods is highlighted. Note that the angle was measured with respect to the x-axis of the image and not to the flow direction. Besides the fact that the velocity of the cells decreased in the corners, no correlation of orientation angle and velocity change could be obtained.

4.9.3 Spiral Flow Experiment

The problem in the multi corner experiment was that the orientation relaxation was determined by the straight path after the corners. The flow direction changes in the corners influenced or even stopped the relaxation. Thus, in another experiment, the RBCs were investigated in microchannels structured as a spiral. Figure 4.28 (top) shows the channel design. The channel width and height is again $w = h = 10\,\mu\mathrm{m}$.

From the transition regime point of view, the spiral is very interesting because the relaxation is not influenced by corners which change the flow direction suddenly. Compared to the multi-corner experiment, the cells also adopted a knizocyte shape (see figure 4.28 (top)). The asymmetric slipper shapes entered the first rotation of the spiral and started to transform into knizocytes. Sometimes their protuberances were also rotating around the cell center of mass. This was denoted as the deformation process and the time t_1 was measured. In contrast, the relaxation time t_2 was defined as the time the cell needed to adopt the same slipper shape as in the beginning of the channel structure. For different velocities, the healthy human RBCs tend to show higher deformation times t_1 compared to the relaxation time t_2 so that $\sigma = t_1 - t_2 > 0$. The same experiment performed with RBCs suffering from Spherocytosis showed an opposite behavior. The diseased RBCs showed a decreased deformation time so that $\sigma < 0$.
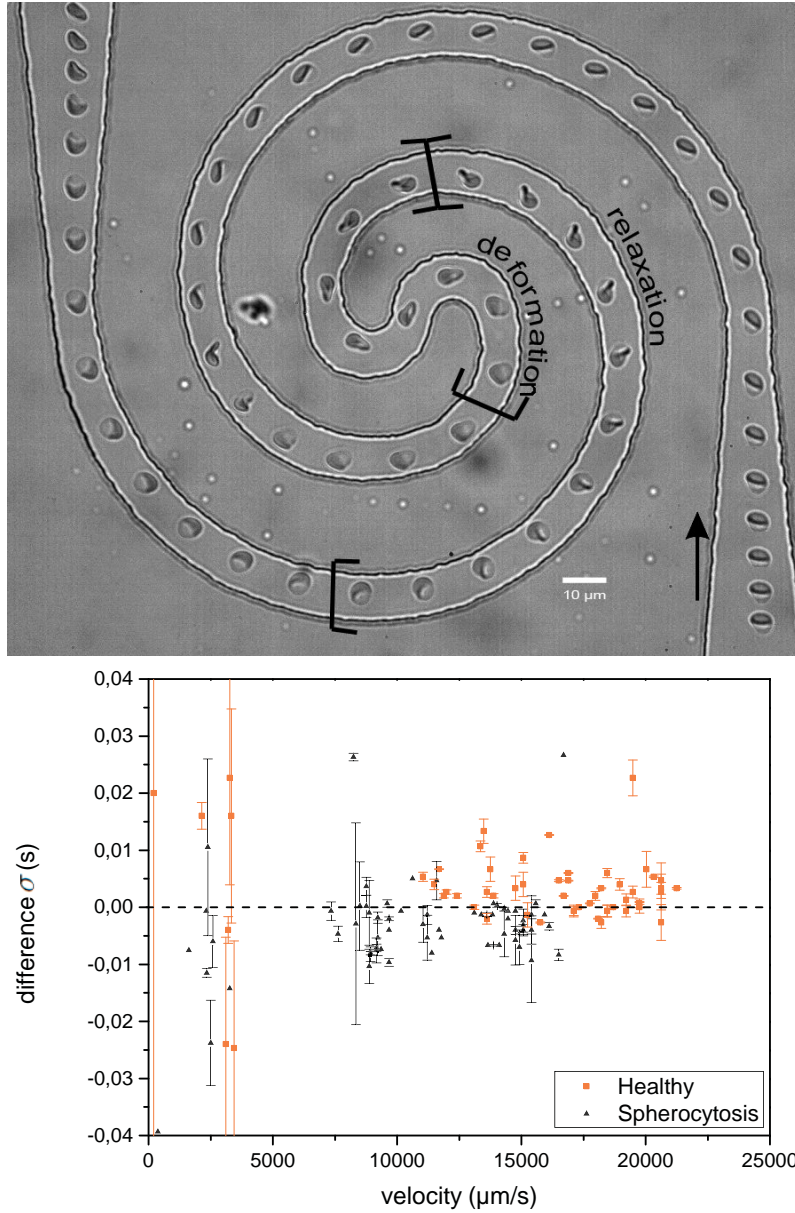
Figure 4.28: PDMS microchannel showing a spiral geometry. After a 360°
rotation, the channel shows a S-shaped turn and another 360° rotation with
opposite rotation direction to the outlet. The width and height of the spiral is
10 x 10 μm. In the transition regime, the asymmetric slipper shapes deform into
knizocytes. The knizocyte shows a rotation as the rear protuberance rotates.
Deformation and relaxation times can be measured (bottom). Healthy RBCs
tend to show higher deformation times compared to the relaxation time (σ>0).
RBC suffering from Spherocytosis show an opposite behavior as σ<0.[10]

---

[10]Experiment is based on work done by Katharina Haase [55] jointly with myself.

4.9.4 The Orientation of RBCs Follows the Flow Direction

The flow orientation of particles in narrow channels is relevant in many fields, ranging from the spinning and molding of fibers to the flow of cells or proteins through thin capillaries [123, 103, 66, 155, 14]. As mentioned in the beginning, droplets pass corners by keeping their original orientation with respect to the flow direction. This effect can be used in winding channels to induce chaotic advection inside the droplet and the inside is mixed [138]. From that point of view, investigations concerning the alignment of RBCs with respect to hemoglobin mixing are highly interesting.

While the RBCs flowed around a rectangular corner, there are some favorable orientation angles that hinder a rotation after the sudden flow direction change. The orientation angles were measured in the rear of the cell with respect to the flow direction. Parachutes show orientation angles of $\Phi = 90°$ and follow the dictated flow direction change perfectly. The same situation appears for slipper shapes that have orientation angles of either $\Phi = 45°$ or $\Phi = 135°$.

Kaoui et al. [76] suppose that the slipper and parachute shape facilitate the oxygen transport efficiency. Further, they suggest that the membrane tank-treads in order to efficiently mix the hemoglobin, and thus enhance oxygen distribution in tissues. The measurements in section 4.7 regarding the transport efficiency and tank-treading occurrence of the shape transitions support this assumption.

The pulmonary capillary is part of a complex organ and shows vessel curvatures down to $C = 5\,\mu m^{-1}$ [163, 34, 62, 63, 139, 64, 114]. There oxygen diffuses into the RBCs on time-scales smaller than $1\,s$ [114, 64]. It would seem reasonable that tank-treading mixes the hemoglobin and increases oxygen uptake. In that sense the stable orientation angles of the slipper shape are reasonable. The same is true for orientation angles different than the stable ones, because these cells try to adopt a slipper shape where the tank-treading frequency is highest. But why is the parachute shape also stabilized when this shape is not able to tank-tread? The measurement of the parachute shapes in the multi-corner channel showed that even the parachute shape did not follow the flow direction changes, at least for physiological shear stress. After some corners, the parachutes adopted a new shape, called knizocyte, that was able to tank-tread due to the asymmetry.

The cells were investigated in a spiral. For healthy RBCs, the same orientation behavior was observed as in the multi-corner experiment. However, the deformation process and relaxation process of knizocytes could be investigated even better because the turn was only one smooth curve. Healthy RBCs showed longer deformation times than relaxation times.

4.10   Rapid Deformation Response

Viscoelastic material behavior, as RBCs depict, is featured by fluid and solid characteristics upon deformation. A deformation is elastic and relaxes viscously. It is time-, temperature- and frequency-dependent. This section tries to clarify the frequency modulated deformation behavior of the cells and tries to identify the viscoelastic properties of the RBC.

In a theoretical and experimental study [105] vesicles were investigated while flowing in microchannels, in which the width varied periodically along the channels. The channel walls or the modulation followed a sawtooth function. The vesicles transformed from a state with orientational oscillations of a fixed prolate shape to a state with shape oscillations of symmetrical ellipsoidal or bullet-like shapes with increasing flow velocity. In addition, the shape oscillation showed a phase shift. Recently, Braunmüller et al. [16] studied the deformation of RBCs in microchannels of oscillating-width. RBCs were deformed in a sine modulated microchannel. They found that RBCs transformed from a flow motion having the inclination angle oscillated to a non-oscillating motion showing a deformed shape only. Up to modulation frequencies of 454 Hz, RBCs showed an inclination angle that started to oscillate. At higher modulations, the RBCs stopped inclination angle oscillations but showed an oscillation of cell deformation. In their experiments, sine modulated channels and modulation frequencies from 400 to 1000 Hz were used. In the following experiments, RBCs are investigated at modulations frequencies from 0 to 1500 Hz using sawtooth modulated microchannels and SAW microfluidics.

4.10.1   Deformation of RBCs in Structured PDMS Microchannels

The freshly prepared RBCs were pipetted into the inlet of the channel and the outlet was connected to a height-adjustable reservoir. The height difference

between the reservoir height and the microscope stage defined the pressure gradient along the channel and controlled the velocity of the RBC suspension by this means. Using the high speed camera that was mounted onto the microscope the RBCs flowing through the microchannel were observed in the middle of the channel. The channel had a zigzag structure which can be seen in the inset of figure 4.30. The channel width decreases by $2R_{cap} = 13\,\mu$m quadratically over the entire channel length. This ensured a linear velocity increase along the complete structure. In every period, the wide part was $\Delta 2R_{cap} = 10\,\mu$m larger than the narrow part. The structure allowed the observation of an oscillating deformation at various velocities simultaneously.

Using ImageJ software, the shape of the cells were tracked and their length l and height h were measured. The deformation parameter was calculated by $1 - ((l - h)/(l + h))$ so that an increasing deformation value corresponded to a cell relaxation. Figure 4.29 (top) shows such a typical tracking of a RBC for low velocities. When the RBCs flowed through the channel, height L_y decreases and the mean cell velocity increases. In the same fashion the maximum deformation of the cells increases. Similar to an elastic material, the maximum deformation of RBCs does not occur in the middle of the period but is slightly shifted to the end of the period. This phenomenon is highlighted in figure 4.29 (bottom). All deformations are plotted in one graph and a sine is fitted. In the first half of the period, the deformation increases because the cell can relax in the flow direction, while in the second half of the period the cell is deformed again because it reaches the narrow part of the next period. The sine fit reveals a phase shift of $\alpha \approx 7\,\%$ or $25.2\,°$.
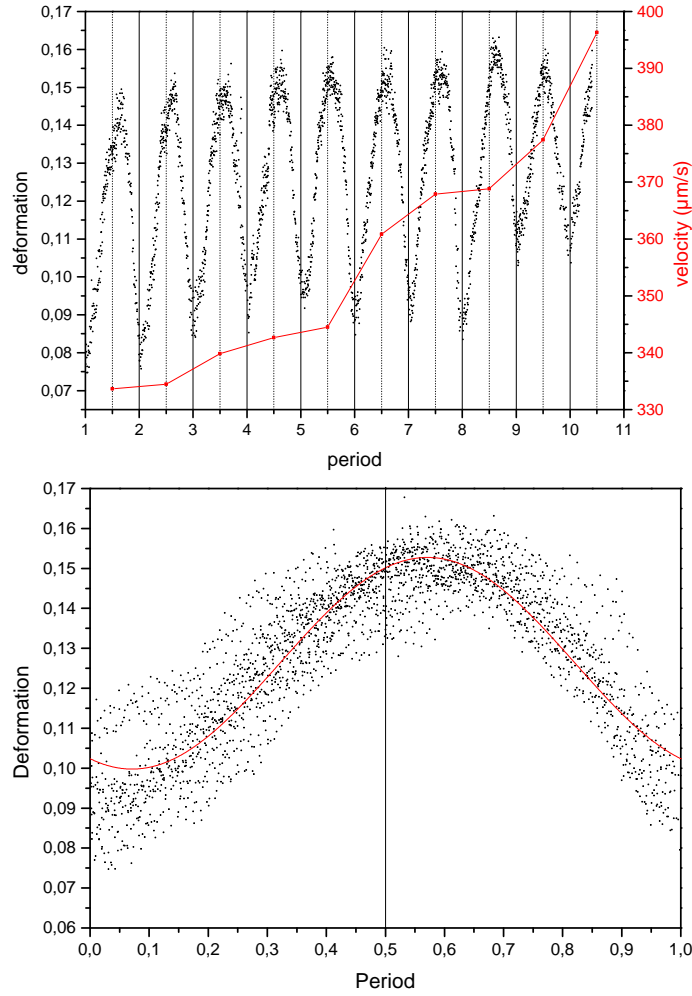
Figure 4.29: (top)1-Taylor deformation $(1-((l-h)/(l+h)))$ of a single RBC in a zig-zag modulated microchannel. The deformation in each period oscillates sinusoidally with a phase shift of $\alpha = 25.2°$ with respect to the microchannel. The microchannel shows a parabolic decreasing channel width so that the mean cell velocity (red line) increases linearly. (bottom) Overlay of all deformations in the zig-zag modulated channel. The red line is a sine fit to determine the phase shift of $\alpha = 25.2°$.

Figure 4.30 (1) shows a typical measurement at a higher velocity of $v_{RBC} \approx$ 2600 µm/s. Here, the two measured cell dimensions l_x and l_y (height and width) are normalized by the period height L_y and are plotted against their position in a single period. In period (1) marked in the inset, the cell is deformed as it enters the period and relaxes in the middle of the period, with a typical phase shift. This behavior changes in the period (5). The deformation does not follow a sine function and no phase shift can be observed because the sine data fit can no longer be applied. Furthermore, the data points scatter more. In the following periods, the RBC deformation stays chaotic or changes in opposite sense, it is relaxed and shows an increased deformation in the wide part of the period. This is shown in figure 4.30 (11). This critical point is identified as occurring at velocities of $v_{RBC} \approx$ 3000 µm/s and $L_y \approx$ 15 µm at modulation frequencies of $f \approx$ 200 Hz.

Noguchi et al. [105] predict a reduced bending rigidity by

$$\kappa^* = \frac{\kappa L_y}{\eta R_v^3 v_m} = \frac{L_y}{v_m \tau} \tag{4.7}$$

Accordingly, the reduced bending rigidity κ^* is found to be $\kappa^* =$ 0.05 for relaxation times of $\tau =$ 0.1 s [17].
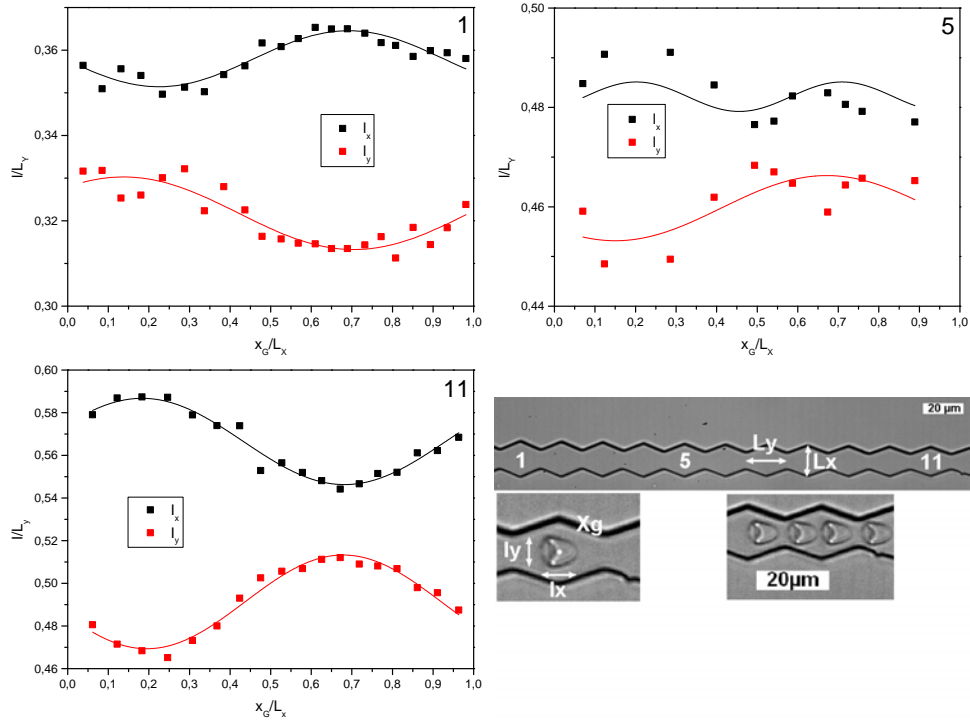
Figure 4.30: The graphs show the length and width change of healthy human RBCs that flow through a zigzag modulated microchannel. The micrograph shows the complete structure of the channel. The characteristic cell deformation for three different periods (1), (5) and (11) is demonstrated. The average RBC velocity in the period amounts to $v_{RBC} =2700$ for the first, $v_{RBC} =3000$ for the fifth and $v_{RBC} =3300\,\mu m/s$ for the eleventh period. The deformation shows a phase shift. This phase shift inverts for mean cell velocities of $v_{RBC} =3000\,\mu m/s$.

4.10.2 Deformation of RBCs of SAW
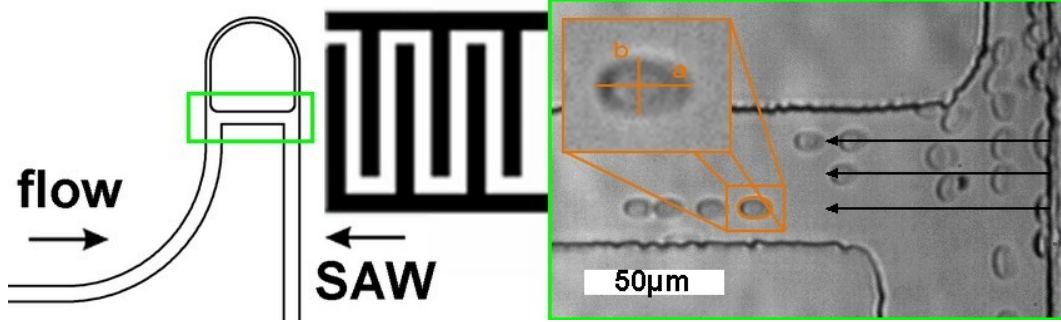
Figure 4.31: Schematic drawing of the SAW modulated deformation experiment. RBCs are flowing from the left to the right driven by a hydrostatic pressure. In the straight part (R_{cap} =50 µm) of the D channel structure the cell is coupled into the channel in opposite flow direction. The wave length of the SAW is between λ =23 and λ =24.5 µm. The black arrows indicate the alignment paths when the SAW is turned on. Taylor deformation is used to describe the oscillating motion of the RBCs [55].

In the following, the RBCs were deformed by coupling a SAW into a microchannel facing the opposite direction to the flow direction. This was achieved by pressing the PDMS with the channel structure strongly onto a carrier using two spring clamps. The carrier held a lithium niobate LiNbO$_3$ plate, that was transparent, with the IDT assembled on top of it. It was important that the channel was aligned perfectly to ensure good coupling (see figure 4.31 and section 2.3.4). After having the channel prepared, it could be filled with PBS-BSA solution (see methods). RBCs were pipetted to the inlet reservoir and the outlet was connected to a height-adjustable reservoir. It was then lowered and a constant cell velocity was adjusted. Using the high speed imaging camera that was mounted on the inverted microscope, the green framed area in figure 4.31 was recorded. As the SAW was turned on, the cells align at the three minimum nodes (black arrows) of the resulting standing waves. In addition to their aligning they were deformed in the SAW direction. The SAW power controlled the deformation. In general, the experiments showed that with increasing SAW power the deformation increased. However, experiments using three different SAW powers of Q =17 dB, Q =22 dB and Q =25 dB showed that the best results were produced by a SAW power of Q =22 dB. These were the best in terms of measurable cell deformation and cell viability since high SAW power thermally destroyed the cells and less power resulted in a

decreased deformation. In a next step, the amplitude of the SAW power was modulated by a sine function and the deformation was measured by the Taylor deformation $D = (a - b)/(a + b)$ (see figure 4.31).

The deformation was fitted using a sine fit. In that way, the deformation could directly be compared to the coupled modulation frequency of the SAW. Figure 4.32 shows the fitted frequency f_g normalized by the modulated frequency f_m in dependency of the modulated frequency. Since the RBCs are not able to follow the modulation at some point f_g/f_m decreases to $f_g/f_m = 0$. This marks the resonance frequency of the cells f_0. In the SAW modulated experiments healthy and chemically modified RBCs were tested. Healthy RBCs were found to follow the modulation frequency up to $f = 200\,\mathrm{Hz}$. Chemical modification allowed the cells to follow the forced deformation even for higher frequencies. Formaline modified RBCs could not follow the modulation at frequencies of $f = 560$ and $f = 820\,\mathrm{Hz}$ for low and high modification respectively. Diamide modifications could be excited until frequencies of $f = 690\,\mathrm{Hz}$ and $f = 1180\,\mathrm{Hz}$ for low and high concentrations respectively. RBCs suffering from Spherocytosis were in the same range as healthy RBCs and followed the forced deformation until a frequency of $f = 210\,\mathrm{Hz}$.

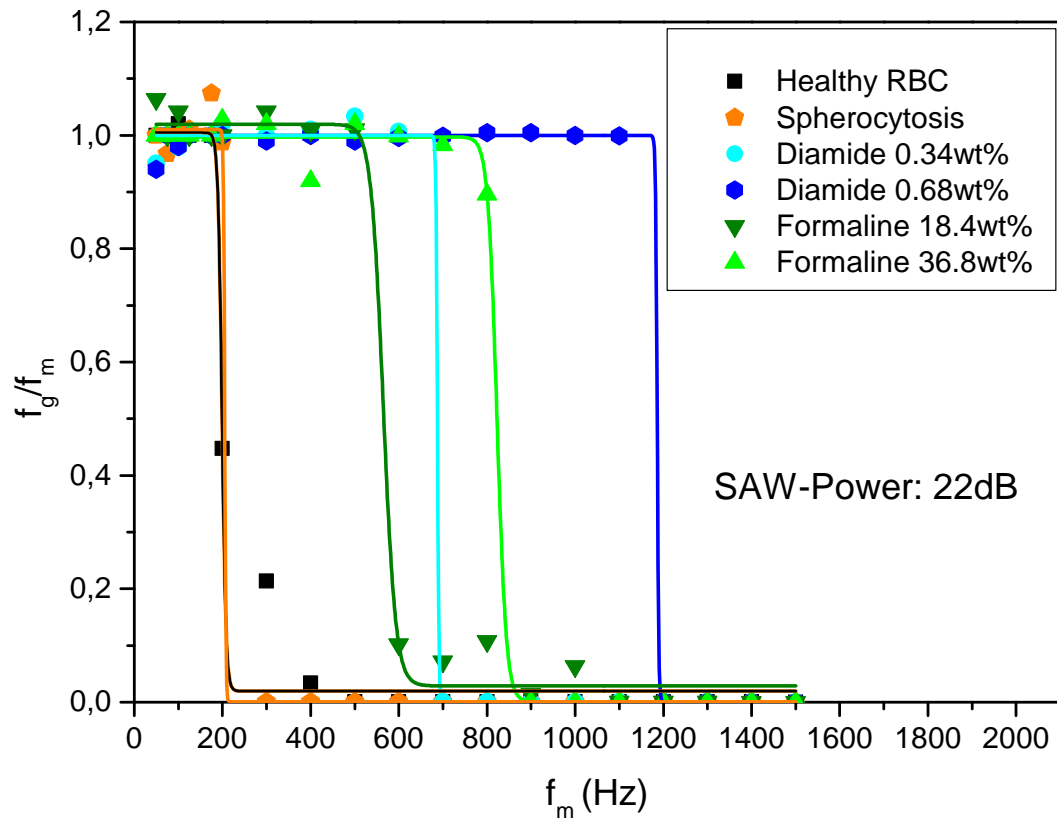Figure 4.32: RBC oscillation frequency f_g normalized by the modulation frequency f_m in dependency of the modulation frequency. The SAW power is 22 dB. Chemical modified RBC sustain higher oscillating deformations than healthy RBCs. RBCs suffering from Spherocytosis are in the same region as healthy RBCs.[11]

---

[11]Experiment is based on work done by Katharina Haase [55] jointly with myself.

4.10.3 Discussion

Recently, Noguchi et al. [105] and Braunmüller et al. [16] reported a phase shift in the induced deformation behavior of RBCs and vesicles while flowing through structured microchannels. Braunmüller et al. studied the dynamics of RBCs in hydrodynamic flow fields determined by a sine-modulated microchannel of varying channel width. The RBCs showed a transition from a regime with oscillating tilt angle and fixed shape to a regime with oscillating shape with increasing flow velocity. They observed the crossover to occur at a modulated frequency of $f =$454 Hz. The oscillation showed a phase shift of $\alpha \approx$44 ° half the value Noguchi et al. simulated ($\alpha \approx$72 °) for vesicles in a zig-zag modulated deformation. Braunmüller et al. reported that the oscillations were superposed by shape transitions from a discocyte to a slipper shape at low velocities and a slipper to parachute transition at high flow velocities.

In the previous section, the deformation of RBCs in a zig-zag modulated microchannel showed no regime of oscillating tilt angle for modulation frequencies of 15 Hz to 300 Hz. A possible reason for the difference could be a different modulation structure of the channel. Obviously, zig-zag modulations affected the cell deformation differently than sine modulations. However, in the experiments, the oscillating deformation behavior changed for a frequency of $f \approx$200 Hz. Furthermore, the phase shift of the oscillating deformation was only $\alpha =$25.2 °.

Quite a few materials behave in such a way that they have a combination of viscous and elastic responses under deformation. Accordingly, RBCs are known to show a viscoelastic behavior upon deformation. These materials can be characterized by a Maxwell material that is a combination of an elastic part described by the Hooke's Law and a viscous part described by Newton's Law. The two components can be expressed by a spring and a dashpot in the equivalent circuit diagram. The Hooke's Law describes the stress σ as a modulus G times the strain γ and the Newton's Law describes the stress σ as the viscosity constant η times the shear rate $\dot{\gamma}$. The elastic mechanical element shows the force (stress) behavior to be proportional to the strain and the viscous mechanical element shows the force to be proportional to the strain rate. Viscoelastic materials show both kinds of behavior upon deformation [95]. Consequently, their material response is time-dependent. In oscillatory rheology the time dependency can be used to identify mechanical constants.

For a viscoelastic material, the stress strain relation is given by [95]

$$\sigma(\omega t) = G'\gamma_0 \cdot \sin(\omega t) + G''\gamma_0 \cdot \cos(\omega t) \qquad (4.8)$$

$$\text{with} \quad \eta = \frac{G''}{\omega} \quad \text{and} \quad \tan(\delta) = \frac{G''}{G'} \qquad (4.9)$$

In the equations ω is the angular modulation frequency, t is the time, G' is the storage modulus, G'' is the loss modulus and γ_0 corresponds to the strain amplitude. Consequently, using the measured phase shift of $\alpha = 25.2°$ and the effective viscosity η_{eff} of $\eta_{\text{eff}} = 81\,\text{mPas}$ [11] the storage and the loss modulus for healthy RBC are found to be $G' = 102\,\text{Pa}$ and $G'' = 216\,\text{Pa}$. The moduli are three orders of magnitude smaller than the elastic constant found by atomic force microscopy. This is mainly related to the fact that in the previous experiments the cells are in the parachute shape and that the whole cell is measured. In the IT-AFM technique, the cell measurement is very localized. However, a more detailed study [18] on the nano-rheology behavior of RBCs using AFM reported a time-independent elastic modulus of $\mu = 4.0\,\text{mPa}$ at low levels of deformation. Furthermore they observed time-dependent elastic moduli ranges of $\mu = 35\,\text{kPa}$ to $\mu = 55\,\text{kPa}$ at intermediate levels of deformation and $\mu = 150\,\text{kPa}$ to $\mu = 300\,\text{kPa}$ at higher levels of deformation.

So far, the advantages of microstructured channels of oscillating width have been highlighted. However, finding the resonant frequency of single RBCs in these channels has some disadvantages (e.g. cell clogging in narrow constrictions or the fixed modulation frequency determined by the channel structure). SAW microfluidics mitigates some of these disadvantages. In the experiment, a SAW is coupled into the D-structure in opposite flow direction. Since the strength of the flow is much stronger than the SAW power, the flow is only slightly affected. In the channel the SAW is reflected by the channel walls and the cells align on the zero amplitude positions of the resulting standing wave. At this point, future research has to be performed to clarify the SAW coupling situations. Nevertheless, the modulation of the SAW amplitude allows a fast scanning of the deformation frequency and deformation level. Note that the deformation level or the SAW power is very dependent on the respective distance to the IDT. However, the cells were able to deform in the zero amplitude position of a sine modulated SAW. The results are summarized in table 4.5.

The corresponding storage modulus G' is calculated using an effective vis-

Cell Type	f_0 (Hz)	G' (Pa)	$G''_{25.2^\circ}$ (Pa)	G''_{79° (Pa)
Healthy	196	99.7	212	103
Spherocytosis	205	104	222	108
Diamide (0.34 wt%)	690	351	746	364
Diamide (0.68 wt%)	1180	601	1276	622
Formaline (18.4 wt%)	560	285	606	295
Formaline (36.8 wt%)	820	417	887	432

Table 4.5: Resonant frequencies f_0 of single RBCs modulated deformation experiment.

cosity η_{eff}=81 mPas [11]. Alterations in the cell membrane may increase the membrane viscosity and thus the effective viscosity. However the membrane thickness is around 30 nm, so that the effect on a comparably large sphere is assumed to be negligible. The effective viscosity depends linearly on the external viscosity η_{ext}. Betz et al. [11] as well as other studies [27] find the RBC viscosity to be in the order of η =0.01 mPas. In the case of the loss modulus G'' two different phase shifts are used: α =25.2° as found in the zig-zag modulated channels and α =79° as in the sine modulated channels. Future improvements would be measuring SAW modulation. Triggering the video capture together with the modulation signal would have allowed an even more precise measurement of the phase shift compared to the structured microchannels. Nevertheless, the mentioned phase shifts are in between α =0° (corresponding to a purely elastic material) and α =90° (corresponding to a purely fluid material) indicating a viscoelastic material behavior. Consequently, the loss modulus values are only an estimation for the range of the material parameter.

Again, chemical modification shifts the resonance frequency to higher values. Regarding the cytoskeleton as a network of springs, a higher resonance frequency f_0 corresponds to a higher spring constant k_{spr} ($f_0 = 1/(2\pi)\sqrt{k_{spr}/m}$) because the mass m of the erythrocyte remains constantly at m =27 picograms [112]. The effect of cross-linking across the spectrin polymers (formaline) shows a minor effect compared to the effect of cross-linking inside the spectrin (diamide). This is consistent with the findings of the IT-AFM and MPA measurements as well as the deformation and shape transformation observations in the microfluidic devices. In contrast, the resonance frequency of RBCs suffering from Spherocytosis shows only a slight increase compared to healthy RBCs.

Chapter 5

Conclusion

The results reported in this thesis link the RBC shape transition or cell deformation of flowing RBCs to their physiology and pathologies. In the following the shape transition from a discocyte to a parachute shape is discussed regarding the single results of the measurements described in the section before.

As a first result in section 4.7 it was shown that the shape change lowers the flow resistance. In tiny capillaries, RBCs of mammals change their typical biconcave discoid rest shape upon increasing shear stress to asymmetric slipper shapes or axisymmetric parachute shapes. Both slipper and parachute shapes lower the flow resistance as their slip velocity increases. The slip velocity is defined as the velocity difference between the mean RBC velocity and the theoretical velocity of the fluid without cells. In the experiments (see section 4.7), the mean cell velocity of the slipper shape is slightly increased compared to the theoretical fluid velocity. The parachute shape shows an even higher increase in mean cell velocity. This is in a good agreement with previous studies. Sutera et al. [142] reported that the velocity ratio was equivalent to the hematocrit discharge. In their study, the hematocrit ratio decreased with increasing fluid velocity or shape. In other words, by changing the shape the cell velocity increases faster relative to the suspending fluid velocity. This has been confirmed experimentally by Tomaiuolo et al. [153], recently. This correlation supports the assumption of Kaoui et al. [75] that the shape transformation of RBCs to slipper or parachute shapes decreases flow resistance.

In the following the second important result, the tank-treading of the RBC membrane, is discussed. During shape transformation the tank-treading motion of the RBC membrane is possible mainly by asymmetry which is caused

by a cell position which is off-center or an asymmetric shape (slipper). Unfortunately, in the tapered capillary experiments (see section 4.6) where RBC transformed from a discocyte shape to a slipper and further parachute shape, no tank-treading could be observed because the latex beads attached to the RBC membrane clotted the capillary. Nevertheless, it was possible to observe RBCs with membrane markers (latex beads) in capillaries of 50 μm (see section 4.7). In this case, the off-centered flowing cells adopted slipper shapes and showed tank-treading of the membrane. Kaoui et al. [75] assume that the tank-treading motion has an important physiological impact: mixing the cytosol especially in narrow capillaries. Additionally, the phase diagram of healthy RBCs (see figure 4.15 in section 4.6) supports this assumption. For flow conditions such as in very narrow capillaries of the microvasculatur the slipper probability is increased. For very small capillaries ($2R_{cap} <4$ μm) the RBCs had contact to the wall and slipper shapes were preferred for mean cell velocities up to 1000 μm/s. These flow conditions are of great relevance, since they are found in the narrow network of the the microvascular network consisting of venules (diameter: $2R =20.6$ μm), arterioles (diameter: $2R =13.2$μm) and capillaries (diameter: $2R=8.72$ μm) [113, 116] and average blood velocities of 1070 μm/s, 2030 μm/s and 850 μm/s, respectively [116, 8]. Especially in the lungs this physiological aspects are important. There, the shape transition decreases flow resistance and increases hemoglobin mixing to increase oxygen uptake.

The measurements in the corner and multi-corner flow experiment (see section 4.9) support the hypothesis even stronger. There, similar curvatures as in the pulmonary capillary were simulated. Interestingly, the parachute shape deformed into a knizocyte. This shape is able to tank-tread and thus increase homogeneous oxygen uptake of the cells. In the literature this shape is not reported for flowing RBC so far. This shape was measured in the spiral flow measurements (see section 4.9.3) only for very high velocities ($v_{RBC} > 3000$ μm/s). It is supposed to be induced by asymmetric flow conditions (off-center flow). From a physiological point of view this shape is very unlikely to occur in the microvasculatur because there are no corners or such high velocities as in the reported experiments. The knizocyte may thus be seen as an artificial shape which occurs only in experiments as described.

However, an important question arises now. Why do the cells change their shape at all and do not keep their slipper or parachute shape all the time? In

the following the results from the measurements try to answered this critical point.

First, the most obvious reason is that membranes in aqueous solutions with volume to surface ratios of $\nu=0.592$ to $\nu=0.651\,\mu$m adopt a biconcave discoid shape (see section 2.2) [57, 144, 130]. Unlike vesicles, RBCs have an in-plane shear elasticity dictated by the cytoskeleton which contributes to the shape formation as well. The discocytic rest shape of a RBC is the result of minimizing bending energies of the membrane and neglecting fluctuations (see section 2.1.1).

Second, aged cells are separated and recycled in the human body [161]. During their lifetime the cells deform in the narrow capillaries of the microvascular reversibly. As a consequence the deformability decreases. After 120 days, mechanical properties are altered and the aged cells rupture in the micropores of the spleen [71]. Regarding the curvatures of the shapes the assumption that shape transformation induces mechanical stress is supported. In flow, the healthy RBC shows a front curvature change of $\Delta C_f^{disco}=0.229\,\mu$m^{-1} upon changing the shape from a discocyte to a parachute (see section 4.4). Compared to the typical front curvature of $C_f^{disco}=0.265\,\mu$m^{-1} for the rest shape the transformation to a parachute corresponds to a curvature change of around 80 %. This indicates already the enormous stress RBCs have to withstand.

Third, RBCs show a unique membrane structure compared to normal cells. The membrane of a RBC is a composite architecture made of a lipid-protein bilayer and a cytoskeleton anchored to the lipid membrane. The cytoskeleton provides stability to the membrane and is composed of a hexagonal spectrin-actin polymer network. The membrane-associated network is composed of semi-flexible spectrin filaments that form a triangular lattice. The sides consist of tetramers of spectrin that are formed by head-to-tail coupling of hetero-dimers (α-spectrin and β-spectrin) [122, 101]. The interplay of the lipid membrane and the cytoskeleton provides the viscoelastic properties of the cell envelope and ensures a reversible response to external stress [122]. The resistance to shear deformation is mainly given by the cytoskeleton because of the fluid character of the lipid membrane. However, the lipid membrane dictates bending response [59, 43, 61]. Performing MPA measurements a value for the cell shear modulus of $\mu = 6.80 \pm 1.4\,\mu$N/m was found. This value is in excellent agreement with literature values using MPA [61, 39]. The bending modulus was measured by IT-AFM. The results for healthy RBCs yield a value of

κ=4.8·10^{-19} J which is also in good agreement with values reported for different techniques [80, 46, 29, 40, 56, 141, 21, 124, 54].

These findings are true for healthy human RBCs or all other mammals (only small variations in cell scales) because the discocytic RBC is the common case. As described in section 2.1.4 and section 4.8.2 there is one exception: RBCs of the camel family show unique RBC shape in the class of mammals. The RBC of Camelidae such as alpacas, camels, guanacos and vicunas adopt a prolate shape. Using ESEM-imaging, the alpaca RBC dimension was identified by a length of $l \approx 7\,\mu$m, a width of $w \approx 4\,\mu$m and a thickness of $h \approx 1\,\mu$m (see section 2.1.4). Omorphos et al. [108] confirmed the flattened ellipsoid shape by SEM-imaginging, too. In comparison to human RBCs, the cells are known to have a reduced volume to surface ratio of ν=0.667. This is below the discocyte regime (ν =0.592 to ν =0.651) and the spontaneous curvature model would predict an elliptic prolate shape. From a physiological point of view, the elliptical shape of alpaca RBCs may be very useful. Their regular habitat are deserts or high altitudes. Exposed to chronic hypoxia or dehydration, as is the case in the mentioned extreme environments, they need less cardiorespiratory adjustments compared to any other mammal. For example, dehydration would lower the water pressure inside the cell and thus the volume. In means of a discocyte, the large osmotic change would decrease the volume to surface ratio leading to a shape change described by the spontaneous curvature model. Such a shape change is accompanied by high mechanical stresses. Obviously, a prolate shape is favorable because it is more stable over a broader range of volume to surface ratios.

Another point regarding the shape of alpaca RBCs is the architecture of the cell membrane. The red cell of Camelidae also has a lipid bilayer with an underlying cytoskeleton as well as the RBCs from other mammals (it is anchored by proteins like ankyrin and band3 underneath the lipid bilayer). In the experiments, a mean cell density increase of 3 % was measured (see appendix A.11). This may be an indication of an increased hemoglobin content in the cytosol of the cells. The hemoglobin content is also known to affect the membrane and thus the shape configuration [171]. An effect that is known from human RBCs suffering from β-Thalassemia [73]. However, McPherson et al. [94] concluded that the degree of the cytoskeleton crosslinking was increased due to a higher content of the protein band3. Other studies on lamas or camels support the result: the high protein to lipid ratio of 9 to 1 stabilizes

the membrane and the elliptical shape strongly [77].

Next, the non-deformable shape and flow motion of RBC from alpaca in the mentioned flow devices is discussed. In ESEM images two opposing indentations in the middle of the cell were observed (see section 2.1.4). These indentations were as deep as 342±20 nm. However, squeezing the cells through an extremely thin capillary ($2R_{cap}$ <2 μm) allows cell bending at the indentation (see section 4.8.2) despite their increased mechanical stability. The indentations are supposed to enable the bending of the cell. Nevertheless, the cell shows a 30 times higher bending modulus of κ =62.1·10^{-19} J compared to human RBCs. The increased bending modulus of the alpaca RBCs also has an effect on the flow behavior of the cells. From other studies observing the RBCs of camel and lama in flow by measuring their diffraction patterns, it is known that the cells do not deform but orient in linear shear flow even at high shear stress up to $\tau \approx$ 800 N/m^2. The experiments described in section 4.8.1 validate this for RBCs from alpaca in parabolic flow profiles and corresponding shear stress up to τ =320 N/m^2. At low shear stress, the cells tumble randomly as human RBCs do. Additionally, with increasing mean cell velocity an oscillating flow motion can be observed. The cells oscillate around their orientation angle with an intermittent tumbling motion. This behavior is only known for human RBCs in linear shear flow [2]. Some theoretical studies on human RBCs call this motion swinging, vacillating-breathing or trembling and identify it as an intermittent regime between tumbling and tank-treading [75, 172, 136].

The cell motion of the alpaca RBCs may be explained by the inhibited tank-treading motion of the membrane due to the increased bending modulus. The membrane is a two-dimensional structure and tank-treading motion induces constant shear and bending. An increased bending modulus also reduces shearing of the membrane and inhibited the tank-treading motion of the membrane.

The alpaca RBC system is a nice example that highlights the relevance of studying the rigidity of RBCs with respect to the physiological requirements. Studying the effects of chemicals to the human RBC associated with an alteration on the dynamics of RBCs will improve the understanding of blood flow. Additionally, modifying the RBC membrane chemically mimics blood diseases or hematological disorders and provides new insight which is relevant to the design of medical therapeutics. To provide a link between the molecular structure and the macroscopic elastic properties of the composite membrane

we selectively introduced mechano-effective agents (see section 2.1.3). These chemical modifications of the cell membrane are motivated by real blood diseases. They can be used as model cells to mimic several blood diseases (see section 2.1.2). In several diseases such as Spherocytosis or elliptocytosis, a deficiency or dysfunction of main membrane proteins such as spectrin or proteins that were involved in cytoskeleton linking was observed. In the spring model this directly translates into a variation in spring constant.

In the following the influence of the single chemical modifications are summarized and discussed.

	κ (J)	μ (N/m)	B (N/m)
native	4.80 E-19	6.80 ± 1.4 E-06	31 ± 1.7 E-06
formaline (18.4 wt%)	6.59 E-19	7.60 ± 2.4 E-06	32 ± 2.6 E-06
formaline (36.8 wt%)	6.99 E-19	3.40 ± 0.2 E-05	28 ± 2.0 E-06
diamide (0.34 wt%)	5.33 E-19	1.25 ± 0.3 E-04	34 ± 2.2 E-05
diamide (0.68 wt%)	9.74E-19	1.85 ± 0.3 E-04	27 ± 2.1 E-05

Table 5.1: Summarized results of the MPA and IT-AFM measurements.

First the influence of the chemical formaline is disussed. The bending modulus κ was only increased by about 50% for both concentrations (see section 4.2). While for low formaline concentrations the shear modulus μ was slightly increased, higher concentrations increased μ about a factor of 10. Parameter B for the high pressure regime of MPA increased less than 10% for formaline comparing to healthy cells. Formaline introduced CH_2-groups between amino-acids in the cytoskeleton but is also known to cross-link hemoglobin [102, 72]. To minimize the latter effect and unspecific cross-linking of other amino-acids the incubation time ($t < 10$ min) was kept short and low formaline concentrations were used. In experiments not discussed here, long incubation times and high formaline concentrations showed non-deformable RBCs in the flow experiments. Therefore, the dominant effect of formaline is to introduce cross-links between α- and β-spectrin. In a simple model, the spectrin tetramer is characterized by a spring constant [33, 12] and cross-links between the α- and β-spectrin of a dimer. This type of cross-link does not affect the spring constant of the tetramer and explains the minor effect of formaline on B and μ.

Second, the effect of diamide is explained. The reducing agent formed cross-links inside the cysteine of the spectrin [49, 71, 24] and thereby reduced the stretch induced unfolding of the tetramer. The change of κ was up to 100%

for the high concentration treatment. The impact on the shear modulus and B was even bigger. B varied in the order of one magnitude and the shear modulus even in the order of two magnitudes. In the spring model this leads to an increase of the spring constant and explained the pronounced effect on B and μ as evident from table 5.1.

Third, modifying the cells by enriching or depleting the cholesterol concentration in the lipid bilayer was quite different from the cell modification with formaline or diamide. This modification affected the cytoskeleton indirectly. As the lipid membrane area was changed an initial tension was applied to the cytoskeleton. In the flow experiments, this could be seen by the decreased transition velocities v_c and v_c^*. The initial tension applied to the spectrin tetramers allowed a premature unfolding, so that slipper and parachute shapes were observed for lower shear stress compared to healthy RBCs. The situation was reversed for cholesterol depletion. There the cells needed additional shear stress to transit from the discocyte into the slipper or parachute shape.

Fourth, the effect of different salt concentrations of the buffer is discussed. The conjecture of the initial load to the spectrin polymers is supported by the fact that RBCs exposed to buffers of different tonicity showed similar effects. In the case of a hypotonic buffer, the inner cell pressure increased and applied an initial load to the skeleton so that the transition velocities were decreased. In contrast, a hypertonic buffer decreases the inner cell pressure and require an even higher shear stress to deform into slippers or parachutes.

It is now possible to connect dynamically measured deformation parameters to statically measured mechanical moduli for the first time because the same preparation techniques and blood donors were used. The dependency of μ and κ on the deformation parameter was depicted. Figure 5.1 (top) shows the behavior of the normalized bending modulus and the normalized shear modulus in dependency of the maximum length ratio (b/a). The maximum length ratio was observed in the PDMS microchannel at a velocitiy of $v_{RBC} = 3500\,\mu\text{m/s}$ (see chapter 4.4). The graph clearly shows that native human RBC are highly deformable at small bending and shearing modulus (square symbols). The chemical modifications exhibit at higher values of μ and κ a decreased cell deformability (note: cell deformation parameter decreases from left to right). In the literature, Noguchi and Gompper [104] simulated elastic and fluid vesicles in a parachute-like shape. They calculated the behavior of the length ratio b/a in dependency of normalized κ (their range is from $\kappa = 0.2 \cdot 10^{-19}\,\text{J}$ to $\kappa = 1.8$
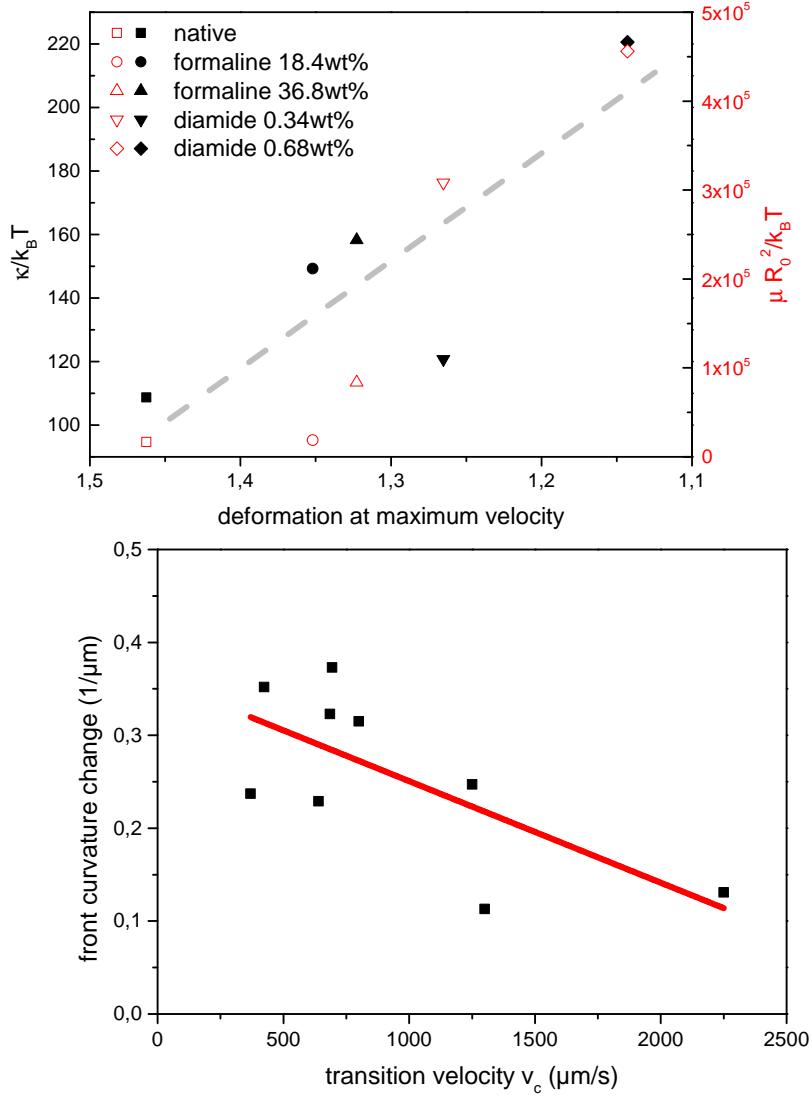
Figure 5.1: (top) normalized bending modulus and shear modulus in dependency on measured deformation b/a at maximum velocities of $v_{RBC} = 3500\,\mu\text{m/s}$ in the 10x10 µm PDMS Microchannel. The dashed grey line is a visual aid indicating the lowered deformability upon increasing bending and shear modulus. (bottom) front curvature change of all measured RBC modifications in dependency on their transition velocity from discocyte to parachute v_c.

$\cdot 10^{-19}$ J). Their calculations are for a fixed μ of $mu \approx 0.04\,\mu$N/m in a round shaped capillary (diameter of $2R_{cap} =10\,\mu$m) and a velocity of $v_{RBC} =47\,\mu$m/s. They concluded a deformation parameter change of $D =1.2$ to $D=1.0$ by increasing the bending modulus for their model cell. The decrease is supposed to be linear.

This cannot be directly translated to the values measured in this thesis because the shear modulus of human RBC is larger than in the theoretical calculation for elastic and fluid vesicles. Additionally, the measured cells were observed for even higher velocities ($v_{RBC} =0\,\mu$m/s to $v_{RBC} =3000\,\mu$m/s). To summarize, their observation regime is slightly different. Nevertheless, the introduced chemical modifications of RBCs allow a comparison to their prediction. The prediction says that with increasing bending modulus the deformation decreases (for a fixed shear modulus). A linear behavior can be confirmed experimentally. The behavior is indicated by the dashed visual aid. However, the chemical modification affects both the bending and the shearing modulus as mentioned (note that the bending modulus was less influenced by formaline and diamide modifications than the shear modulus).

Figure 5.1 (bottom) shows the dependency of the front curvature change in dependency of the transition velocity from discocytes to parachutes in the PDMS microchannel. As mentioned the front curvature is correlated to the bending and the shearing of the membrane (see section 4.4). The graph highlights the fact that an increased transition velocity is strongly correlated to membrane curvatures and thus the membrane bending and shearing. Additionally, an increased number of cross-links in the cytoskeleton lowers the membrane curvature and consequently increases the transition velocity.

The cells were also deformed by coupling SAW into a PDMS microchannel (see section 4.10.2). These measurements leave room for improvement. By sweeping the modulation frequency of the SAW amplitude, the measurement was able to identify the resonant frequency of the whole cell. Future experiments that synchronize the phase between modulation signal and video signal will also allow the determination of the phase shift, another important parameter describing the viscoelasticity of RBCs.

Appendix A

Appendix

A.1 SU-8 Master Production

In the following the master production of the channel mold is described. The single steps follow the data sheet instructions for the negative photo resist SU-8 2-25 provided by MicroChem LINK!. The following instruction is for a master production having a final height of $10\,\mu$m. For different heights replace corresponding values of the data sheet with values marked as variable.

- Cut the silicon wafer that are used as substrates for the photo resist in pieces of 5 x 5 cm

- Clean the pieces properly using acetone and then isopropyl alcohol

- Put a cleaned piece on the chuck of the spin coater

- Be sure that the piece is aligned symmetrically to avoid vibrations during the further processes.

- Turn on the vacuum to have the peace fixed to the chuck

- Program the spin coater as described in table A.1

Step	Spin Speed (rpm)	Time (s)	Ramp (rpm/s)
1	500	5	100
2	500	5	0
3	3000 (variable)	30	0

Table A.1: Spin Coater Parameters for a final resist height of $10\,\mu$m. The first steps are always the same independently on the resist type. Depending on the desired final height choose a different resist and final Spin Speed (see data sheet).

- Close the lid and make a test run

- Add around 2 ml of photo resist on top of the piece and start the spin coater again

- Transfer the spin coated substrate to a petri dish on the hotplate having a temperature of 70 °C. Note: Be sure that the petri dish is already heated

- Wait 2 min (variable)

- Transfer the petri dish to the oven having a temperature of 100 °C.

- Wait 5 min (variable)

- Let the coated substrate cool down slowly and prepare the mask aligner in the meantime

- Use scotch tape or depression to adhere the foil or chrome mask respectively to the mask holder

- Transfer the coated substrate to the drawer of the Mask Aligner MJB3 (Carl Süss, Garching)

- Align the substrate to control the position of the future channel structure

- Contact the sample with the mask

- Set the exposure time to 10 s (variable)

- Start the exposure

- Separate the sample from the mask

- Transfer the coated and exposed substrate to the petri dish on the hotplate having a temperature of 70 °C. Note: Be sure that the petri dish is already heated

- Wait 1 min (variable)

- Transfer the coated and exposed substrate to the oven having a temperature of 100 °C.

- Wait 2 min (variable)

- Let the coated and exposed substrate cool down slowly and fill up a petri dish with developer mr-dev 600 (MicroChem Corp., Newton)

- Develop the master in the petri dish by slowly pivoting the dish for 2 min (variable)

- Clean the master with isopropyl alcohol

A.2 PDMS Channel Production

In this part, the PDMS micro-channel construction is described. Cut the hardened PDMS that is on top of the master out using a scalpel. Then punch holes in the in- and outlets of the channel structure with a punch. Then, take the cut PDMS pieces having the channel structure stamped to the ground and some glass slides to the clean room.

- Clean the PDMS parts in an ultrasonic bath in a tube containing isopropyl alcohol for 10 min

- Dry the parts with nitrogen

- Clean the side containing the channel structure with scotch tape

- Ensure that there is no dirt particle in the channel structure using the light microscope or otherwise repeat the steps before

- Clean the glass slides using acetone and then isopropyl alcohol

- Place both glass slide and PDMS channel in the plasma cleaner

- Wait until the vacuum reached around 23 mTorr

- Flush the chamber with oxygen

- Set the time for the plasma to 12 s

- Start the plasma

- Pump the chamber for 10 s

- Ventilate the chamber

- Put the PDMS on top of the glass slide with little pressure

A.3 Glass Capillary Fabrication for Flow Experiments

This appendix deals with the production of glass capillaries for RBC observation

- Clamp a glass capillary into the micro pipette puller P-97 (Sutter Instruments, Novato)

- Program the micro pipette puller with the following parameters of table A.2

Parameter	Value
Heat	794
Pressure	80
Velocity	70
Delay	80

Table A.2: Parameters for small tapered glass capillaries

- Press run

- Remove the two glass capillaries having the desired structure

- Assemble the capillary to the micro forge

- Align the tip of the capillary close to the glass bead from top to down

- Press the heating foot switch to adhere the glass bead to the capillary

- Hit the table once so that the shock brakes the capillary at the position where the glass bead is adhered to the capillary

A.4 Micro Pipette Aspiration Capillary Fabrication

In the following the production of glass capillaries for micro pipette aspiration is described in detail. The capillaries should have a very small opening diameter (less than $2\,\mu m$ to increase the accuracy of the determination of the elastic constants.

- Clamp a glass capillary into the micro pipette puller P-97 (Sutter Instruments, Novato)

- Program the micro pipette puller as the parameters are given in table A.3

Parameter	Value
Heat	810
Pressure	150
Velocity	150
Delay	120

Table A.3: Parameters for capillaries having a very tiny capillary opening and a parallel tip.

- Press run

- Remove the two glass capillaries having the desired structure

- Assemble the capillary to the micro forge

- Align the capillary from the left so that the opening of the tip is directly in front of the glass bead

- Press the heating foot switch shortly and take care to not adhere the glass bead to the capillary

- Repeat the last step a few times so that the tip is polished and not as sharp as in the beginning

A.5 RBC Separation from Whole Blood

In this section the RBC separation from the whole blood is described in detail.

- Adjust pH of a fresh PBS (140 mM NaCl, 10 mM KCl and 6.4 mM $Na_2HPO_4 \cdot 2H_2O$) buffer (without Ca and Mg) to 7.4 by adding NaOH or HCl to decrease it or increase it respectively

- Add 3 ml PBS to a 15 ml tube

- Add 1 ml of whole blood to the tube

- Centrifuge the tube

- Remove all the liquid on top of the sedimented red fluid (RBCs) with the pipette

  The last two steps should be repeated two times minimum to ensure a clean solution of containing only RBCs and PBS.

A.6 Size Effect of Cholesterol Incubated RBC

This experiment was performed to investigate the size effect of cholesterol modification of healthy human RBC. The figure A.1 shows the projected 2-D cell area in the microscope of enriched and depleted RBCs.
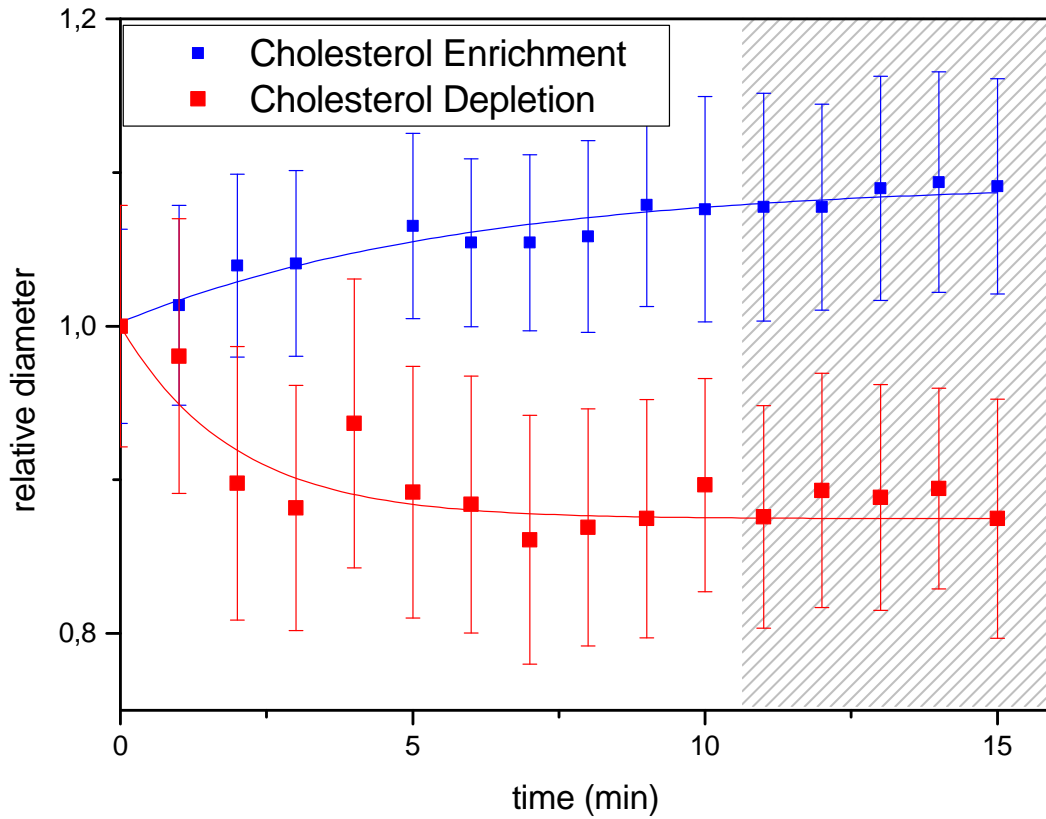
Figure A.1: Size effect of RBC for Cholesterol Enrichment (a) and Depletion (b)[1]

The measurement shows that incubation times longer than 10 min do not change the shape. However longer incubations showed cell lysis and an increased number of stomatocytes or echinocytes. Thus the incubation was set to 10 min to keep the cells vital.

A.7   Size Effect of Spherocytosis

RBCs suffering from spherocytosis are known to show a decreased volume to surface ratio due to the release of microvesicles. Thus the measurement of the cell size is interesting. Figure A.2 shows the projected 2-D cell area in the microscope in dependency of different velocities. Of course cells change their shape upon increasing shear stress. However, the cell areas are compared to healthy RBCs. The measurement shows that the cells are smaller by about 30%.

---

[1]Experiment is based on work done by Kerstin Wittmann jointly with myself. Wittmann, Kerstin: Cholesterol-modifizierte rote Blutkörperchen im Mikrofluss. Universität Augsburg, 2011.
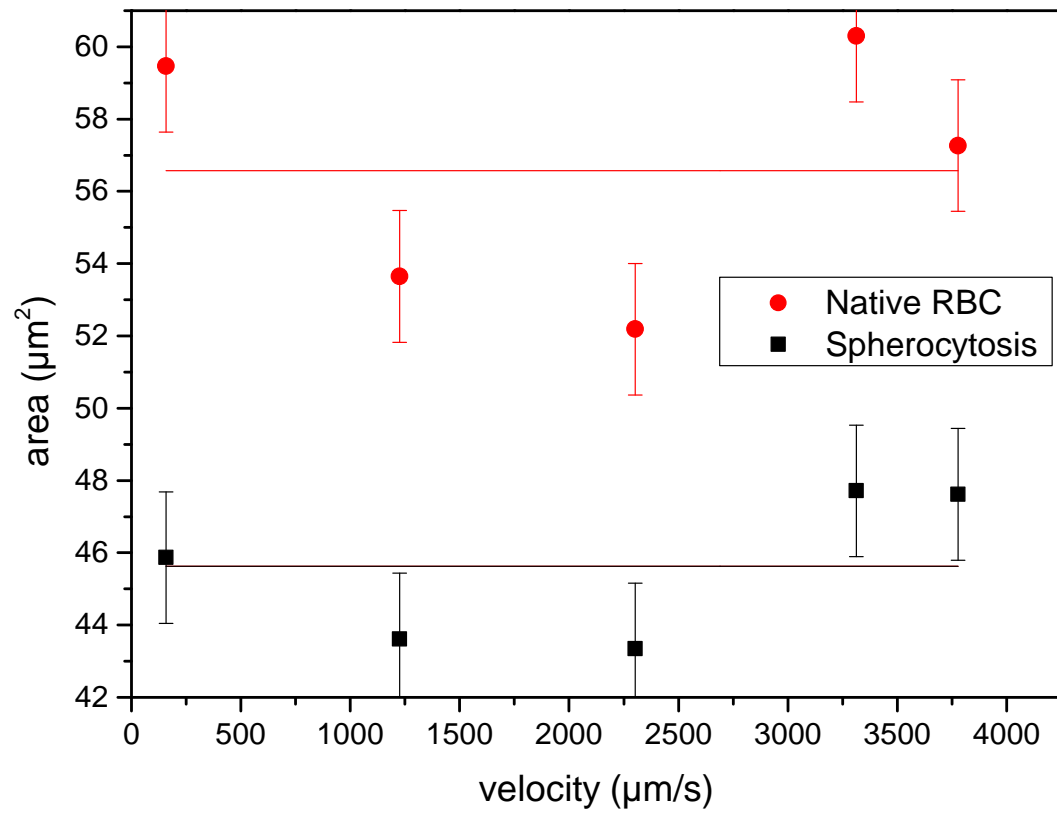
Figure A.2: Size measurement of healthy RBCs (red circles) and RBCs suffering from spherocytosis (black squares) in dependency of their mean velocity in PDMS micro-channels of 10 x 10 μm.

A.8   Alpaca Donors

Here, the healthy donors of alpaca RBCs are shown.

Many thanks to Chromotek GmbH (Prof. Dr. Ulrich Rothbauer, Dr. Tina Romer and Jacqueline Gregor).

Figure A.3: Healthy alpacas in Unterschleißheim, Germany (473 meters above sea level).

A.9   The Dependency of the Young's Modulus on the Indentation Depth

In figure A.4 the dependency of the Young's Modulus E of the indentation depth is shown. It shows the problem of identifying mechanical properties of living cells using the Hertz-Fit. The modulus depends critically on the indentation depth.
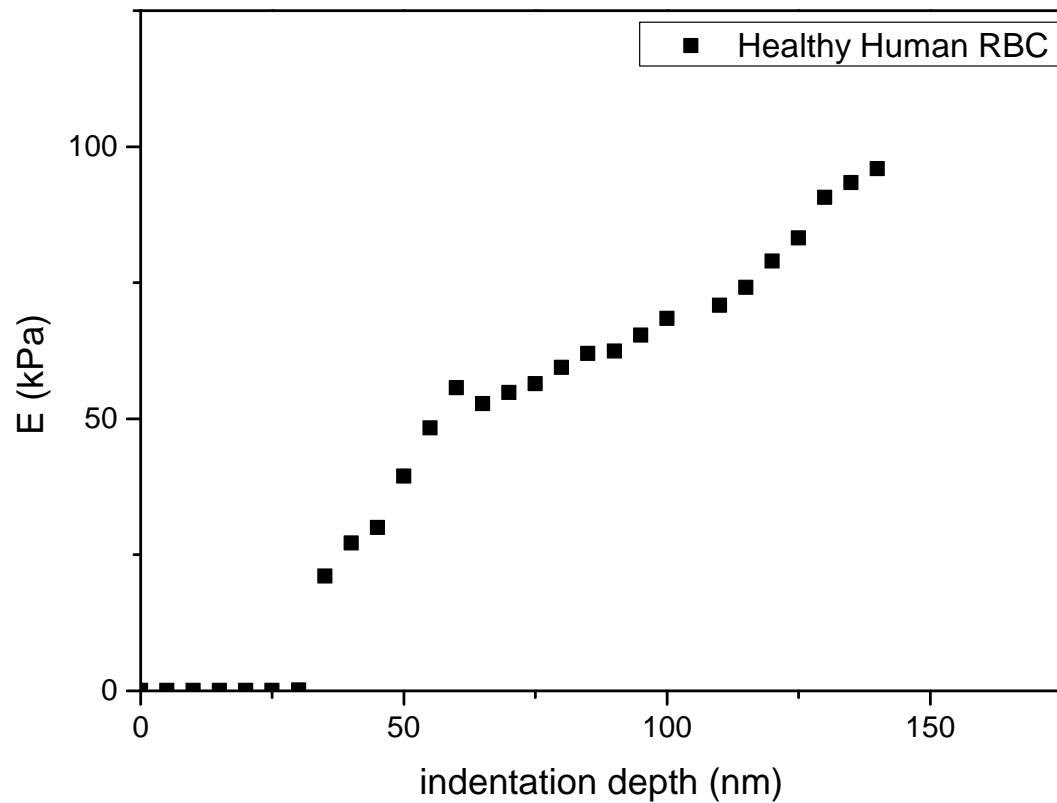
Figure A.4: The dependency of the Young's Modulus on the indentation depth using the Hertz-Fit. Using more data points from deeper indentation depths yields in higher elastic constants. This demonstrates the problem using the Hertz-Fit for visco-elastic materials like RBCs.

Additionally the measurement position may be critical. The cell is thicker at the rim and thinner in the middle. However the setup allowed a very precise localization of the AFM measurement position on the cell.

A.10 Single AFM Measurement

This section shows the distribution of the single measured Young's Moduli. In figure A.5 the relative frequency of the Young's Modulus E of healthy human RBCs is shown.
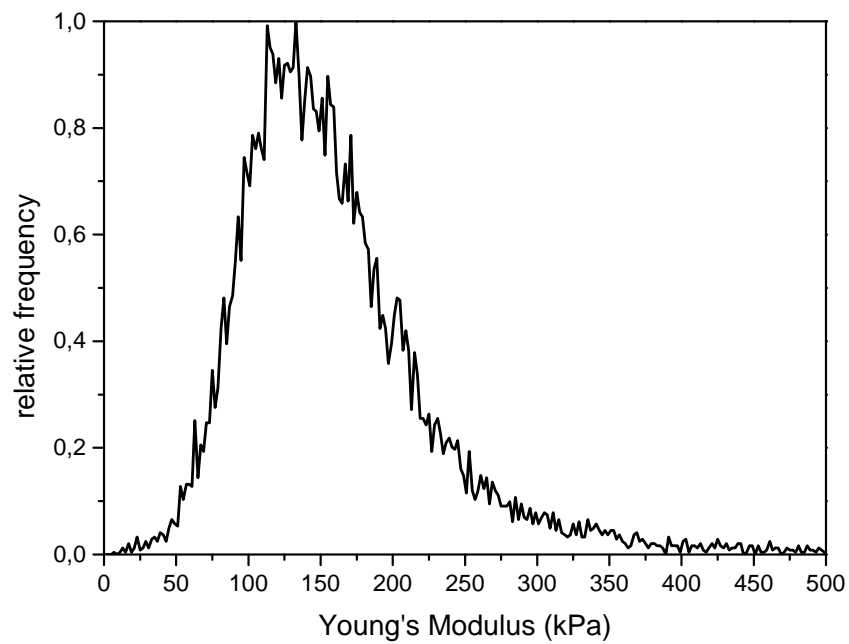

Figure A.5: Relative Frequency of the Young's Modulus E of healthy human RBC.

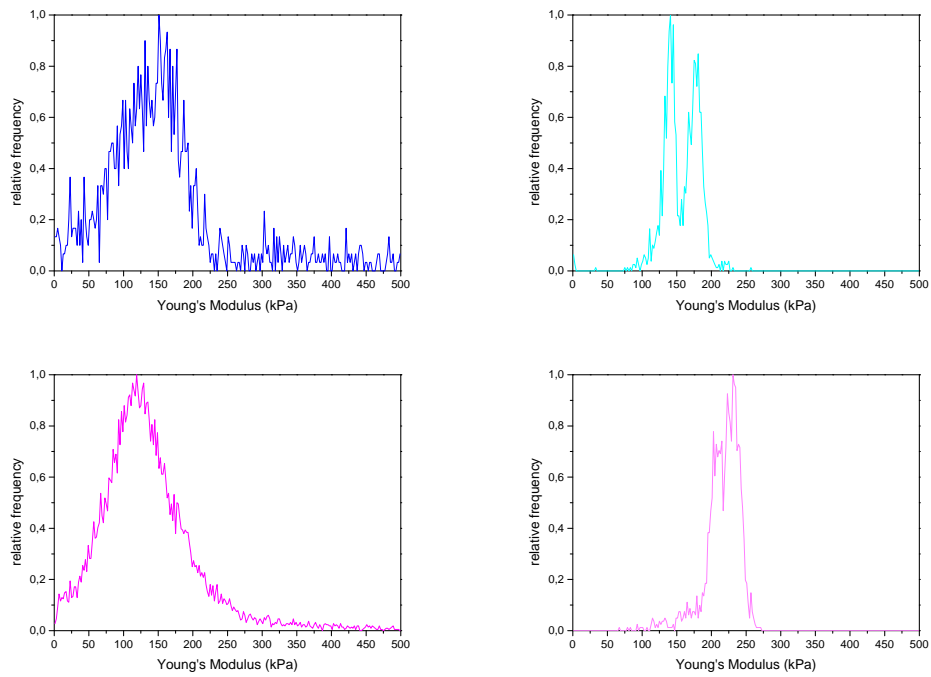Figure A.6 shows the same measurement for the chemically modified RBCs.

Figure A.6: Relative Frequency of the Young's Modulus E for chemically modified RBCs. Formaline 18.4 wt% (top left), formaline 36.8 wt% (top right), diamide 0.34 wt% (bottom left) and diamide 0.68 wt% (bottom right).

A.11 Density Determination of RBC

In this section the measurement of the mean RBC density is explained.

First, the determination of healthy human RBCs is described. Five tubes of different PBS and OptiPrep solutions were prepared and mixed with isolated RBCs.
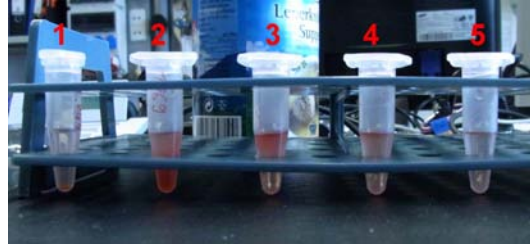

Figure A.7: Tubes filled with human RBC and PBS+OptiPrep of different densities. (1) 1.064 $\frac{kg}{m^3}$; (2) 1.087 $\frac{kg}{m^3}$; (3) 1.107 $\frac{kg}{m^3}$; (4) 1.132 $\frac{kg}{m^3}$; (5) 1.160 $\frac{kg}{m^3}$. Osmolarity of the density solutions is still in the range of normal PBS. Obviously the density of native RBC is in the range of 1.087 and 1.107 $\frac{kg}{m^3}$.

Figure A.7 shows the tubes after 18 h. As the RBCs in the tube having a density of 1.087 are still solved the density of healthy human RBCs is around $1.087 \pm 0.022 \, \text{kg/m}^3$.
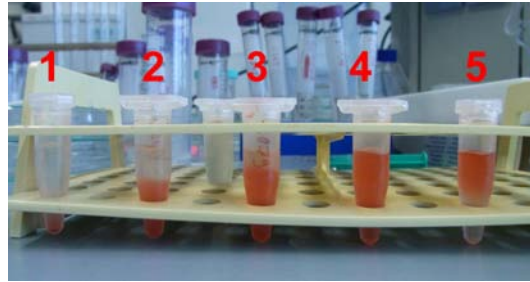

Figure A.8: Alpaca RBC diluted in PBS+OptiPrep of different densities. (1) 1.064 $\frac{kg}{m^3}$; (2) 1.087 $\frac{kg}{m^3}$; (3) 1.107 $\frac{kg}{m^3}$; (4) 1.132 $\frac{kg}{m^3}$; (5) 1,160 $\frac{kg}{m^3}$. Osmolarity of the density solutions is still in the range of normal PBS. Oviously the density of alpaca RBC is around 1.132 $\frac{kg}{m^3}$.

The same experiment was performed with RBCs from alpaca. Figure A.8 shows the tubes containing PBS, OptiPrep of various concentrations and RBCs after 18 h. In the tube having an adjusted density of 1.132 $\frac{kg}{m^3}$ the cells did not sink. Consequently the density is 1.132 $\pm$ 0.027 $\frac{kg}{m^3}$.

A.12 Lens Effect of Cylindrically Shaped Glass Capillaries

During the experiments it turned out that the round shape of the glass capillary shows the same effect as two lenses depending on the inner medium. Figure A.9 shows the effect of the glass capillary lens effect in dependency of three different inner media: air, water and glycerol. To identify the stretching of the glass capillary in one direction the Taylor Deformation of a nearly perfectly ball shaped polystyrol bead is measured. The inset demonstrate the lens effect as well.
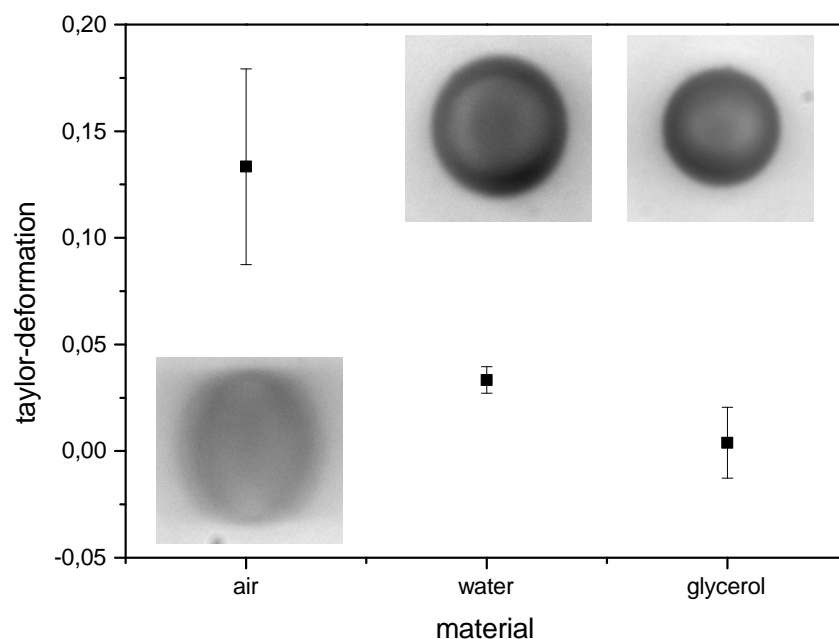

Figure A.9: Capillary Effect of the glass capillary in dependency of three different inner media: air, water and glycerol. As the refraction index of glycerol is nearly the same as for water the round polystyrol bead is not asymmetric.

A.13 Confidence Interval

Here, the R-script to calculate the confidence interval is shown.

Listing A.1: Confidence Interval R-Script

```
1 n <- 109
2 # Messungen
3 test <- sample(c(1,2,3), n, prob=c(0.1,0.3,0.6),
```

```r
4 replace=TRUE)
5
6 # 0-1-Vektoren
7
8 n1 <- 56
9 test1 <- rep(0,n)
10 for(i in 1:n){
11     if(i<=n1){test1[i] <- 1}
12     else{ test1[i] <- 0 }
13 }
14
15 n2 <- 27
16 test2 <- rep(0,n)
17 for(i in 1:n){
18     if(i<=n2){test2[i] <- 1}
19     else { test2[i] <- 0 }
20 }
21
22 n3 <- 26
23 test3 <- rep(0,n)
24     for(i in 1:n){
25     if(i<=n3){test3[i] <- 1}
26 else { test3[i] <- 0 }
27 }
28
29 # Punktschätzer
30 mu1 <- sum(test1)/n
31 mu2 <- sum(test2)/n
32 mu3 <- sum(test3)/n
33
34 # Varianzschätzer
35 sigma1 <- sum((test1 - mu1)^2)/(n-1)
36 sigma2 <- sum((test2 - mu2)^2)/(n-1)
37 sigma3 <- sum((test3 - mu3)^2)/(n-1)
38
39 # Wahrscheinlichkeit für die Aussage
40 z <- qnorm(0.68)
41 t <- qt(0.68, n-1)
42
43 # Konfidenzintervalle
44 I1 <- c( mu1 - z*sqrt(sigma1)/sqrt(n),
45     mu1 + z*sqrt(sigma1)/sqrt(n))
46 I2 <- c( mu2 - z*sqrt(sigma2)/sqrt(n),
47     mu2 + z*sqrt(sigma2)/sqrt(n))
```

```
48  I3 <- c( mu3 - z*sqrt(sigma3)/sqrt(n),
49     mu3 + z*sqrt(sigma3)/sqrt(n))
50
51  I1_t <- c( mu1 - t*sqrt(sigma1)/sqrt(n),
52     mu1 + t*sqrt(sigma1)/sqrt(n))
53  I2_t <- c( mu2 - t*sqrt(sigma2)/sqrt(n),
54     mu2 + t*sqrt(sigma2)/sqrt(n))
55  I3_t <- c( mu3 - t*sqrt(sigma3)/sqrt(n),
56     mu3 + t*sqrt(sigma3)/sqrt(n))
57
58  if(n==(n1+n2+n3)){sprintf("passt")}
59
60  #normalverteilt
61  mu1-I1
62  mu2-I2
63  mu3-I3
64
65  #t-verteilt
66  mu1-I1_t
67  mu2-I2_t
68  mu3-I3_t
```

Bibliography

[1] M. Abkarian, M. Faivre, R. Horton, K. Smistrup, C. Best-Popescu, and H. Stone. Cellular-scale hydrodynamics. *Biomedical Materials (Bristol, England)*, 3(3):034011, September 2008.

[2] M. Abkarian, M. Faivre, and A. Viallat. Swinging of red blood cells under shear flow. *Physical Review Letters*, 98(18):188302, 2007.

[3] M. Abkarian, C. Lartigue, and A. Viallat. Tank Treading and Unbinding of Deformable Vesicles in Shear Flow: Determination of the Lift Force. *Physical Review Letters*, 88(6):068103, January 2002.

[4] M. Abkarian and A. Viallat. Vesicles and red blood cells in shear flow. *Soft Matter*, 4(4):653, 2008.

[5] M. Alghane, B. X. Chen, and Y. Q. Fu. Experimental and numerical investigation of acoustic streaming excited by using a surface acoustic wave device on a 128° YX-LiNbO3 substrate. *Journal of Micromechanics and Microengineering*, 21(1), 2011.

[6] X. An, M. Lecomte, J. Anne, N. Mohandas, and W. Gratzer. Shear-Response of the Spectrin Dimer-Tetramer Equilibrium in the Red Blood Cell Membrane. *The Journal of Biological Chemistry*, 277(35):31796–31800, 2002.

[7] X. An and N. Mohandas. Disorders of red cell membrane. *British Journal of Haematology*, 141(3):367–375, May 2008.

[8] L. Bayliss. The axial drift of the red cells when blood flows in a narrow tube. *The Journal of Physiology*, 149(3):593–613, 1959.

[9] P. Becker, C. Cohen, and S. Lux. The effect of mild diamide oxidation on the structure and function of human erythrocyte spectrin. *Journal of Biological Chemistry*, 261(10):4620–4628, 1986.

[10] W. Bergmann, V. Dressler, C. Haest, and B. Deuticke. Cross-linking of SH-groups in the erythrocyte membrane enhances transbilayer reorientation of phospholipids. Evidence for a limited access of phospholipids to the reorientation sites. *Biochimica et Biophysica Acta*, 769(2):390–398, January 1984.

[11] T. Betz, M. Lenz, J. Joanny, and C. Sykes. ATP-dependent mechanics of red blood cells. *Proceedings of the National Academy of Sciences of the United States of America*, 106(36):15320–15325, September 2009.

[12] D. Boal. Computer simulation of a model network for the erythrocyte cytoskeleton. *Biophysical Journal*, 67(2):521–529, August 1994.

[13] P. Bogner, P. Csutora, I . Cameron, D. Wheatley, and A. Miseta. Augmented water binding and low cellular water content in erythrocytes of camel and camelids. *Biophysical Journal*, 75(6):3085–3091, December 1998.

[14] N. Bouxsein, L. Hirst, and Y. Li. Alignment of filamentous proteins and associated molecules through confinement in microchannels. *Applied Physics Letters*, 85(23), 2004.

[15] S. Braunmüller. *Untersuchung des dynamischen Verhaltens roter Blutkörperchen in mikrofluidischen Systemen*. PhD thesis, Universität Augsburg, 2012.

[16] S. Braunmüller, L. Schmid, and T. Franke. Dynamics of red blood cells and vesicles in microchannels of oscillating width. *Journal of Physics: Condensed Matter*, 23(18):184116, May 2011.

[17] S. Braunmüller, L. Schmid, E. Sackmann, and T. Franke. Hydrodynamic deformation reveals two coupled modes/time scales of red blood cell relaxation. *Soft Matter*, 8(44):11240, 2012.

[18] K. Bremmell, A. Evans, and C. Prestidge. Deformation and nanorheology of red blood cells: an AFM investigation. *Colloids and Surfaces B: Biointerfaces*, 50(1):43–48, June 2006.

[19] P. Bronkhorst, G. Streekstra, and J. Grimbergen. A new method to study shape recovery of red blood cells using multiple optical trapping. *Biophysical Journal*, 69(5):1666–1673, November 1995.

[20] G. Bushell, C. Cahill, F. Clarke, and C. Gibson. Imaging and force-distance analysis of human fibroblasts in vitro by atomic force microscopy. *Cytometry*, 36(3):254–264, 1999.

[21] H. Byun, T. Hillman, J. Higgins, M. Diez-Silva, Z. Peng, M. Dao, R. Dasari, S. Suresh, and Y. Park. Optical measurement of biomechanical properties of individual erythrocytes from a sickle cell patient. *Acta Biomaterialia*, 8(11):4130–4138, November 2012.

[22] A. Chabanel, M. Flamm, and K. Sung. Influence of cholesterol content on red cell membrane viscoelasticity and fluidity. *Biophysical Journal*, 44(2):171–176, 1983.

[23] J. Chasis and S. Shohet. Red cell biochemical anatomy and membrane properties. *Annual Review of Physiology*, 49(1):237–248, 1987.

[24] S. Chien. Red cell deformability and its relevance to blood flow. *Annual Review of Physiology*, 49(1):177–192, 1987.

[25] S. Chien, K. Sung, R. Skalak, S. Usami, and A. Tözeren. Theoretical and experimental studies on viscoelastic properties of erythrocyte membrane. *Biophysical Journal*, 24(2):463–487, November 1978.

[26] A. Christian and M. Haynes. Use of cyclodextrins for manipulating cellular cholesterol content. *Journal of Lipid Research*, 38(11):2264–2272, 1997.

[27] G. Cokelet and H. Meiselman. Rheological comparison of hemoglobin solutions and erythrocyte suspensions. *Science*, 162(3850):275–277, 1968.

[28] G. Danker, T. Biben, T. Podgorski, C. Verdier, and C. Misbah. Dynamics and rheology of a dilute suspension of vesicles: Higher-order theory. *Physical Review E*, 76(4):041905, October 2007.

[29] M. Dao, C. Lim, and S. Suresh. Mechanics of the human red blood cell deformed by optical tweezers. *Journal of the Mechanics and Physics of Solids*, 51(11):2259–2280, November 2003.

[30] J. Deschamps, V. Kantsler, and V. Steinberg. Phase diagram of single vesicle dynamical states in shear flow. *Physical Review Letters*, 102(11):3–6, March 2009.

[31] X. Ding, P. Li, S. Lin, Z. Stratton, N. Nama, F. Guo, D. Slotcavage, X. Mao, J. Shi, F. Costanzo, and T. Huang. Surface acoustic wave microfluidics. *Lab on a Chip*, 13(18):3626–3649, September 2013.

[32] X. Ding, S. Lin, M. Lapsley, S. Li, and X. Guo. Standing surface acoustic wave (SSAW) based multichannel cell sorting. *Lab on a Chip*, 12(21), 2012.

[33] D. Discher, D. Boal, and S. Boey. Simulations of the Erythrocyte Cytoskeleton at Large Deformation . II . Micropipette Aspiration. *Biophysical Journal*, 75(3):1584–1597, 1998.

[34] C. Doerschuk, H. Coxson, and J. Hogg. The site of neutrophil (PMN) accumulation within the pulmonary capillary bed after infusion of zymosan-activated plasma (ZAP). *The American Review of Respiratory Disease*, 139(A302), 1989.

[35] J. Drury and M. Dembo. Hydrodynamics of micropipette aspiration. *Biophysical Journal*, 76(1):110–128, January 1999.

[36] I. Dulinska, M. Targosz, W. Strojny, M. Lekka, P. Czuba, W. Balwierz, and M. Szymonski. Stiffness of normal and pathological erythrocytes studied by means of atomic force microscopy. *Journal of Biochemical and Biophysical Methods*, 66(1):1–11, March 2006.

[37] S. Eber and S. Lux. Hereditary spherocytosis - defects in proteins that connect the membrane skeleton to the lipid bilayer. *Seminars in Hematology*, 41(2):118–141, April 2004.

[38] B. Eggart. Chemically Modified Red Blood Cells in Fluidic Environment, Masterthesis, 2010.

[39] E. Evans. New membrane concept applied to the analysis of fluid shear-and micropipette-deformed red blood cells. *Biophysical Journal*, 13(9):941–954, September 1973.

[40] E. Evans. Bending elastic modulus of red blood cell membrane derived from buckling instability in micropipet aspiration tests. *Biophysical Journal*, 43(1):27–30, July 1983.

[41] E. Evans. Structure and deformation properties of red blood cells: Concepts and quantitative methods. *Methods in Enzymology*, 173:3–35, 1989.

[42] E. Evans and R. Hochmuth. A solid-liquid composite model of the red cell membrane. *The Journal of Membrane Biology*, 30(1):351–362, 1976.

[43] E. Evans and R. Hochmuth. Membrane viscoelasticity. *Biophysical Journal*, 16(1):1–11, January 1976.

[44] E. Evans, N. Mohandas, and A. Leung. Static and dynamic rigidities of normal and sickle erythrocytes. Major influence of cell hemoglobin concentration. *Journal of Clinical Investigation*, 73(2):477–488, 1984.

[45] E. Evans, R. Waugh, and L. Melnik. Elastic area compressibility modulus of red cell membrane. *Biophysical Journal*, 16(6):585–595, June 1976.

[46] J. Evans, W. Gratzer, N. Mohandas, K. Parker, and J. Sleep. Fluctuations of the red blood cell membrane: relation to mechanical properties and lack of ATP dependence. *Biophysical Journal*, 94(10):4134–4144, May 2008.

[47] T. Fischer. Shape memory of human red blood cells. *Biophysical Journal*, 86(5):3304–3313, May 2004.

[48] T. Fischer. Tank-tread frequency of the red cell membrane: dependence on the viscosity of the suspending medium. *Biophysical Journal*, 93(7):2553–2561, October 2007.

[49] T. Fischer, M. Stohr-Lissen, and H. Schmid-Schonbein. The red cell as a fluid droplet: tank tread-like motion of the human erythrocyte membrane in shear flow. *Science*, 202(4370):894–896, November 1978.

[50] A. Forsyth, J. Wan, W. Ristenpart, and H. Stone. The dynamic behavior of chemically "stiffened" red blood cells in microchannel flows. *Microvascular Research*, 80(1):37–43, July 2010.

[51] A. Forsyth, J. Wana, P. Owrutskyb, M. Abkarianc, and H. Stone. Multiscale approach to link red blood cell dynamics, shear viscosity, and ATP release. *Proceedings of the National Society*, 108(27):1–6, 2011.

[52] Y. Fung. *Biomechanics: motion, flow, stress, and growth*. Springer, 1990.

[53] P. Gaehtgens. In vitro studies of blood rheology in microscopic tubes. *The Rheology of Blood, Blood Vessels, and Associated Tissues*, 1(3):257–275, 1981.

[54] S. Guido and G. Tomaiuolo. Microconfined flow behavior of red blood cells in vitro. *Comptes Rendus Physique*, 10(8):751–763, November 2009.

[55] K. Haase. Manipulation von roten Blutkörperchen in akustischen und mikrofluidischen Feldern, Masterthesis, 2013.

[56] V. Heinrich, K. Ritchie, N. Mohandas, and E. Evans. Elastic thickness compressibilty of the red cell membrane. *Biophysical Journal*, 81(3):1452–1463, September 2001.

[57] W. Helfrich. Elastic properties of lipid bilayers: theory and possible experiments. *Zeitschrift für Naturforschung. Teil C: Biochemie, Biophysik, Biologie, Virologie*, 28(11):693–703, 1973.

[58] S. Henon, G. Lenormand, A. Richert, and F. Gallet. A new determination of the shear modulus of the human erythrocyte membrane using optical tweezers. *Biophysical Journal*, 76(2):1145–1151, 1999.

[59] R. Hochmuth. Surface Elasticity and Viscosity of Red Cell Membrane. *Journal of Rheology*, 23(6):669, 1979.

[60] R. Hochmuth. Micropipette aspiration of living cells. *Journal of Biomechanics*, 33(1):15–22, January 2000.

[61] R. Hochmuth and R. Waugh. Erythrocyte membrane elasticity and viscosity. *Annual Review of Physiology*, 49(1):209–219, 1987.

[62] J. Hogg. Neutrophil kinetics and lung injury. *Physiological Reviews*, 67(4):1249–1295, 1987.

[63] J. Hogg. Neutrophil kinetics in the pulmonary microcirculation. *The Pulmonary Circulation and Acute Lung Injury (2nd edition)*, 141:253–269, 1991.

[64] Y. Huang, C. Doerschuk, and R. Kamm. Computational modeling of RBC and neutrophil transit through the pulmonary capillaries. *Journal of Applied Physiology*, 90(2):545–564, February 2001.

[65] C. Humpert and M. Baumann. Local membrane curvature affects spontaneous membrane fluctuation characteristics. *Molecular Membrane Biology*, 20(2):155–162, 2003.

[66] K. Humphry, P. Kulkarni, and D. Weitz. Axial and lateral particle ordering in finite Reynolds number channel flows. *Physics of Fluids*, 22(8), 2010.

[67] J. Hutter and J. Bechhoefer. Calibration of atomic-force microscope tips. *Review of Scientific Instruments*, 64(7):1868, 1993.

[68] W. Hwang and R. Waugh. Energy of dissociation of lipid bilayer from the membrane skeleton of red blood cells. *Biophysical Journal*, 72(6), 1997.

[69] A. Iolascon, R. Avvisati, and C. Piscopo. Hereditary spherocytosis. *Transfusion Clinique et Biologique*, 17(3):138–142, September 2010.

[70] C. Johnson, H. Tang, and C. Carag. Forced unfolding of proteins within cells. *Science*, 317(5838), 2007.

[71] G. Johnson, D. Allen, T. Flynn, B. Finkel, and J. White. Decreased Survival In Vivo of Diamide-incubated Dog Erythrocytes. *Journal of Clinical Investigation*, 66(5):955–961, 1980.

[72] D. Jones. The reaction of formaldehyde with unsaturated fatty acids during histological fixation. *The Histochemical Journal*, 4(5):421–465, August 1969.

[73] I. Kahane, A. Shifter, and E. Rachmilewitz. Cross-linking of red blood cell membrane proteins induced by oxidative stress in β thalassemia. *FEBS Letters*, 85(2):267–270, 1978.

[74] V. Kantsler, E. Segre, and V. Steinberg. Vesicle dynamics in elongation flow: Wrinkling instability and bud formation. *Physical Review Letters*, 99(178102):1–4, 2007.

[75] B. Kaoui, G. Biros, and C. Misbah. Why Do Red Blood Cells Have Asymmetric Shapes Even in a Symmetric Flow? *Physical Review Letters*, 103(18):188101, October 2009.

[76] B. Kaoui, N. Tahiri, T. Biben, H. Ez-Zahraouy, a. Benyoussef, G. Biros, and C. Misbah. Complexity of vesicle microcirculation. *Physical Review E*, 84(4):041906, October 2011.

[77] J. Khodadad and R. Weinstein. The band 3-rich membrane of llama erythrocytes: studies on cell shape and the organization of membrane proteins. *The Journal of Membrane Biology*, 72(3), 1983.

[78] D. Köster. Numerical simulation of acoustic streaming on surface acoustic wave-driven biochips. *SIAM Journal on Scientific Computing*, 29(6), 2007.

[79] M. Kraus, W. Wintz, U. Seifert, and R. Lipowsky. Fluid Vesicles in Shear Flow. *Physical Review Letters*, 77(17):3685–3688, October 1996.

[80] D. Kuzman, S. Svetina, R. Waugh, and B. Žekš. Elastic properties of the red blood cell membrane that determine echinocyte deformability. *European Biophysics Journal*, 33(1):1–15, 2004.

[81] R. Law, G. Liao, S. Harper, and G. Yang. Pathway shifts and thermal softening in temperature-coupled forced unfolding of spectrin domains. *Biophysical Journal*, 85(5), 2003.

[82] J. Lee and D. Discher. Deformation-Enhanced Fluctuations in the Red Cell Skeleton with Theoretical Relations to Elasticity , Connectivity , and Spectrin Unfolding. *Biophysical Journal*, 81(6):3178–3192, 2001.

[83] A. Lehninger. *Prinzipien der Biochemie.* Walter de Gruyter, 1987.

[84] M. Lekka, P. Laidler, J. Ignacak, and M. Labedz. The effect of chitosan on stiffness and glycolytic activity of human bladder cells. *Biochim Biophys Acta*, 1540:1–10, 2001.

[85] G. Lenormand, S. Hénon, A. Richert, J. Siméon, and F. Gallet. Direct measurement of the area expansion and shear moduli of the human red blood cell membrane skeleton. *Biophysical Journal*, 81(1):43–56, July 2001.

[86] S. Levine, M. Levine, K. Sharp, and D. Brooks. Theory of the electrokinetic behavior of human erythrocytes. *Biophysical Journal*, 42(2):127–135, May 1983.

[87] J. Lewis. Comparative hematology - studies on camelidae. *Comparative Biochemistry and Physiology*, 55(4):367–371, 1976.

[88] J. Lidmar, L. Mirny, and D. Nelson. Virus shapes and buckling transitions in spherical shells. *Physical Review E*, 68(5):051910, November 2003.

[89] W. Linss, C. Pilgrim, and H. Feuerstein. How thick is the glycocalyx of human erythrocytes? *Acta Histochemica*, 91(1):101–104, 1991.

[90] R. Lipowsky. The conformation of membranes. *Nature*, 1991.

[91] C. Long. A principle of prolation in biology. *WSEAS Transactions on Biology and Medicine*, (3):1–5, 2004.

[92] C. Long. Evolution of function and form in camelid erythrocytes. *Proceedings of the 2007 WSEAS Int. Conference on Cellular & Molecular Biology - Biophysics & Bioengineering*, pages 18–24, 2007.

[93] R. Mario and P. Morrison. Physiological response to heat and dehydration in the guanaco. *Physiological Zoology*, 36(1):45–51, 1963.

[94] R. McPherson, W. Sawyer, and L. Tilley. Band 3 mobility in camelid elliptocytes: implications for erythrocyte shape. *Biochemistry*, 32(26):6696–6702, July 1993.

[95] T. Mezger. *The Rheology Handbook*. Vincentz Network, 2002.

[96] A. Minerick, R. Zhou, P. Takhistov, and H. Chang. Manipulation and characterization of red blood cells with alternating current fields in microdevices. *Electrophoresis*, 24(21):3703–3717, 2003.

[97] D. Mirijanian and G. Voth. Unique elastic properties of the spectrin tetramer as revealed by multiscale coarse-grained modeling. *Proceedings of the National Society*, 105(4):1204–1208, 2008.

[98] C. Misbah. Vacillating breathing and tumbling of vesicles under shear flow. *Physical Review Letters*, 96(2):028104, 2006.

[99] Y. Missirlis and M. Brain. An improved method for studying the elastic properties of erythrocyte membranes. *Blood*, 54(5):1069–1079, November 1979.

[100] N. Mohandas and E. Evans. Mechanical properties of the red cell membrane in relation to molecular structure and genetic defects. *Annual Review of Biophysics and Biomolecular Structure*, 23(1):787–818, 1994.

[101] N. Mohandas and P. Gallagher. Red cell membrane: past, present, and future. *Blood*, 112(10):3939–3948, 2008.

[102] F. Morel, R. Baker, and H. Wayland. Quantitation of human red blood cell fixation by glutaraldehyde. *The Journal of Cell Biology*, 48(1):91–100, January 1971.

[103] T. Nakajima, K. Kajiwara, and J. McIntyre. *Advanced Fiber Spinning Technology*. Crc Press, 1 edition, 1994.

[104] H. Noguchi and G. Gompper. Shape transitions of fluid vesicles and red blood cells in capillary flows. *Proceedings of the National Academy of Sciences of the United States of America*, 102(40):14159–14164, October 2005.

[105] H. Noguchi, G. Gompper, L. Schmid, A. Wixforth, and T. Franke. Dynamics of fluid vesicles in flow through structured microchannels. *EPL (Europhysics Letters)*, 89(8002):1–6, 2010.

[106] E. Ogura, P. Abatti, and T. Moriizumi. Measurement of human red blood cell deformability using a single micropore on a thin Si/sub 3/N/sub 4/film. *IEEE Transactions on Biomedical Engineering*, 38(8):721–726, 1991.

[107] N. Olivieri. The beta-thalassemias. *New England Journal of Medicine*, 3412:99–109, 1999.

[108] S. Omorphos, C. Hawkey, and C. Rice-Evans. The elliptocyte: a study of the relationship between cell shape and membrane structure using the camelid erythrocyte as a model. *Comparative Biochemistry and Physology*, 94(4):789–795, 1989.

[109] S. Perrotta, P. Gallagher, and N. Mohandas. Hereditary spherocytosis. *The Lancet*, 372(9647):1411–1426, 2008.

[110] M. Peterson. Linear response of the human eryhtrocte to mechanical stress. *Physical Review A*, 45(6):4116–4131, 1992.

[111] D. Petschow and I. Wurdinger. Causes of high blood O2 affinity of animals living at high altitude. *Journal of Applied Physiology: Respiratory, Environmental and Exercise Physiology*, 42(2):139–143, February 1977.

[112] K. Phillips, S. Jacques, and O. McCarty. Measurement of Single Cell Refractive Index, Dry Mass, Volume, and Density Using a Transillumination Microscope. *Physical Review Letters*, 109(11):118105, September 2012.

[113] J. Poiseuille. Recherches sur la force du coeur aortiqueJ. *Thèse de Médecine de Paris*, 166, 1828.

[114] R. Presson. Pulmonary capillaries are recruited during pulsatile flow. *Journal of Applied Physiology*, 92(3):1183–1190, 2002.

[115] A. Price and D. Fischer. Deformation-induced release of ATP from erythrocytes in a poly (dimethylsiloxane)-based microchip with channels that mimic resistance vessels. *Analytical Chemistry*, 76(16):4849–4855, 2004.

[116] A. Pries and Secomb T. Blood flow in microvascular networks. *Circulation Research*, 97(4):826–834, 1990.

[117] L. Randles, R. Rounsevell, and J. Clarke. Spectrin domains lose cooperativity in forced unfolding. *Biophysical Journal*, 92(2):571–577, 2007.

[118] M. Reid and N. Mohandas. Red blood cell blood group antigens: structure and function. *Seminars in Hematology*, 41(2):93–117, 2004.

[119] C. Reynafarje and J. Faura. Oxygen transport of hemoglobin in high-altitude animals (Camelidae). *Journal of Applied Physiology*, 38(5):806–810, 1975.

[120] M. Rief, J. Pascual, M. Saraste, and H. Gaub. Single molecule force spectroscopy of spectrin repeats: low unfolding forces in helix bundles. *Journal of Molecular Biology*, 286(2):553–561, 1999.

[121] H. Römpp, F. Jürgen, and M. Regitz. *Römpp Basislexikon Chemie.* Thieme, Stuttgart, 1999.

[122] E. Sackmann. Thermo-elasticity and adhesion as regulators of cell. *Condensed Matter*, 18(45):785–825, 2006.

[123] D. Salem, N. Aminuddin, and D. Baird. *Structure Formation in Polymeric Fibers.* Hanser Gardner Publ, 1 edition, 2001.

[124] L. Scheffer, A. Bitler, E. Ben-Jacob, and R. Korenstein. Atomic force pulling: probing the local elasticity of the cell membrane. *Single Molecules*, 1(2):83–90, 2000.

[125] S. Schrier. Pathobiology of thalassemic erythrocytes. *Current Opinion Hematology*, 4(2):75–8, 1997.

[126] J. Schwegler and R. Lucius. *Der Mensch-Anatomie und Physiologie.* Georg Thieme Verlag, 2 edition, 2011.

[127] T. Secomb. Flow-dependent rheological properties of blood in capillaries. *Microvascular Research*, 34(1):46–58, 1987.

[128] T. Secomb, R. Hsu, and A. Pries. Motion of red blood cells in a capillary with an endothelial surface layer: effect of flow velocity. *American Journal of Physiology. Heart and Circulatory Physiology*, 281(2):629–636, August 2001.

[129] TW Secomb and N Ozkaya. Flow of axisymmetric red blood cells in narrow capillaries. *Journal of Fluid Mechanics*, 163:405–423, 1986.

[130] U. Seifert, K. Berndl, and R. Lipowsky. Shape transformations of vesicles: Phase diagram for spontaneous-curvature and bilayer-coupling models. *Physical Review A*, 44(2):1182, 1991.

[131] E. Shinar and E. Rachmilewitz. Haemoglobinopathies and red cell membrane function. *Baillière's Clinical Haematology*, 6(2):357–369, 1993.

[132] A. Sillau, S. Cueva, A. Valenzuela, and Candela E. O2 transport in the alpaca (Lama pacos) at sea level and at 3,300 m. *Respiratory Physiology*, 27:147–155, 1976.

[133] R. Skalak and P. Branemark. Deformation of red blood cells in capillaries. *Science*, 164:717–719, 1969.

[134] R. Skalak, N. Ozkaya, and T. Skalak. Biofluid mechanics. *Annual Review of Fluid Mechanics*, 21(42):167–204, 1989.

[135] R. Skalak, A. Tozeren, R. Zarda, and S. Chien. Strain energy function of red blood cell membranes. *Biophysical Journal*, 13(3):245–264, 1973.

[136] J. Skotheim and T. Secomb. Red Blood Cells and Other Nonspherical Capsules in Shear Flow: Oscillatory Dynamics and the Tank-Treading-to-Tumbling Transition. *Physical Review Letters*, 98(7):078301, February 2007.

[137] J. Smith. Variability in erythrocyte deformability among various mammals. *American Journal of Physiology*, 236(5):725–730, 1979.

[138] H. Song, J. Tice, and R. Ismagilov. A microfluidic system for controlling reaction networks in time. *Angewandte Chemie*, 115(7):767–772, 2003.

[139] N. Staub and E. Schultz. Pulmonary capillary length in dog, cat and rabbit. *Respiration Physiology*, 5:371–378, 1968.

[140] M. Stolz, R. Raiteri, A. Daniels, M. VanLandingham, W. Baschon, and U. Aebi. Dynamic elastic modulus of porcine articular cartilage determined at two different levels of tissue organization by indentation-type atomic force microscopy. *Biophysical Journal*, 86(5):3269–3283, 2004.

[141] H. Strey, M. Peterson, and E. Sackmann. Measurement of Erythrocyte Membrane Elasticity by Flicker Eigenmode Decomposition. *Biophysical Journal*, 69(2):478–488, 1995.

[142] S. Sutera, V. Seshadri, P. Croce, and R. Hochmuth. Capillary blood flow: II. Deformable model cells in tube flow. *Microvascular Research*, 4(2):420–433, 1970.

[143] Y. Suzuki, N. Tateishi, M. Soutani, and N. Maeda. Deformation of erythrocytes in microvessels and glass capillaries: effects of erythrocyte deformability. *Microcirculation*, 3(23):49–57, 1996.

[144] S. Svetina and B. Žekš. Membrane bending energy and shape determination of phospholipid vesicles and red blood cells. *European Biophysics Journal*, 17(2):101–111, 1989.

[145] P. Tabeling. *Introduction to microfluidics*. Oxford, 2005.

[146] N. Tahiri, T. Biben, and H. Ez-Zahraouy. On the problem of slipper shapes of red blood cells in the microvasculature. *Microvascular Research*, 85:40–45, 2012.

[147] M. Tan, J. Friend, and L. Yeo. Direct visualization of surface acoustic waves along substrates using smoke particles. *Applied Physics Letters*, 91(22):224101, 2007.

[148] P. Teitel. Polymicroviscometry of spectrin cross-linked red blood cells: theoretical and clinical implications. *Scandinavian Journal of Clinical and Laboratory Investigations*, 41:235–237, 1981.

[149] G. Tomaiuolo, M. Barra, and V. Preziosi. Microfluidics analysis of red blood cell membrane viscoelasticity. *Lab on a Chip*, 11(3):449–454, 2011.

[150] G. Tomaiuolo and S. Guido. Start-up shape dynamics of red blood cells in microcapillary flow. *Microvascular Research*, 82(1):35–41, 2011.

[151] G. Tomaiuolo, L. Lanotte, and G. Ghigliotti. Red blood cell clustering in Poiseuille microcapillary flow. *Physics of Fluids*, 24(5):051903, 2012.

[152] G. Tomaiuolo, D. Rossi, and S. Caserta. Comparison of two flow based imaging methods to measure individual red blood cell area and volume. *Cytometry Part A*, 81(12):1040–1047, 2012.

[153] G. Tomaiuolo, M. Simeone, and V. Martinelli. Red blood cell deformation in microconfined flow. *Soft Matter*, 5(19):3736–3740, 2009.

[154] T. Traykov and R. Jain. Effect of transmembrane potential on the deformability of RBC's suspended in carbohydrate-saline solutions. *Journal of Colloid and Interface Science*, 114(1):0–3, 1986.

[155] M. Trebbin, D. Steinhauser, J. Perlich, A. Buffet, S. Roth, W. Zimmermann, J. Thiele, and S. Förster. Anisotropic particles align perpendicular to the flow direction in narrow microchannels. *Proceedings of the National Academy of Sciences of the United States of America*, 110(17):6706–11, April 2013.

[156] K. Tsukada, E. Sekizuka, C. Oshio, and H. Minamitani. Direct measurement of erythrocyte deformability in diabetes mellitus with a transparent microchannel capillary model and high-speed video camera system. *Microvascular Research*, 61(3):231–239, 2001.

[157] A. Van Leeuwenhoek. Other microscopical observations made by the same, about the texture of the blood, the sap of some plants, the figures of sugar and salt, and the probable cause of the difference of their tastes. *Philosophical Transactions of the Royal Society of London*, 10:380–385, 1675.

[158] V. Vitkova, M. Mader, and T. Podgorski. Deformation of vesicles flowing through capillaries. *Europhysics Letters (EPL)*, 68(3):398–404, November 2004.

[159] R. Waugh and R. Bauserman. Physical measurements of bilayer-skeletal separation forces. *Annals of Biomedical Engineering*, 23(25):308–321, 1995.

[160] R. Waugh and P. Celle. Abnormalities in the membrane material properties of hereditary spherocytes. *Journal of Biomechanical Engineering*, 102:240– 246, 1980.

[161] R. Waugh, M. Narla, C. Jackson, T. Mueller, T. Suzuki, and G. Dale. Rheologic properties of senescent erythrocytes: loss of surface area and volume with red blood cell age. *Blood*, 79(5):1351–1358, 1992.

[162] D. Weatherall and J. Clegg. Thalassaemia - a global public health problem. *Nature Medicine*, 2:847–849, 1996.

[163] J. West, K. Tsukimoto, O. Mathieu-Costello, and R. Prediletto. Stress failure in pulmonary capillaries. *Journal of Applied Physiology*, 70(4):1731–1742, 1991.

[164] K. Wittmann. Cholesterol-modifizierte rote Blutkörperchen im Mikrofluss, Bachelorthesis, 2011.

[165] A. Wörl. Einfluss der hereditären Sphärozytose auf die dynamische Form von roten Blutkörperchen, Bachelorthesis, 2013.

[166] H. Wu, T. Kuhn, and V. Moy. Mechanical properties of L929 cells measured by atomic force microscopy: effects of anticytoskeletal drugs and membrane crosslinking. *Scanning*, 20:389–397, 1998.

[167] H. Wyss, T. Franke, and D. Weitz. Capillary micromechanics : Measuring the elasticity of microscopic soft objects. *Soft Matter*, 6:4550–4555, 2010.

[168] H. Wyss and J. Henderson. Biophysical properties of normal and diseased renal glomeruli. *American Journal of Cell Physiology*, 300:397–405, 2011.

[169] R. Yagil, U. Sod-Moriah, and N. Meyerstein. Dehydration and camel blood. I. Red blood cell survival in the one-humped camel Camelus dromedarius. *American Journal of Physiology*, 226(2):298–300, 1974.

[170] K. Yamaguchi, K. Jfirgens, H. Bartels, and J. Piiper. Oxygen transfer properties and dimensions of red blood cells in high-altitude camelids, dromedary camel and goat. *Journal of Comparative and Physiology*, 157(1):1–9, January 1987.

[171] T. Yamaguchi, S. Yamada, and E. Kimoto. Effects of Cross-Linking of Membrane Proteins on Vesiculation. *Journal of Biochemistry*, 115(4):659–663, 1994.

[172] A. Yazdani and P. Bagchi. Phase diagram and breathing dynamics of a single red blood cell and a biconcave capsule in dilute shear flow. *Physical Review E*, 84(2), August 2011.

[173] K. Zeman, H. Engelhard, and E. Sackmann. Bending undulations and elasticity of the erythrocyte membrane: effects of cell shape and membrane organization. *European Biophysics Journal*, 18(4):203–219, January 1990.

[174] R. Zhou, J. Gordon, A. Palmer, and H. Chang. Role of Erythrocyte Deformability During Capillary Wetting. *Biotechnology and Bioengineering*, 93(2):201–211, 2005.

[175] A. Zilker, H. Engelhardt, and E. Sackmann. Dynamic reflection interference contrast (RIC-) microscopy: a new method to study surface excitations of cells and to measure membrane bending elastic moduli. *Journal de Physique*, 48(12):2139–2151, 1987.

Danksagung

Zum Abschluss möchte ich die Gelegenheit ergreifen und mich bei den Leuten bedanken, die wesentlich zum Gelingen dieser Doktorarbeit sowie meines bisherigen Werdegangs an der Universität Augsburg beigetragen haben. Im Speziellen erwähnt sei,